Title
A multitude of meals and mechanisms: How microglia sculpt the brain

Author
Dorman, Leah Cathleen

Publication Date
2022

A Multitude of Meals and Mechanisms: How Microglia Sculpt the Brain

by
Leah Cathleen Dorman

DISSERTATION
Submitted in partial satisfaction of the requirements for degree of
DOCTOR OF PHILOSOPHY

in

Neuroscience

in the

GRADUATE DIVISION
of the
UNIVERSITY OF CALIFORNIA, SAN FRANCISCO

Approved:

DocuSigned by:
Michael Stryker
15DFF21E2A5440C...

Michael Stryker
Chair

DocuSigned by:
Anna Victoria Molofsky
D0C1B5C25...

Anna Victoria Molofsky

DocuSigned by:
Tomasz Nowakowski
DAE3...

Tomasz Nowakowski

DocuSigned by:
Kira Poskanzer
64ED3BCFD209496...

Kira Poskanzer

Committee Members

Dedication

In loving memory of Eileen Smith Dorman

Acknowledgements

This thesis represents an incredible amount of work from many people I have had the pleasure of calling colleagues and friends. I don't have space to thank everyone here, but I appreciate everyone who has helped along the way. First, I would like to thank my mentor, Anna Molofsky, for creating a supportive and collaborative environment in which to become a better scientist. Anna, thank you for supporting me through thick and thin, helping me to focus on the important questions, and vastly improving everything I write. Thank you to my qualifying exam and thesis committee members: Tom Nowakowski, Kira Poskanzer, Michael Stryker, Grae Davis, and Li Gan for scientific guidance and support throughout this process.

Special thanks to all of my co-authors, especially Ilia Vainchtein, Phi Nguyen, Nick Silva, Rafael Han, and Caroline Escoubas Guney, for your invaluable assistance and permission to use your work in this dissertation. Working closely with each of you made my time in the lab immensely more enjoyable and fulfilling, and none of the work presented here would have been possible without you. To Marci Rosenberg and Jerika Barron, thanks for the endless technical expertise, emotional support, and general cheeriness that made coming in to lab fun. Thank you to Hiromi Nakao-Inoue for being the best founding lab manager imaginable, and to Sunrae Taloma for helping hold the lab together during a pandemic while applying for grad school. Thanks to Haruna Nakajo, Christian Lagares-Linares, Ellen Wang, Beatriz Cuevas, Nadine Horneck, Yinghong Xiao, Peter Lidsky, Brianna Rivera, Bjoern Schwer, Carlo Condello, and Raul Andino for helping get these papers across the finish line. Thank you to Carol Kim for all of the support you provide behind the scenes, and thanks to all the lab members past and present, especially Richard Jin, Ricky Guajardo, Kevin Kelley, Sarah Wang, Lukasz Szewczyk, Sarah Wade, and John Miller, for your support, expertise, and friendship.

Thanks to my cohort, Frances Cho, Trisha Vaidyanathan, Selin Schamiloglu, Michael Reitman, Ben Mansky, and Match McGregor. I couldn't have asked for a more supportive, intellectually rigorous, thoughtful and friendly group of students to go through grad school with. Thanks to Stephanie Holden, Lindsay Osso, and the rest of NS 2014 for being incredibly welcoming, Anna Lipkin for dancing with me, and Michelle Cahill for being the best conference buddy. Michael Reitman, Austin Wang, Tara Aitken, Monique Lillis, Cindy Liu, Lay Kodama, Alison Comrie, and Chenyu Wang, thank you for making the student handbook a reality.

I owe a debt of gratitude to my science teachers at Ohlone College, who taught me "basic" science with the kind of depth that allows the ideas to stick even when the details fade: Maru Grant, James Baxter, Anu Ganguly, and Luc Desmedt. Thank you to Barry Starr, John Olson, Ira Clark, and Harley Kornblum for introducing me to scientific research, and thanks to my first research mentor Yasmin Ghochani for an incredible amount of patience.

Academic research requires an incredible number of moving parts, and I would like to thank all the people who dealt with the behind-the-scenes work that allowed me to focus on research. Thank you to the neuroscience program directors from 2015-2022 and especially the program administrators, Pat Veitch and Lucita Nacionales, for guiding me through this process. Thank you to the support staff at Rock Hall, particularly the janitorial staff and LARC staff and veterinarians, for making our work possible. Thank you as well to the mice and fish who literally made this work feasible.

If the key to grad school is work-life balance, I've only achieved a semblance of that through the efforts of many friends. Thank you to Peggy Peabody and the entire Ballet Petit community past and present, particularly the extended carpool family, for providing a refuge of incremental success that didn't depend on fickle experiments. Thanks to Jr. Company 2022 for

bringing a vision to life. Thanks to the dancers of Bliss Dance Company and Mannakin Dance Theater for the wonderful performance opportunities. To all my college friends, especially Cho Ki Tam-Ferguson, Sharon Lee, and Tien Phan-Everson, thank you for the laughter and conversations across the years and miles. Thank you to Poornima Meenakshisundaram and the entire Venkatesan family for many years of friendship and encouragement. A million thanks to my amazing friend and roommate Sonja Wright for somehow putting up with me through many stressful years. I truly appreciate all the emotional support and chocolate.

Finally and most importantly, thank you to my entire extended family, especially my grandparents Margaret and Pete Beck and George and Eileen Dorman, for the dangerously high dose of stubbornness genes as well as the unconditional love and support regardless of how many times I said I'd graduate "this year". To my siblings, Sarah, Claire, Eric, and Charmaine Dorman, thank you for alternatively providing transportation, deep conversations, advice, food, vacations, and hilarious diversions. This likely would have been far more entertaining if any of you had written it. Finally, there are no words to express my deep appreciation for my parents, Catherine and Michael Dorman. Mom, thank you for being my first and best teacher. Thank you for fostering a love of learning by allowing me to study whatever I wanted and always focusing on improvement rather than perfection. Dad, thank for teaching me that in order for a dissertation to amount to more than a hill o'beans, the thrust of said dissertation must be something other than "newness". Thank you for teaching me rationality and logic, and for modeling an incredible depth of commitment to any project you take on. All of you have made this possible, and in return you are all required to call me "doctor" at least once a year in perpetuity.

Contributions

Chapters 1 and 5 were written by Leah Dorman.

Chapter 2 was reproduced in its entirety from the following preview article:

Dorman, L. C., & Molofsky, A. V. (2019, January 15). Demystifying Microglia: And Now the Work Begins. Immunity 50, 11–13.

Chapter 3 was adapted from the following published article:

Silva, N.J., Dorman, L.C., Vainchtein, I.D., Horneck, N.C., and Molofsky, A. V. (2021). In situ and transcriptomic identification of microglia in synapse-rich regions of the developing zebrafish brain. Nat. Commun. 2021 121 12, 1–12.

> Conceptualization: N.J.S., A.V.M., I.D.V., and L.C.D.; methodology, N.J.S., I.D.V, and L.C.D.; investigation, N.J.S, I.D.V, L.C.D, and N.C.H.; writing—original draft, N.J.S., L.C.D., and A.V.M.; writing—review & editing, all co-authors; funding acquisition, A.V.M., and N.J.S. resources, A.V.M.; supervision, A.V.M. and I.D.V

Chapter 4 was adapted from the following article, currently in review:

Dorman, L.C., Nguyen, P.T., Escoubas, C.C., Vainchtein, I.D., Xiao, Y., Lidsky, P. V., Nakajo, H., Silva, N.J., Lagares-Linares, C., Wang, E.Y., Taloma, S.E., Cuevas, B., Nakao-Inoue, H., Rivera, B.M., Schwer, B., Condello, C., Andino, R., Nowakowski, T.J., and Molofsky, A.V. (2021). A type I interferon response defines a conserved microglial state required for effective phagocytosis. BioRxiv 2021.04.29.441889.

Conceptualization: A.V.M and L.C.D.; Methodology, L.C.D., A.V.M, P.T.N., I.D.V., C.C.E., H. N-I., Y.X., B.R., C.C., R.A. B.S., H.N., N.J.S.; Investigation: L.C.D., P.T.N., I.D.V, S.E.T., C.C.E, E.W., B.R., Y.X., P.V.L., C.L.L., B.C., H.N., N.J.S.; Writing – Original Draft, L.C.D., P.T.N., C.C.E., and A.V.M.; Writing – Review & Editing, all co-authors; Funding Acquisition, A.V.M. and L.C.D; Resources, A.V.M., C.C., R.A., Supervision, A.V.M., T.N., C.C., R.A., B.S., and I.D.V.

A multitude of meals and mechanisms: How microglia sculpt the brain

By Leah Cathleen Dorman

Abstract

Microglia, the innate immune cells of the brain, are exquisitely sensitive to dynamic changes in the brain environment. They respond to extracellular signals in order to promote synapse formation and turnover, respond to tissue damage and pathogens, and clean up dead or dying cells. Ultimately, microglia are professional phagocytes; so how do they decide what to eat? This dissertation examines multiple transcriptomically and functionally distinct subpopulations of phagocytic microglia that shape the developing brain. Chapter 1 is an introduction to microglia with an emphasis on phagocytosis. Chapter 2 introduces single-cell sequencing of microglia through a mini-review of two papers published in 2019. Chapter 3 characterizes two populations of microglia in the developing zebrafish brain, showing that neuron-engulfing and synapse-associated microglia have distinct transcriptomic and morphological states depending on their local environment. Chapter 4 identifies a new molecular signature associated with microglia that are actively engulfing whole neurons in the developing murine brain. These transient interferon-responsive microglia restrict the accumulation of damaged neurons. Chapter 5 discusses the implications of this work and how carefully designing single cell sequencing experiments in combination with *in situ* work allows the functional and transcriptomic characterization of transient and rare populations.

Table of Contents

List of Figures

List of Tables

Chapter 1: Introduction

Microglia, the innate immune cells of the brain, are exquisitely sensitive to dynamic changes in the brain environment. They respond to extracellular signals in order to promote synapse formation and turnover, respond to tissue damage and pathogens, and clean up dead or dying cells. However, the intercellular communication pathways that regulate these diverse skill sets and ensure that microglia act appropriately to their environment are not fully understood.

Microglia were discovered and defined in the early 20th century by Pío del Río-Hortega as tiny 'glial' cells, much smaller than astrocytes and neurons, that altered their morphology during injury or disease and were capable of phagocytosis, the process of engulfing and breaking down other cells (Sierra et al., 2016). The word 'glia' is derived from the Greek word for glue, as astrocytes, the first recognized glial cells, were thought to hold the brain together like glue. Microglia were lumped into this category because they are also non-neuronal cells found in the brain; however, they do not share an origin with other neural cell types as they are not derived from neural stem cells. Microglia are macrophages derived from the embryonic yolk sac that migrate into the brain during embryogenesis, where they colonize and proliferate throughout early postnatal development (Ginhoux et al., 2010). As the only immune cells found within the brain parenchyma, they are now known to be capable of a wide variety of functions made possible by their motility and ability to respond quickly to environmental cues (Li and Barres, 2018). Microglia are constantly moving their processes to scan their environment for cues such as purines that might indicate damage or pathogens, which they can then migrate towards (Davalos et al., 2005; Nimmerjahn et al., 2005). They can actively modulate synapses in a variety of ways, including by

increasing spine stability, promoting synaptic and circuit maturation, and reducing hyperexcitability (Hoshiko et al., 2012; Li et al., 2012; Miyamoto et al., 2016; Popova et al., 2021). As professional phagocytes closely related to peripheral macrophages, they can also engulf entire cells (Galloway et al., 2019; Grommes et al., 2008; Peri and Nüsslein-Volhard, 2008; Sierra et al., 2010; VanRyzin et al., 2019) as well as portions of cells including synaptic structures (Izquierdo et al., 2021; Paolicelli et al., 2011; Schafer et al., 2012; Vainchtein et al., 2018; Weinhard et al., 2018).

How do microglia know what to eat in which context? This question is important both for understanding the process of neural development and for potentially developing targeted therapeutics that could inhibit or promote particular microglial functions in disease states. Phagocytosis is a multi-step, highly regulated process that relies on recognition of a substrate in need of phagocytosis; a response from the phagocyte including moving towards the substrate and changing its membrane shape to allow engulfment; and then processing of the engulfed object through the lysosomal pathway to be broken down and recycled (Uribe-Querol and Rosales, 2020). The signals, receptors, response mechanisms, and lysosomal pathways can vary depending on the nature of the substrate. Engulfment of whole cells can act through multiple signaling pathways including the TAM receptors Axl and Mertk (Fourgeaud et al., 2016a; Lemke, 2013), each of which has multiple ligands including Gas6, which can promote phagocytosis (Grommes et al., 2008). Activation of the TREM2-ApoE pathway can also promote phagocytosis of both apoptotic cells and amyloid-beta, particularly in disease states and potentially in the developing white matter tracts (Hammond et al., 2019; Krasemann et al., 2017; Li et al., 2019a; Shirotani et al., 2019; Takahashi et al., 2005). Additional signaling pathways that rely on receptors Tim-4 and Bai1 have been identified during engulfment of apoptotic cells, but have not been linked to disease states

(Mazaheri et al., 2014a; Park et al., 2007). Microglia can also engulf apoptotic newborn neurons (Sierra et al., 2010) and even astrocytes (VanRyzin et al., 2019), potentially through a Mertk-dependent pathway (Diaz-Aparicio et al., 2020). Intriguingly, microglia may not always wait for the cells they engulf to die but instead promote the programmed cell death of damaged neurons through a process called phagoptosis (Brown and Neher, 2014).

In the absence of appropriate regulatory mechanisms, microglial phagocytosis – or the lack thereof - could wreak havoc on the nervous system; therefore, it is perhaps unsurprising that multiple redundant pathways continue to be found that both promote and prevent phagocytosis. Transcriptomic analyses of microglia in different environments is a promising method to elucidate different phagocytic programs and potentially identify how microglia respond to different stimuli. In the following works, we used single-cell sequencing as a tool in combination with *in situ* methods to identify novel microglial regulators of phagocytosis of extracellular matrix, synaptic material, and whole neurons.

This work uses single-cell sequencing, a tool which is uniquely suited to identifying unique subpopulations of cells based on a snapshot of their current transcriptome, to characterize multiple novel cell states of both microglia and neurons. In each case, we used a combination of sequencing and imaging techniques to map transcriptomically defined cell states onto functional subpopulations of cells, each with a particular role in sculpting the intact brain. Chapter 2 provides a brief introduction to using single-cell sequencing to characterize transient cell states through a mini-review of two microglial sequencing studies published in 2019 (Hammond et al., 2019; Li et al., 2019a). The main body of work in this thesis can be found in chapters 3 and 4, in which a combination of sequencing and imaging techniques are used to functionally and transcriptomically characterize diverse microglial cell states found in the developing brain.

Chapter 3 investigates the relationship between regional environment and functional states within microglia in the zebrafish brain. Zebrafish are a model organism characterized by juveniles with translucent skin that facilitates live imaging. This study also took advantage of the fact that zebrafish brains have very distinct regional separation between areas of neurogenesis and areas of synaptogenesis, allowing closer investigation of the relationship between microglial structure and function. Here we investigate differences in microglial populations in the neurogenic optic tectum (OT) and the synapse-rich hindbrain (HB). By overlaying regional information from bulk sequencing with single-cell sequencing analysis of microglia from the whole brain, we found that each region had enrichment of a particular microglial transcriptomic signature that enabled the functions necessary for that region, namely engulfing newborn neurons in the OT and interacting with synapses in the HB. We characterized the distinct cell states populating each region, found that these distinct cell populations persist into adulthood, and found gene candidates for the regulation of microglial morphology and function.

Chapter 4 defines a population of interferon-responsive microglia in a sterile physiological environment which are necessary for the efficient phagocytosis of dead and dying cells in the developing mouse brain. This cell population rapidly expands following the stressor of topographic remapping in the somatosensory cortex following whisker cauterization in neonatal mice, which allowed us to capture this rare transcriptomic signature using single-cell sequencing of microglia from intact and whisker deprived somatosensory cortices. The sequencing analysis predicted that this population represented a transient cell state involved in the engulfment of neurons in the developing brain. Using a candidate gene identified through this analysis, we imaged these microglia *in situ* and found that interferon-responsive microglia were specifically phagocytosing whole neurons, and in many cases multiple neurons simultaneously. Furthermore, we discovered

that blocking interferon signaling in mice with no other developmental stressor resulted in dysmorphic microglia, fewer dead cells, and the accumulation of neurons with DNA damage. While more work remains to be done to elucidate the exact mechanisms controlling this process, our work suggests that interferon signaling allows microglia to kill and eat "stressed" neurons quickly during development, preventing the accumulation of damaged neurons within fragile developing cortical circuitry. Intriguingly, this population is also expanded in a wide range of pathological conditions. The implications of this remain to be determined, but gaining more control of the mechanisms by which microglia recognize and remove damaged neurons could be a key to the therapeutic potential of microglia. Further discussion of the ramifications and future directions suggested by this work are presented in Chapter 5.

Chapter 2: An introduction to single-cell sequencing analysis of microglia

---

The following essay was published as a preview article in Immunity for two microglial single-cell sequencing papers published in Immunity and Neuron in 2019 (Hammond et al., 2019; Li et al., 2019a). *These papers influenced the interpretation and analysis of my microglial dataset analyzed in Chapter 6, and this preview is included here as an introduction to whole-brain single-cell sequencing of microglia including a brief discussion of various cell isolation and sequencing techniques and the potential and limitations of these analyses.*

Demystifying microglia: and now the work begins

Microglia actively shape the developing brain, but their transcriptional diversity is not well understood. Complementary studies by Hammond *et al* and Li *et al* (Hammond et al., 2019; Li et al., 2019a) characterize the microglial transcriptome at single cell resolution, highlighting their diversity during development, aging, and pathology.

Microglia are the primary tissue-resident immune cells of the central nervous system (CNS). As the macrophages of the CNS parenchyma, microglia shape neural development through phagocytosis of apoptotic cells and neuronal synaptic elements. Microglia also actively survey and respond to changes in the brain environment, responding to a wide variety of signaling molecules such as neurotransmitters, cytokines, and 'alarmins' such as ATP and IL-33. Microglial dysfunction is linked to both developmental and neurodegenerative disorders, implicating them as potential drivers and therapeutic targets for a variety of neurologic diseases. Yet despite this intense interest, the heterogeneity of microglia across time, space, gender, and disease states is only beginning to be elucidated.

In complementary papers published in January 2019 in *Immunity* and *Neuron*, the authors use single-cell transcriptomics to define the transcriptional state of microglia over development and aging (**Fig. 2.1**). Several common themes emerge. Both the Stevens/McCarroll and the Barres groups, in Hammond *et al* and Li *et al* respectively, found that microglial heterogeneity peaks early in development. Both groups identified a distinct and previously uncharacterized population of microglia in the developing white-matter – regions of brain tissue rich in myelinated neuronal axons and relatively devoid of neuronal synapses. This microglial subset expresses a gene signature including *Spp1*, *Gpnmb*, *Igf1*, and *Clec7a*. Li *et al* further showed that this subset is more amoeboid and phagocytic, whereas Hammond *et al* demonstrated that this subtype shares some transcriptomic features with disease-associated microglia. Separately, Hammond *et al* characterized the aging and sex-specific microglial transcriptomes.

This set of studies represents an important next step in the recent flourishing of microglial "omics" analyses, and a reminder of how far we have come (Ransohoff and Cardona, 2010). Although microglia had been long described in the brain, they were not firmly established as hematopoietic cells until the discovery of the transcription factor Pu.1, which is required for the emergence of microglia from an embryonic common myeloid progenitor (McKercher et al., 1996). Subsequent transcriptomic and epigenetic analyses of Pu.1 positive cells across tissues defined local signals that drive differences between tissue-resident macrophages (Gosselin et al., 2014; Lavin et al., 2014). In the brain these include Transforming Growth Factor beta (TGF-β) dependent signaling, which drives a core adult homeostatic microglial signature including *Fcrls*, *HexB*, *P2ry12*, and *Tmem119* (Bennett et al., 2016; Butovsky et al., 2014). Recent single-cell sequencing has identified three epochs of microglial development- embryonic, early postnatal, and adult (Matcovitch-Natan et al., 2016), consistent with the studies described below. The transcriptional

profile of disease associated microglia is also beginning to be elucidated in a variety of contexts, including in a mouse model of Alzheimer's disease (5xFAD) which identified a disease associated microglia (DAM) signature linked to the Alzheimer's risk gene *Trem2* (Keren-Shaul et al., 2017).

The 2019 papers from the Barres and Stevens labs support much of the work above, while further defining potential microglial sub-populations and transcriptomic signatures. Li *et al* isolated about 2000 myeloid cells from the mouse CNS (excluding the midbrain) using tissue homogenization followed by FACS isolation of CD11b+/CD45+ cells at embryonic day 14.5, postnatal day 7, and postnatal day 60. Using Smart-Seq2 technology, they sequenced each cell to a depth of 1 million reads and additionally were able to retain metadata regarding surface marker expression and the region of origin.

In Hammond *et al*, the Stevens and McCarroll labs took an alternative approach to maximize cell capture over depth of sequencing. After isolating microglia from whole mouse brains at E14.5, P4/5, P30, P100, and P540, they sorted 76,000 microglia using the droplet-based high throughput single cell sequencing. Smart-Seq2 captures about 50% more genes per cell than the droplet-based platform offered by 10x Genomics, which the authors offset by maximizing the number of cells sequenced. Additional differences in the observed clusters can be partially explained by the fact that in Hammond *et al* the mice were perfused and potential infiltrating peripheral cells expressing high levels of CD45 were excluded, thereby nearly eliminating the monocyte clusters observed by Li and colleagues. Additionally, Hammond *et al* isolated microglia from the whole brain while Li *et al* selected six brain regions from which to isolate cells, excluding microglia in the midbrain and other regions.

Both studies highlighted the early postnatal period as the peak of microglial diversity, while adult microglia isolated from diverse brain regions appeared relatively homogenous. Hammond *et*

al additionally identified two small populations of adult microglia that become more prominent in older mice and show upregulation of inflammatory or interferon-related genes. Interestingly, Hammond *et al* examined both male and female mice and found few sex-based differences during development and aging. There is an emerging literature suggesting important functional differences between male and female microglia in a variety of disease contexts. So far, those differences are not clearly reflected in the homeostatic microglial transcriptome, where sex differences have been identified by some groups but not others. It may be necessary to capture the transcriptome at the right place, time, and disease context. It is also possible that current tools do not adequately capture the temporal dynamics of microglial state changes, and that new cell capture and bioinformatic approaches will be required.

During development, microglia engulf both apoptotic cells and synapses, depending on time and region. Interestingly, both of the current studies identified a unique developmentally restricted population of phagocytic microglia. This population, which can be identified by the expression of *Spp1*, *Gpnmb, Igf1*, and *Clec7a*, appeared in the early postnatal (P4/5 and P7) microglia and was largely absent in both embryonic and adult mice. Both groups showed that these cells are restricted to developing white matter tracts in the corpus callosum and cerebellum, and the Barres lab demonstrated that this population consists of amoeboid, phagocytic cells capable of engulfing oligodendrocytes. It is worth noting that studies of microglia during development have overwhelmingly focused on synapse elimination and engulfment of apoptotic neurons. Yet the most transcriptionally striking cluster of microglia from these studies are in brain regions devoid of both synapses and neuronal cell bodies. Functional investigation of how microglia shape white matter development is a clear future direction.

Reactive microglia are a hallmark of the diseased brain and actively phagocytose degenerative tissues. Hammond *et al* also sequenced microglia from an established model of demyelination- injection of the toxic compound lysolecithin. They found that demyelination led to a marked expansion of an inflammatory microglial subset in the white matter expressing *Apoe*, interferon-inducible genes, and chemokines. They compared this dataset to the disease associated microglia (DAM) identified in the 5xFAD model of Alzheimer's Disease (Keren-Shaul et al., 2017). Interestingly, the DAMs fit within a subset of the clusters identified in their demyelinating lesion, suggesting both common and divergent activation patterns across injury states. Ultimately functional analyses of these different disease-associated microglial subsets will be essential.

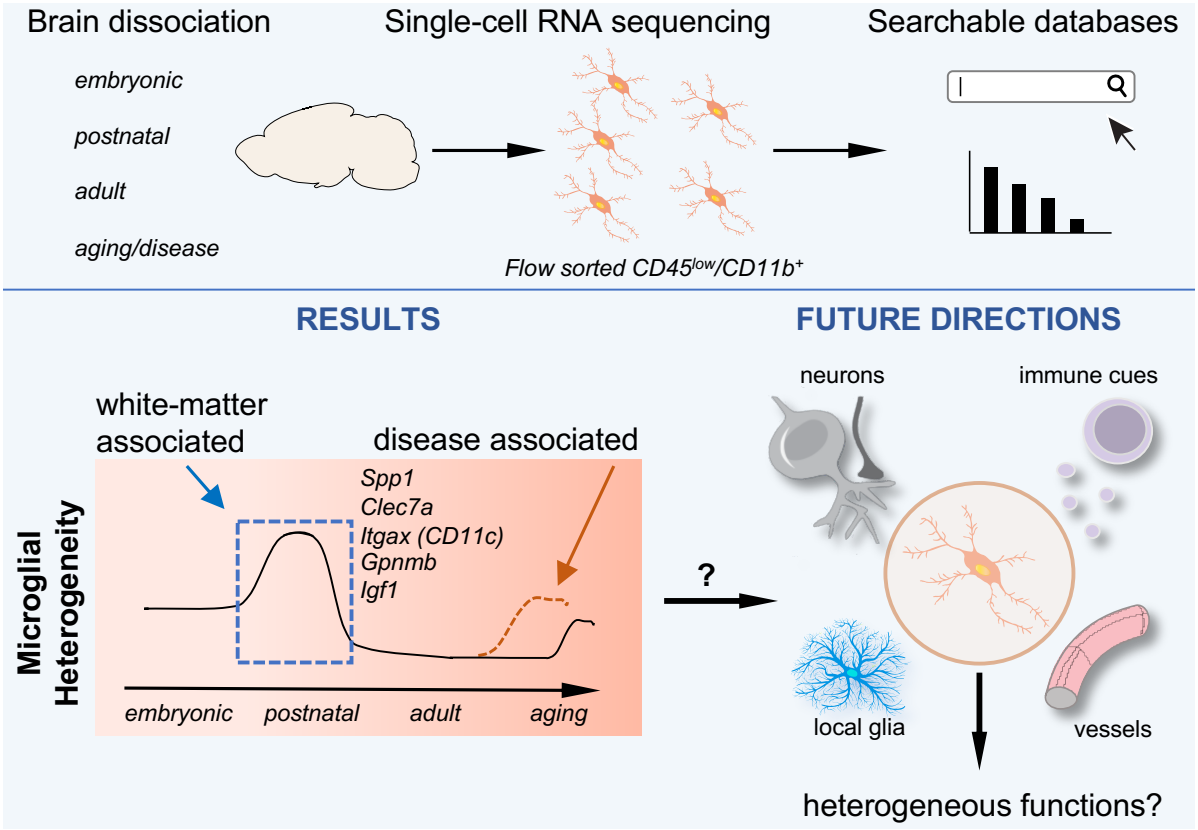

Figure 2.1: Single cell sequencing reveals microglial age and location-dependent heterogeneity. Hammond et al and Li et al isolated microglia from developing and adult mouse brain tissue and used single cell sequencing to determine the resting microglial transcriptome. Microglial heterogeneity peaks during development and increases with aging and disease. Future work should address cell autonomous vs. cell extrinsic cues that drive heterogeneity (neurons, immune and peripheral signals, local glial cells including astrocytes and oligodendrocytes, and vasculature). The functional significance of this heterogeneity remains to be determined.

In summary, these complementary papers add to a growing body of literature on the microglial transcriptome, at a time when microglial function is increasingly implicated in neurodevelopment and disease. The authors have made their data available on the Barres website *brainrnaseq.org* (Li *et al*) and *microgliasinglecell.com* (Hammond *et al*), providing a valuable reference for others studying microglia. It is bittersweet to note that Ben Barres is not only a posthumous senior author on one of the studies, but one of the foundational influences in a rigorous approach to glial gene expression. All who have used these datasets over the years (and who might remember the familiar sight of Ben pulling out his smartphone to look up genes in the middle of a talk) will appreciate the potential biological insights that evolve from such resources. And yet, more biology is essential. Future work should build on these datasets to define the upstream cues that establish microglial heterogeneity. Defining the existence, functional relevance, or prognostic potential of these subsets in human tissues will be critical to potential therapeutic targeting of microglial subtypes in disease. The work described in the current papers, together with others in the field, will provide convergent lines of evidence from which to begin to address these goals.

Chapter 3: *In situ* and transcriptomic identification of microglia in synapse rich regions of the developing zebrafish brain

Summary

Microglia are brain resident macrophages that play vital roles in central nervous system (CNS) development, homeostasis, and pathology. Microglia both remodel synapses and engulf apoptotic cell corpses during development, but whether unique molecular programs regulate these distinct phagocytic functions is unknown. Here we identify a molecularly distinct microglial subset in the synapse rich regions of the zebrafish (*Danio rerio*) brain. We found that ramified microglia increased in synaptic regions of the midbrain and hindbrain between 7 and 28 days post fertilization. In contrast, microglia in the optic tectum were ameboid and clustered around neurogenic zones. Using single-cell mRNA sequencing combined with metadata from regional bulk sequencing, we identified synaptic-region associated microglia (SAMs) that were highly enriched in the hindbrain and expressed multiple candidate synapse modulating genes, including genes in the complement pathway. In contrast, neurogenic associated microglia (NAMs) were enriched in the optic tectum, had active cathepsin activity, and preferentially engulfed neuronal corpses. These data reveal that molecularly distinct phagocytic programs mediate synaptic remodeling and cell engulfment, and establish the zebrafish hindbrain as a model for investigating microglial-synapse interactions.

Introduction

Microglia are the dominant immune cells in the central nervous system (CNS). They perform critical functions during brain development and disease including engulfing synapses, promoting synapse formation, and clearing apoptotic neurons (Colonna and Butovsky, 2017; Wu et al., 2015). However, it is not clear whether these diverse functions are mediated by molecularly distinct subsets of microglia. Single-cell sequencing of mouse microglia reveals transcriptional heterogeneity predominantly during development (Hammond et al., 2019; Li et al., 2019a), whereas functional studies reveal region-specific microglial populations that persist into adulthood (Ayata et al., 2018; Sierra et al., 2010; VanRyzin et al., 2019). These data suggest that transcriptional profiling in rodents has not yet been able to resolve known functional heterogeneity in microglia. Furthermore, linking these transcriptionally identified subpopulations to functional subsets *in situ* remains challenging. Thus, despite abundant evidence that microglia both modulate synapses and engulf cell corpses during development, the molecular regulation of these different functions is not well understood.

The zebrafish (*Danio rerio*) is an increasingly utilized vertebrate model for developmental neuroscience (Sakai et al., 2018) that has not yet been used to study microglial-synapse interactions. Zebrafish microglia are ontogenetically similar to mammalian microglia and express most canonical microglia genes identified in mammals (Butovsky et al., 2014; Geirsdottir et al., 2019; Mazzolini et al., 2020; Oosterhof et al., 2017). The neuroimmune interface is also similar between species, including a diversity of glial cell types (Chen et al., 2020; Kawai et al., 2001; Lyons and Talbot, 2014) and an immune system homologous to mammals (Meeker and Trede, 2008; Renshaw and Trede, 2012; Rougeot et al., 2019), including meningeal lymphatics (Chen et al., 2019) and a blood brain barrier that matures between 8-10 days post fertilization (dpf) (Fleming

et al., 2013). There are also many similarities in nervous system development, with the exception that robust neurogenesis persists throughout life in the zebrafish brain. This leads to ongoing turnover of neuronal corpses in neurogenic regions, particularly in the midline optic tectum (OT). Much of our functional understanding of fish microglia comes from elegant work in the OT identifying molecular mechanisms that drive phagocytosis of neuronal corpses (Mazaheri et al., 2014a; Shen et al., 2016; Villani et al., 2019). However, microglia in the OT are functionally and ontogenetically distinct from those found in other CNS regions (Casano et al., 2016; Herbomel et al., 2001; Svahn et al., 2013; Wu et al., 2018). In addition, a subset of microglia in the spinal cord white matter engulfs myelin sheaths (Hughes and Appel, 2020) and is linked to leukodystrophy (Oosterhof et al., 2018). These functionally distinct microglia subsets coexist in the developing zebrafish nervous system and are to some extent segregated by CNS region.

Interestingly, despite tremendous interest in defining the role of microglia in synaptic remodeling in mammals, it is not known whether there are unique molecular programs that subserve this functional specialization. Furthermore, while the zebrafish is an ideal model system in which to study microglial-synaptic interactions, whether microglia are present in synaptic regions of the fish CNS is not well defined. Recent studies suggest that transcriptional and functional heterogeneity of microglia in the adult zebrafish brain is in part linked to their developmental origins, whereby ameboid OT microglia derived from the rostral blood island (RBI) and aortic gonad mesonephros (AGM) have enhanced capacity to phagocytose bacteria in vitro, compared to more ramified microglia that appear to be exclusively AGM derived (Ferrero et al., 2018; Wu et al., 2020; Xu et al., 2015). Like in mammals, it is difficult to precisely define to what extent ontogeny defines function. However, these studies suggest that zebrafish microglia are

regionally and molecularly distinct in a manner that impacts function, raising the question of whether synapse-associated functions could be transcriptionally defined.

Here we identify a distinct subpopulation of synaptic-region associated microglia (SAMs) in the juvenile fish using *in situ* characterization as well as single cell and bulk RNA sequencing. SAMs were ramified and expanded in the midbrain and hindbrain after 7 dpf. These microglia engulf neuronal synaptic proteins as in mammals and were defined by expression of complement genes (*c1qa, c1qc*) and other candidate pathways. In contrast, microglia in the optic tectum clustered near neurogenic regions, were rich in lysosomal gene expression (*ctsla, ctsba*), and their phagocytic capacity correlated with functional cathepsin activity. These data define a molecular profile associated with phagocytosis of synaptic proteins and suggest a model system in which to study microglial-synapse interactions.

Results

Microglia in synaptic regions expand developmentally in the zebrafish hindbrain and are distinct from neurogenic-associated microglia

To characterize microglia in both synaptic and neurogenic regions of the fish brain, we performed immunohistochemistry using the myeloid reporter line *Tg*(*mpeg1.1:GFP-CAAX*) (Villani et al., 2019). We used the presynaptic vesicle marker SV2 to demarcate synapse rich regions and bromodeoxyuridine (BrdU) labelling to identify neurogenic zones. We observed microglia in synapse rich regions of the midbrain and hindbrain at the earliest time-point we examined, 7 days post fertilization (dpf), and found that they increased in number over the late larval to juvenile period (14-28 dpf; **Fig 3.1a-b**). By 28 dpf most microglia in the midbrain and hindbrain colocalized with the presynaptic marker SV2 (65% and 80%, respectively; **Fig 3.1c-d**). In contrast, >60% of

microglia in the optic tectum (OT) clustered near the BrdU+ neurogenic zone (**Fig 3.1e-f**), consistent with their known roles in eliminating apoptotic cell corpses (Herbomel et al., 2001; Svahn et al., 2013). Immunostaining with the commonly used microglia antibody 4C4 was consistent with these findings and indicated that the majority (70-90%) of *mpeg1.1*-GFP^{+} cells in the brain are microglia, with a modestly lower proportion in the midbrain and hindbrain relative to OT (**Fig. S3.1.1a-b**). Of note, while 4C4 is not detected in border-associated macrophages, it also fails to label some ramified *mpeg1.1*-GFP^{+} parenchymal cells that are putative microglia, suggesting that it is specific to microglia (vs. macrophages), but not entirely sensitive (**Fig. S3.1.1c-e**). We next characterized microglial morphology in the hindbrain and OT. We found that microglia (*mpeg1.1*-GFP^{+} 4C4^{+}) in the hindbrain were ramified and more closely resembled microglia in the postnatal rodent brain, whereas OT microglia were on average significantly more ameboid, as quantified by increased sphericity (**Fig 3.1g-h**). Sholl analysis supported the finding that HB microglia are significantly more ramified than OT microglia (**Fig 3.1i**). In summary, we identified ramified microglia enriched in synapse-rich regions of the hindbrain and midbrain that were distinct from amoeboid microglia seen around neurogenic regions of the optic tectum.

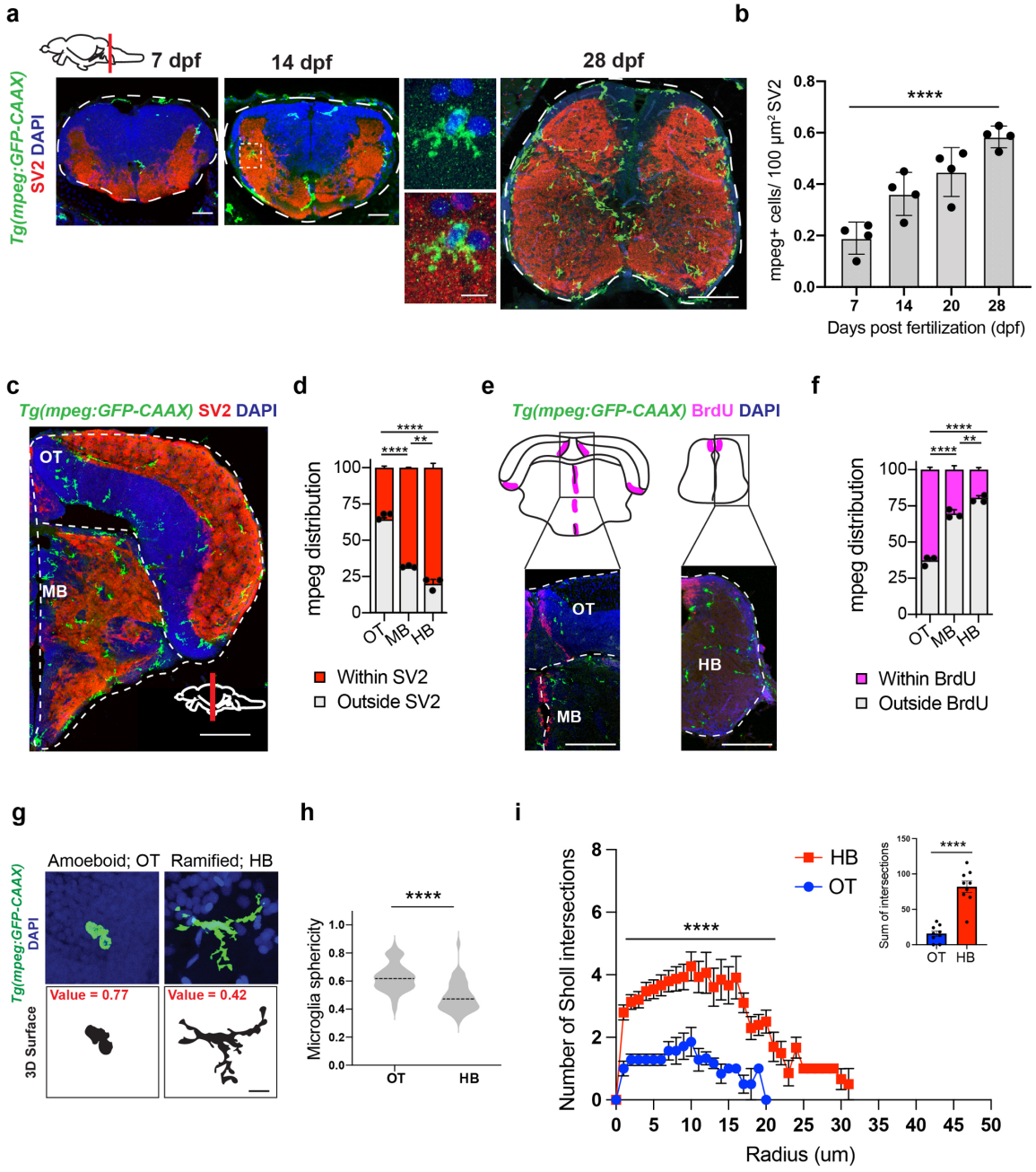

Figure 3.1. Phenotypically distinct populations of microglia in synaptic and neurogenic regions of zebrafish brain.

a) Representative images of microglia (*mpeg1.1-GFP*+) and synapses (SV2 antibody stain) in developing zebrafish hindbrain. Inset: representative synapse-embedded microglia at 14 dpf. Scales: 7-14 dpf, 20µm; 28 dpf, 50µm; inset, 5µm. All images are representative of the n=4 replicates. **b)** Quantification of *mpeg1.1-GFP* + cells per 100 µm^2 of SV2+ synaptic area at 7,14, and 28 days post fertilization. Dots represent 4 individual fish, data are mean ± SD. One way ANOVA *p < 0.0001. **c-d)** Representative images and quantification of the proportion of *mpeg1.1-GFP* + cells in synaptic (SV2+; red) vs. cellular (DAPI+/SV2-; grey) areas. Distribution quantified within each brain region as outlined (dotted lines): midbrain (MB), optic tectum (OT), and hindbrain (HB, see panel a). Mean ±SEM from n=3 fish. Two way ANOVA with Tukey's post-hoc comparison; ****p<0.0001, **p<0.0029. Scale: 50µm. **e-f)** Representative images and quantification of the proportion of *mpeg1.1-GFP*+ cells within 20 µm of BrdU+ neurogenic regions (purple) vs. outside neurogenic regions (grey). Mean ±SEM from n=3 fish. Two way ANOVA with Tukey's post-hoc comparison; ****p<0.0001, **p<0.0062. Scale: 50µm. **g)** Representative images of *mpeg1.1-GFP*+

microglia and thresholded maximal projections in OT and HB at 28 dpf. Value = Sphericity; Scale 0-1, 1=most spherical/ameboid. 5µm. Images are representative of respective values indicated in red. **h)** Quantification of microglial sphericity from images thresholded as in G. n= 50 microglia per region from n=4 fish. Dotted line indicates the median. Two-tailed unpaired t-test; ****p<0.0001). **i)** Sholl analysis quantifying number of intersections (y-axis) measured at 1µm increments from the soma (x-axis) in microglia from optic tectum (OT) and hindbrain (HB). Total of n= 9 microglia per region from n=3 fish. Mean ±SEM. Two way ANOVA with Sidak's multiple comparison; ****p<0.0001. Inset: two-tailed unpaired t-test; ****p<0.0001**. See also Fig. S3.1.1.**

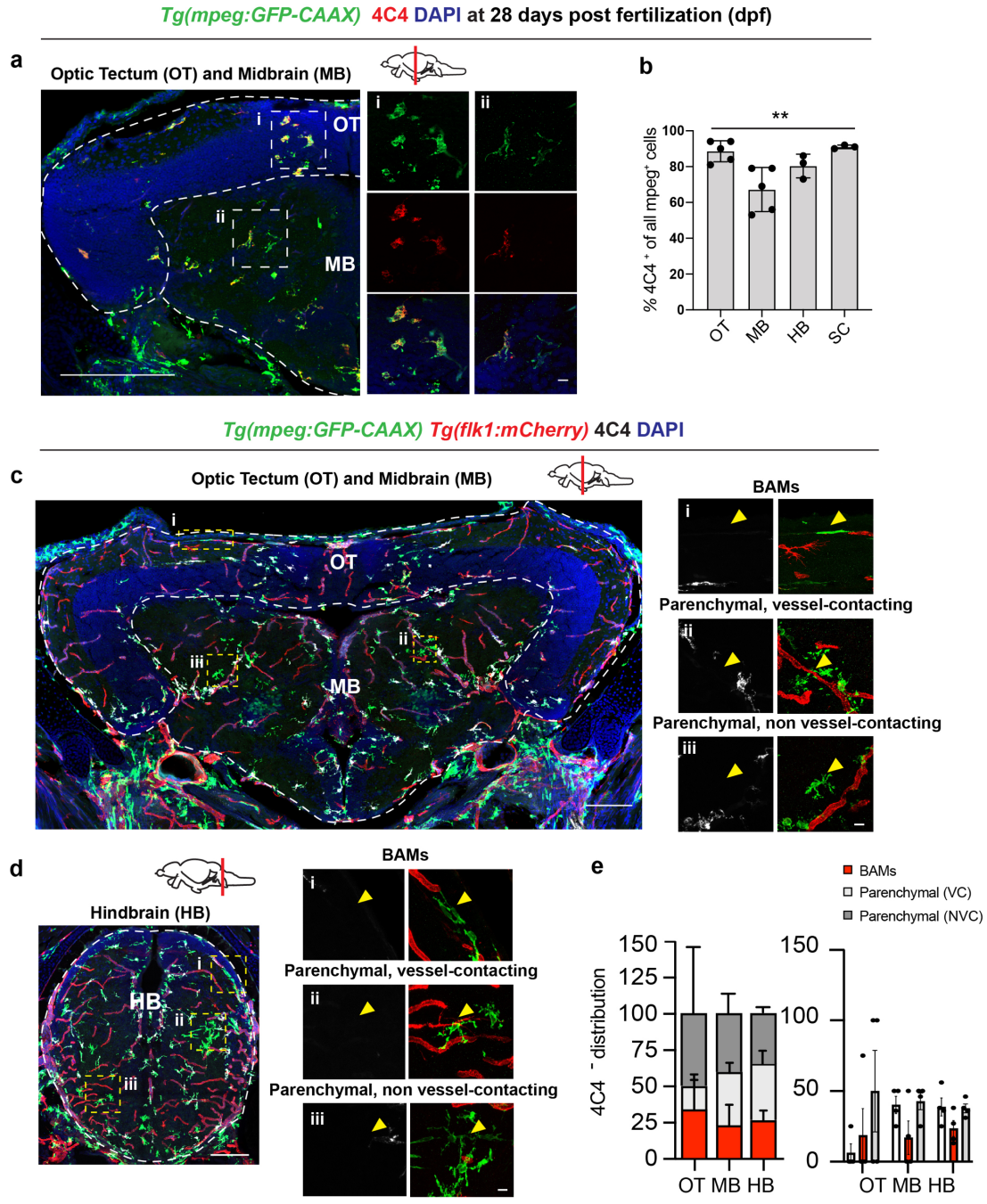

Supplemental Figure 3.1.1. Characterization of 4C4 positive and negative myeloid cells.
a) Representative images of OT and MB brain regions using the pan-myeloid reporter line *mpeg1.1:*GFP-CAAX and the commonly used antibody 4C4 to label presumptive microglia at 28 days post fertilization (dpf). Scale: 100 µm.

Optic tectum (OT), midbrain (MB), and hindbrain (HB). Insets of boxed areas show separate channels (top) and merged image (bottom) for each respective region. Scale: 10 µm. All images are representative of the n=3 replicates. **(b)** Quantification of percent of *mpeg1.1:*GFP-CAAX^{+} population also 4C4 positive. Dots represent individual fish, data are mean ± SD. One way ANOVA; ** p = 0.0047. **(c-d)** Characterization of 4C4-negative myeloid cells. Representative images using the pan-myeloid reporter line Tg(*mpeg1.1:GFP-CAAX*) crossed to vascular reporter line Tg(*flk1:mCherry*), stained with the 4C4 antibody at 30 dpf. I) Insets highlighting *mpeg1.1:* GFP-CAAX^{+} 4C4 negative border associated macrophages (BAMs) at the brain surface, ii) insets of representative *mpeg1.1:* GFP-CAAX+ 4C4-negative ramified parenchymal cell contacting a blood vessel; note, these cells lacked elongated perivascular macrophage morphology seen in mammalian PVMs. Iii) Insets highlighting a *mpeg1.1:*GFP-CAAX^{+} 4C4-negative, ramified, parenchymal, non-vessel contacting cell. Scale: 10 µm. All images are representative of the n=3 replicates. **e)** Distribution of the 4C4-negative *mpeg1.1:*GFP-CAAX^{+} cell population across the three morphologically and regionally defined subsets shown in c-d. Dots represent individual fish (n=4), data are mean ± SEM. Scale: 100 µm. Optic tectum (OT), midbrain (MB), and hindbrain (HB).

Molecularly distinct subsets of microglia identified at single cell resolution during brain development

To determine whether microglia in the zebrafish brain are molecularly heterogeneous, we performed single-cell RNA sequencing. We flow sorted hematopoietic cells from juveniles at 28 dpf using a *Tg(cd45:DsRed*) reporter (Wittamer et al., 2011) crossed with the myeloid-specific *Tg(mpeg1.1:EGFP)* reporter to ensure that all potential subsets of immune cells were captured (**Fig 3.2a, S3.2.2a**). This juvenile time-point of 28 dpf encompasses both developmental waves of embryonic and adult microglia in the zebrafish brain (Ferrero et al., 2018; Xu et al., 2015). Flow analysis indicated that 90% of *cd45*-DsRed^{+} cells were *mpeg1.1*-EGFP^{+}, and that the *cd45*-DsRed^{+} population captured all *mpeg1.1*-EGFP^{+} cells. Unbiased clustering following single cell RNA sequencing of 6,666 *cd45*-DsRed^{+} cells revealed 15 distinct clusters of hematopoietic origin, including seven non-myeloid clusters (*mpeg1.1* negative; **Fig. 3.2b, S3.2b-c**). These included clusters that expressed markers for T-cells (*cd4-1, lck*, and *ccr9a),* natural killer cells *(eomesa),* and innate lymphocyte-like cells *(il13, gata3)* (Hernández et al., 2018; Kasheta et al., 2017; Liu et al., 2017; Tang et al., 2017); **Fig. S3.2c**). Thus, multiple immune cell subsets, predominately myeloid in origin, are present in the zebrafish brain, although it is possible that some of these may be circulating rather than tissue-resident.

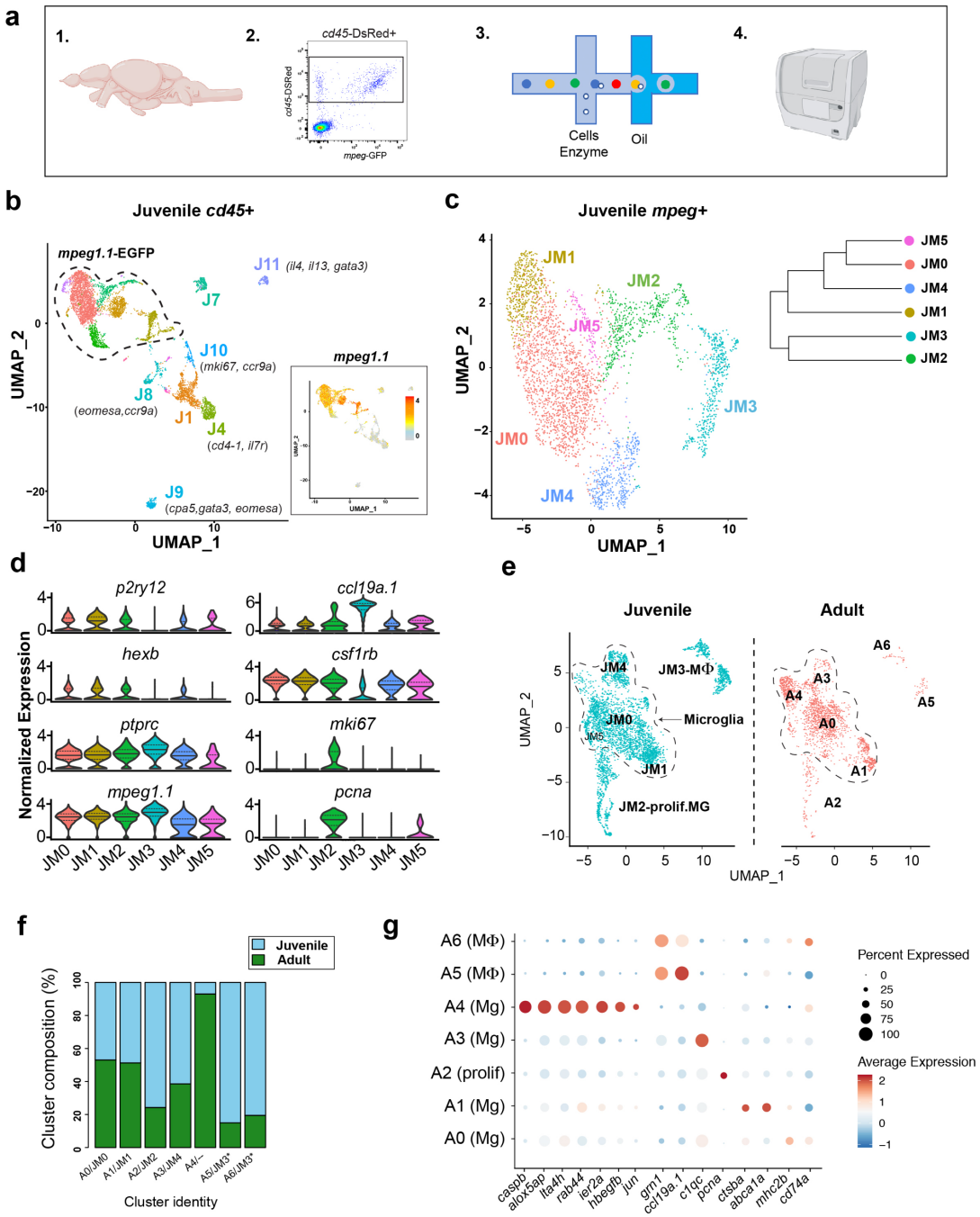

Figure 3.2. Functionally distinct subsets of microglia identified at single cell resolution during brain development and in adulthood.

a) Schematic diagram of whole brain scRNA -sequencing pipeline (items 1 and 4 adapted from BioRender.com (2020). Retrieved from https://app.biorender.com/biorender-templates. **b)** Unsupervised clustering of 6,666 juvenile *ptprc (cd45)*+ cells, colored by cluster. Inset: feature plot of *mpeg1.1* expression. N = 10 fish in two independent replicates. Color-coding for inset: normalized *mpeg1.1* expression; low expression, grey; high expression, orange. **c)** Subclustering of 3,539 *mpeg1.1*+ cells in C, colored by cluster. Inset: cluster dendrogram. **d)** Violin plots for select marker genes across juvenile clusters from C (JM1-5), including microglia (*p2ry12, hexb, csf1rb*), pan-myeloid (*mpeg1.1),* pan-hematopoietic (*ptprc/cd45),* macrophage (*ccl19a.1*) and proliferative (*mki67* and *pcna*). Colors correspond with clusters shown in Fig 2C. (Solid black line = median; dotted lines = 1st and 3rd quartiles; any lines not visible fall at 0). **e)** UMAP plots showing co-clustering analysis of juvenile cells in C (blue) and 2,080 adult (red)

myeloid (*mpeg1.1+)* cells. Datasets were merged then integrated with the Harmony R package before clustering. Conserved macrophage and proliferative clusters indicated. Dotted line outlines remaining 'homeostatic' microglial clusters. **f)** Percent of each cluster shown in E consisting of Juvenile (blue) vs. Adult (green) derived cells. Normalized within groups to account for overall cell number difference between ages. Asterisks indicate a shared juvenile cluster. **()** Dot plot highlighting select up- and downregulated genes within combined Juvenile and Adult clustering in E. Size represents percent of cells expressing each gene while color represents normalized and scaled gene expression compared to all clusters; decreased expression: blue, expression unchanged: white, increased expression: red (MAST DE algorithm in Seurat, p<0.01). **See also Fig. S3.2.2, S3.2.3**

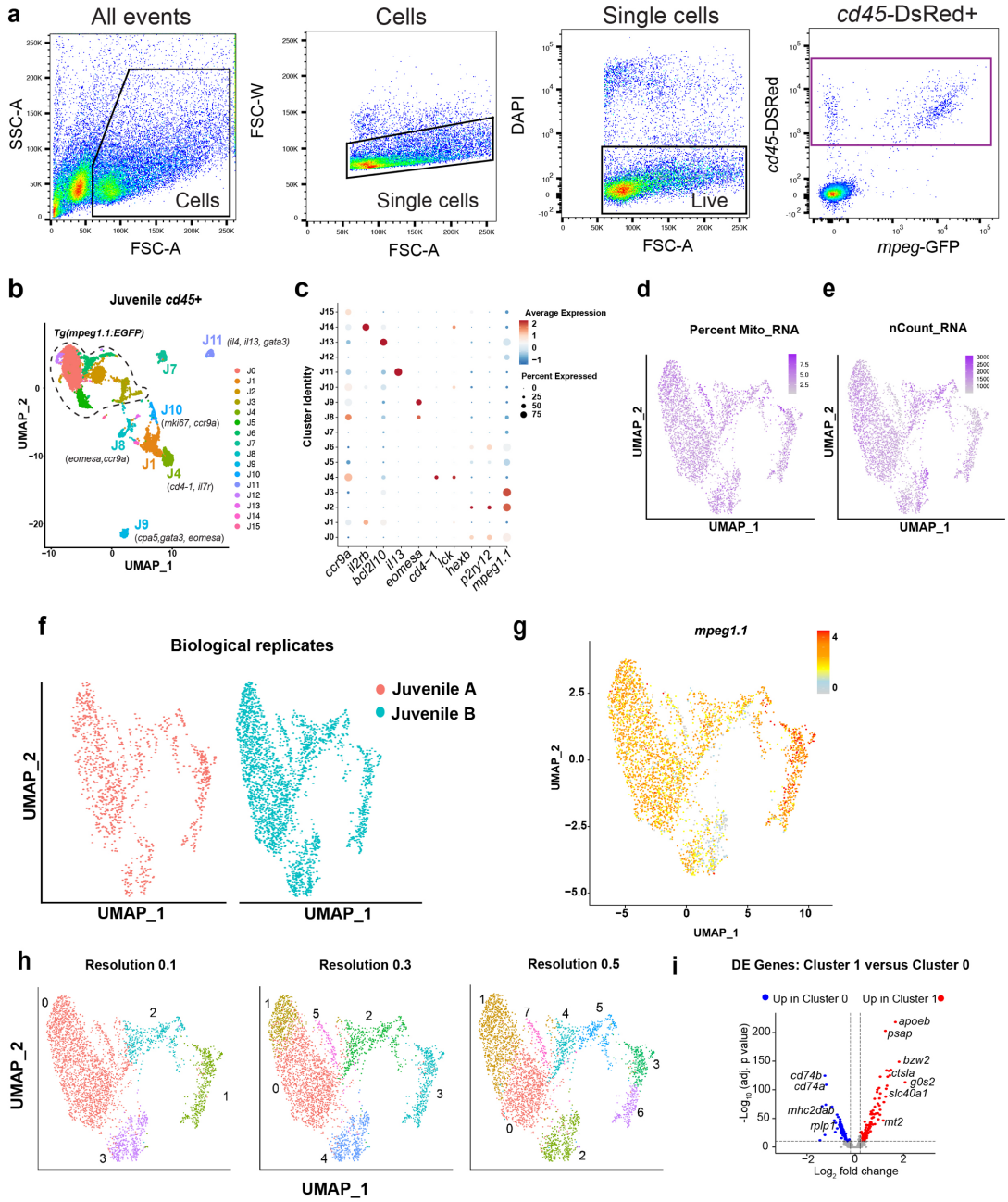

Supplemental Figure 3.2.2. Gating hierarchy and quality control of single cell sequencing data.

a) Gating strategy to isolate *cd45* positive cells for single-cell RNA sequencing data in Figure 2 a-g. The violet gate represents the total *cd45*-DsRed^{+} population that was sequenced. **b)** Unsupervised clustering of juvenile *cd45* positive

cells, replicated from Fig. 2b for reference. **c)** Select enriched genes in *cd45+mpeg1.1*$^{-}$ immune cell subsets calculated with the MAST DE algorithm in Seurat. Size represents percent of cells expressing each gene while color represents normalized and scaled gene expression compared to all clusters; decreased expression: blue, expression unchanged: white, increased expression: red. **d-e)** Feature plot showing distribution of mitochondrial RNA content and genes recovered (nCount) per cell. **f)** Comparison of independent biological replicates of *mpeg1.1*$^{+}$ cells pooled in Fig. 2c. **g)** UMAP plot highlighting levels of *mpeg1.1* expression the *mpeg1.1*$^{+}$ population from 2c. **h)** UMAP plots showing the effects of changing the clustering resolution on unsupervised clustering in Seurat with the FindClusters function. Clustering resolutions 0.1, 0.3, and 0.5 are shown. **i)** Volcano plot of differentially expressed genes between clusters JM1 (cluster 1) and JM0 (cluster 0) using a clustering resolution of 0.3. The MAST DE algorithm in Seurat was used to calculate log fold changes. Thresholds represented by dotted lines were set to adjusted p value $<10^{-10}$, log(2) fold change > 0.2.

To focus on myeloid cells, which are the dominant immune cell subset, we reclustered 3539 *mpeg1.1*$^{+}$ cells. After quality control and filtering, the myeloid subset yielded six distinct clusters (**Fig 3.2c; Fig. S3.2.2d-g**) at a clustering resolution of 0.3, which best represented the observed patterns of gene expression (**Fig. S3.2.2h-i**). We identified cluster JM3 as the macrophage subset based on the absence of microglial-specific markers (*p2ry12, csf1ra, hexb,* and *slc7a7*), the presence of *ccl19a.1 (a.k.*a. macrophage inflammatory protein), *flt3,* and *grn1* (**Fig 3.2d, Fig. S3.2.3a**), and higher levels of *mpeg1.1* (**Fig. S3.2.2g**). However, we could not definitively identify whether the JM3 macrophage cluster represented CNS-resident 'border associated' macrophages (BAMs) (Prinz et al., 2019) vs. circulating macrophages, as the zebrafish homologs of mammalian BAM genes (e.g. *cd63, mrc1b, apoc1, apoc4,* and *lyve1b)*(Utz et al., 2020) were either not detected or did not segregate as expected between microglial and macrophage subsets (**Fig. S3.2.3a**). Of the remaining microglial clusters, cluster JM2 marked a proliferating subset (*pcna* and *mki67*; **Fig 3.2d**), cluster JM5 contained too few cells to be definitively assigned, and the remaining three clusters (JM1, JM0, and JM4) had clear microglial identity but unique gene expression profiles which we further analyze below.

Next, we examined whether these subsets persist into adulthood by co-clustering the juvenile *mpeg1.1*$^{+}$ population with adult (1 year old) brain *mpeg1.1*$^{+}$ cells that were sorted and

sequenced in parallel. The datasets were integrated using the Harmony R package (Korsunsky et al., 2019) to compensate for sources of technical variation. Unbiased clustering and differential expression analysis revealed six subsets that were conserved between juveniles and adults (**Fig 3.2e**) as well as a distinct adult-enriched microglial cluster (A4; **Fig 3.2f**). Notably, adult cluster A3 mapped to juvenile cluster JM4 (conserved genes included *cebpb, c1qa, c1qb,* and *c1qc*), whereas adult cluster A1 mapped to juvenile cluster JM1 (*apoeb* and *ctsba*). A proliferative cluster was still present (A2; *pcna, tubb2b,* and *mki67*), as well as two distinct macrophage clusters (A5 and A6) corresponding to juvenile cluster JM3 (*ccl19a, siglec15l,* and *cmklr1*). Interestingly, the adult-enriched cluster A4 was distinctly enriched in inflammasome genes, suggesting a microglial subset poised for inflammasome activation (*caspb, fads2, and alox5ap*; **Fig 3.2g**). Taken together, these data reveal myeloid cell heterogeneity in the juvenile zebrafish brain that persists into adulthood.

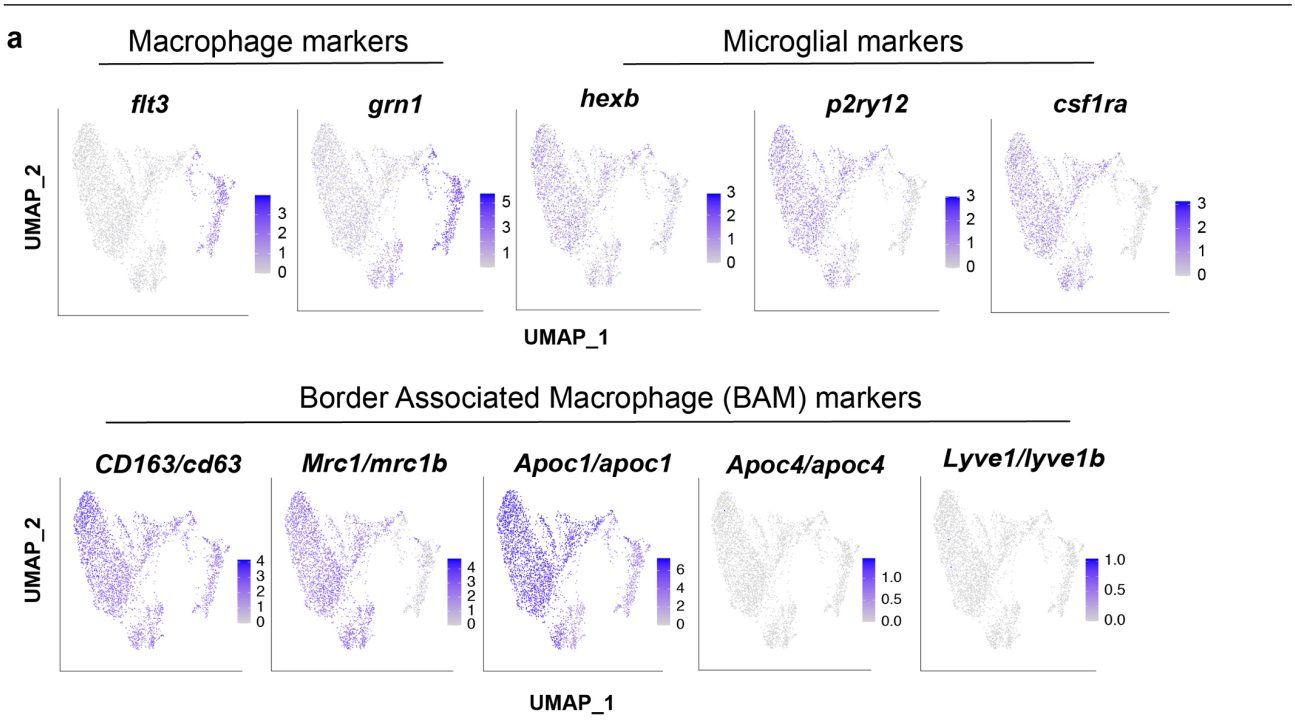

Supplemental Figure 3.2.3: Feature plots of macrophage, microglia, and mammalian BAMs.
a) Feature plots from juvenile single-cell RNA dataset from Fig. 2C, showing canonical macrophage and microglia markers (top), and several proposed mammalian border associated macrophage (BAM) signature genes(Utz et al., 2020), (Van Hove et al., 2019) with known homologs in fish (labels indicate mammalian/zebrafish homologs, bottom).

Region-specific transcriptional signatures of juvenile zebrafish myeloid cells

Previous zebrafish transcriptomes using the *Tg(mpeg1.1:EGFP*) transgenic line and bulk sequencing approaches have suggested regional transcriptional heterogeneity within the zebrafish brain (Wu et al., 2020). To better compare our single cell data with the existing literature (Mazzolini et al., 2020; Oosterhof et al., 2017), we isolated *mpeg1.1*-EGFP^{+} myeloid cells from the OT, midbrain, and hindbrain at 28 dpf by flow cytometry and performed bulk RNA sequencing (**Fig 3.3a, Fig. S3.3.4a**). The resulting transcriptome was highly enriched for microglial specific genes (*csf1rb, c1qa, p2ry12*), as well as some macrophage markers (*siglec15l*, *spock3)*. This was a pure myeloid population with no detectable evidence of neuronal, astrocyte, or oligodendrocyte genes (**Fig. S3.3.4b**). Principal component analysis revealed that 60% of gene variance was driven by brain region (PC1; **Fig 3.3b**), and differential expression analysis of these subsets ($p<0.05$) identified region specific gene expression signatures (**Fig 3.3c**). In particular, complement and antigen presentation genes were enriched in the hindbrain (*c1qa, c1qc*, *cd74a, mhc2dab*), whereas lysosome-associated genes were highly enriched in the OT (*apoeb, ctsba, ctsc*, *ctsla*). The midbrain was intermediate and did not clearly segregate with either phenotype.

We confirmed region-specific expression for two candidate genes from this profile via *in situ* hybridization (ISH). *Cd74a* was expressed in over 90% of hindbrain microglia (*mpeg1.1*-GFP^{+} 4C4^{+}) and 30% of OT microglia, with intermediate expression in the midbrain (**Fig 3.3d-e**). In contrast, *ctsba* was highly enriched in neurogenic areas and highest in the OT compared to midbrain and hindbrain (72%, 33%, 19%, respectively; **Fig 3.3f-g**). These data reveal brain-region specific transcriptional signatures that can be identified *in situ*. However, they also suggest that

these differences may be partly driven by varying proportions of phenotypically distinct microglia as well as resident macrophages that are better discriminated at single-cell resolution.

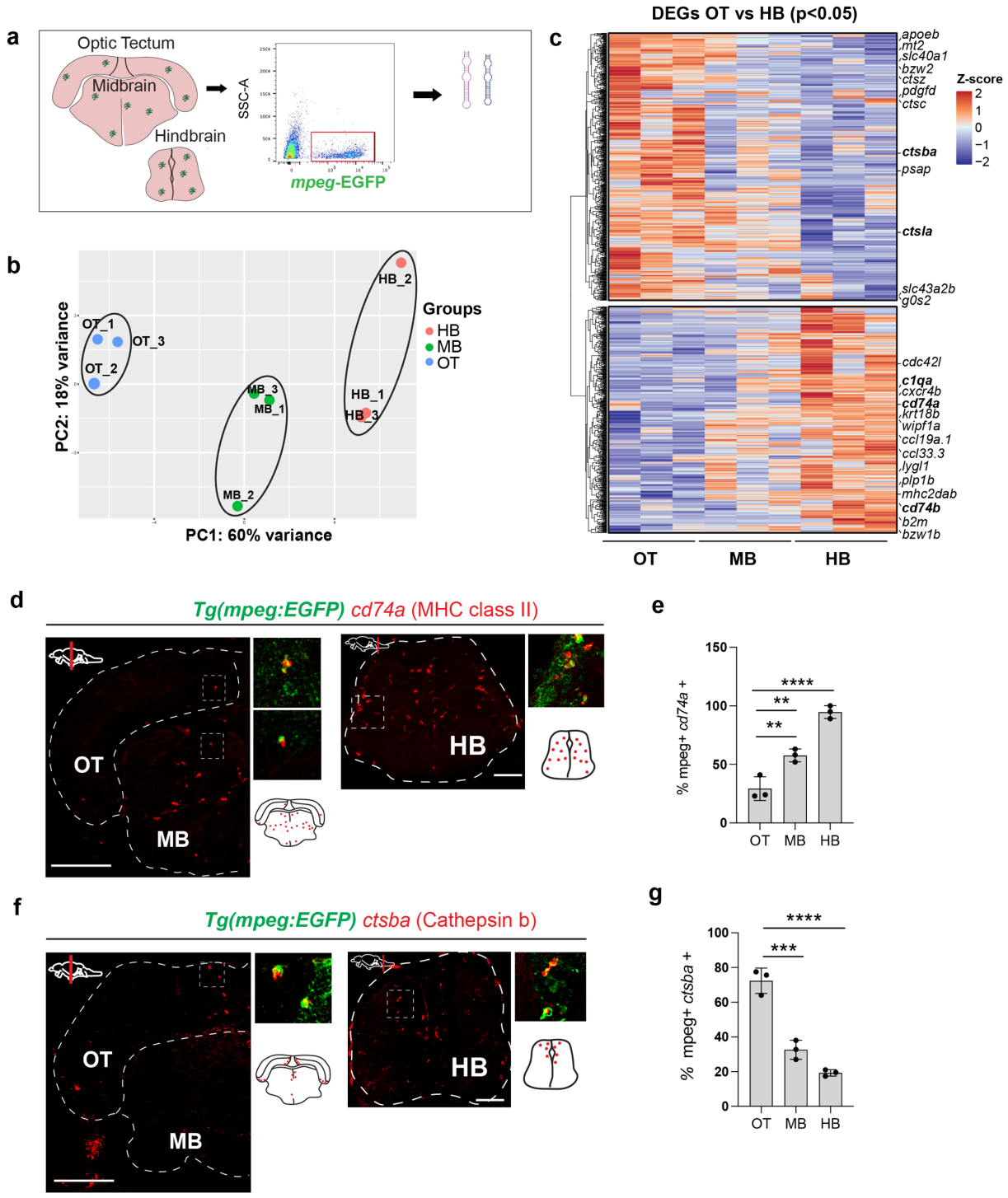

Figure 3.3. Region specific transcriptional signatures of juvenile zebrafish myeloid cells.
() Schematic of region-specific bulk-sequencing approach using *Tg(mpeg1.1:EGFP)*. **(b)** Principal component analysis (PCA) plot of top 500 most variable genes for OT, MB, HB regions (dots= independent replicates from 10

pooled fish/replicate). **(c)** Heatmap of differentially expressed genes (DEGs) from *mpeg1.1*-EGFP positive cells across brain regions (Adjusted p-value <0.05). Selected top differentially expressed genes from each cluster highlighted. Color-coding, decreased expression; blue, no expression; white, high expression; red. **d-e)** Representative images and quantification of *cd74a* expression across brain regions by *in situ* hybridization (ISH), co-localized with *mpeg1.1*-GFP+. Quantification shows percentage of *cd74* + *mpeg1.1*-GFP+ microglia within each brain region. Dots represent 3 individual fish, data are mean ± SD. One way ANOVA with Tukey's post hoc test. **p<0.0079, ****p<0.0001, **p<0.0021. Scale: 50µm. All images are representative of the n=3 replicates. **f-g)** Representative images and quantification of *ctsba* expression by ISH colocalized with *mpeg1.1*-GFP. Quantification shows percentage *ctsba*+ *mpeg1.1*-GFP+ microglia within each brain region. Dots represent 3 individual fish, data are mean ± SD. One way ANOVA with Tukey's post hoc test. ***p<0.0003, ****p<0.0001. Scale: 50 µm. All images are representative of the n=3 replicates. **See also Fig. S3.3.4.**

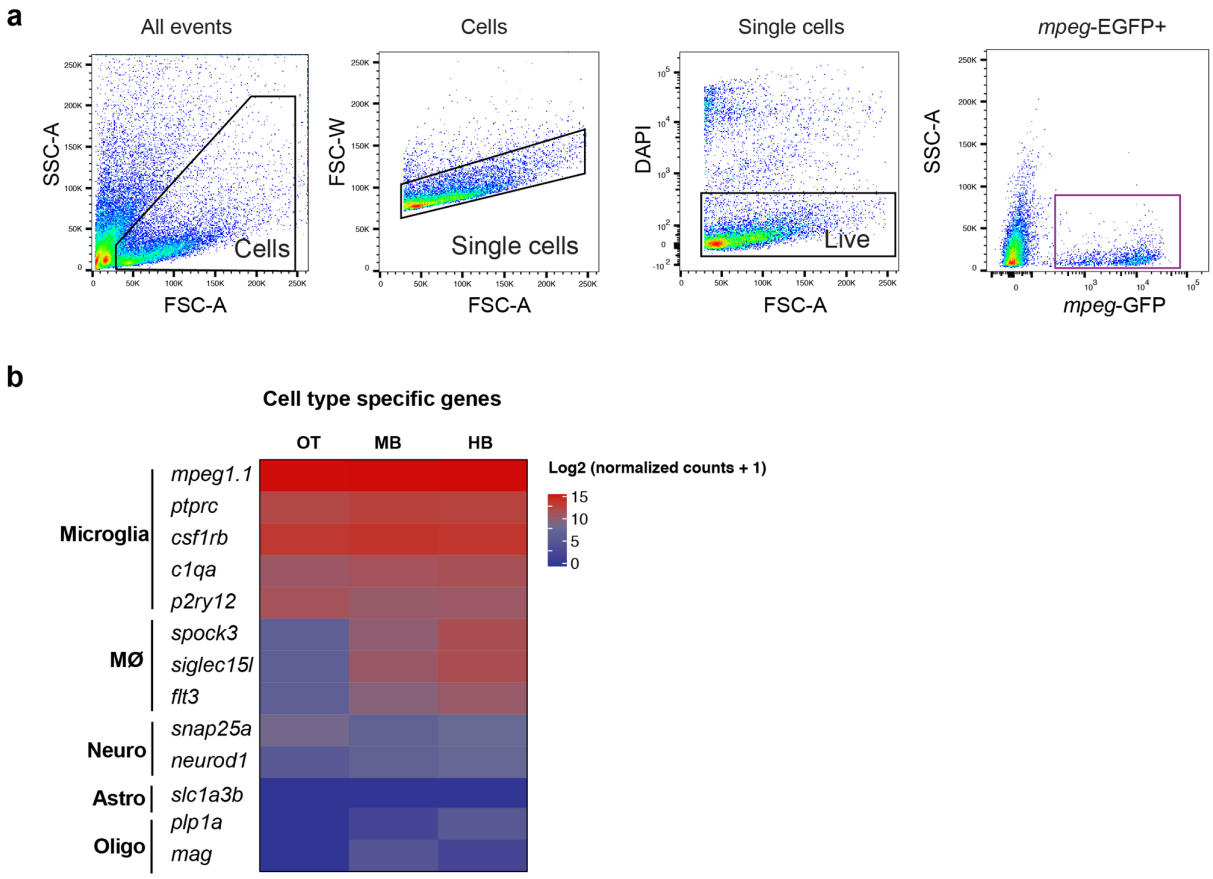

Supplemental Figure 3.3.4. Gating strategy and quality control of bulk sequencing data in Figure 3.3. **a)** Gating strategy to isolate *mpeg1.1*-EGFP^{+} myeloid cells for region-specific bulk sequencing data in Figure 3A-C. The violet gate represents the *mpeg1.1*-EGFP^{+} population that was sequenced. **b)** Heatmap of selected microglia, macrophage, neuronal, astrocyte, and oligodendrocyte genes. Optic tectum (OT), midbrain (MB), and hindbrain (HB). Log-normalized counts generated with DESeq2.

Region-enriched functional microglial subsets in zebrafish hindbrain and optic tectum

We next used the region-specific transcriptional signatures to map the single cell data, with the goal of localizing functional subsets *in situ* (**Fig 3.4a**). To do this, we calculated an "eigengene"

composed of the top differentially expressed genes in the *mpeg1.1:*EGFP^{+} population from each region. Overlay of these region-defining eigengenes onto our UMAP plot revealed enrichment of the OT signature in the juvenile cluster JM1, whereas the hindbrain eigengene was enriched in JM4 and the macrophage cluster JM3 (**Fig 3.4b-c**). The midbrain regional signature was indeterminate and aligned only with the macrophage cluster, consistent with our finding of substantially more macrophages in this region (**Fig. S3.1.1b**). Cluster JM0 was not enriched in any regional signature, suggesting that it may represent either a common microglial population or a subset not represented in our bulk sequencing. The OT-enriched cluster JM1 and the hindbrain-enriched cluster JM4 were distinct in both bulk and single-cell sequencing and did not contain macrophages, so we directly compared the transcriptomic profile of these subsets (**Fig 3.4d-e**).

Genes that defined the hindbrain-enriched cluster (JM4) included *c1qa*, the initiating protein in the complement cascade and a known regulator of synaptic engulfment expressed in rodent microglia (Fonseca et al., 2017; Stephan et al., 2012). Another cluster-defining gene was *cebpb*, a transcription factor that promotes microglial homeostasis in neurodegenerative disease (Ndoja et al., 2020). Other upregulated genes included the hindbrain region defining gene *cd74b,* which encodes the invariant chain of major histocompatibility complex class II, and *grn1,* which encodes progranulin and interacts with C1q to regulate synaptic pruning (Lui et al., 2016). We also identified several putative functional genes not previously studied such as the lysozyme gene *lygl1*. Gene ontology analysis suggested that the preferentially expressed genes in cluster JM4 are involved in protein production and metabolism, including translational elongation, negative regulation of proteolysis, and protein folding (**Fig 3.4d-e**). In contrast, the OT-enriched cluster JM1 was highly enriched for lysosomal activity, including multiple genes for lysosomal proteases including cathepsins (*ctsba, ctsz, ctsla, ctsc*, and *ctsd*) as well as higher levels of *apoeb* and

lgals9l1. Thus, functional subsets identified by scRNA sequencing correlate with the differentially enriched populations of synapse-associated and neurogenic-associated microglia that we identified *in situ*.

We hypothesized that hindbrain-enriched cluster JM4 represents a synapse-associated microglia subset, whereas OT-enriched JM1 preferentially associates with neurogenic regions. To identify our putative OT-enriched cathepsin-rich cluster (JM1) *in situ*, we quantified functional cathepsin activity with the biomarker Prosense 680, which becomes fluorescent after proteolytic cleavage by cathepsins with a preference for cathepsin B and L (Weissleder et al., 1999). Microglial cathepsin activity (*mpeg1.1*-EGFP^{+} Prosense^{+}) was highly enriched in the OT, where it was mostly detected in ameboid microglia around neurogenic regions (**Fig 3.4f-g**), closely matching the expression of *ctsba* by *in situ* hybridization (**Fig 3.3f-g**). Consistent with this, OT microglia engulfed substantially more cell corpses than hindbrain microglia, as quantified by uptake of a neuronal-soma enriched DsRed *Tg(NBT:DsRed)*; **Fig. S3.4.5a-b**). Next, we quantified synapse engulfment by 3D reconstruction of *mpeg1.1*-EGFP positive cells with the synaptic marker SV2. We found that hindbrain microglia engulfed significantly more SV2 than OT microglia, consistent with enrichment of the JM4 cluster in hindbrain (**Fig 3.4h-i**). Importantly, stratifying this data by morphology revealed that ramified microglia (sphericity <0.6) engulfed more SV2 regardless of brain region, although they were markedly more abundant in the hindbrain. These data suggest functional subsets whose abundance differs between brain regions, rather than strictly region-specific functions. Taken together, we conclude that our cathepsin-enriched cluster JM1 corresponds to cell corpse-engulfing microglia highly enriched in neurogenic regions, whereas complement-expressing cluster JM4 identified a synapse-associated subset.

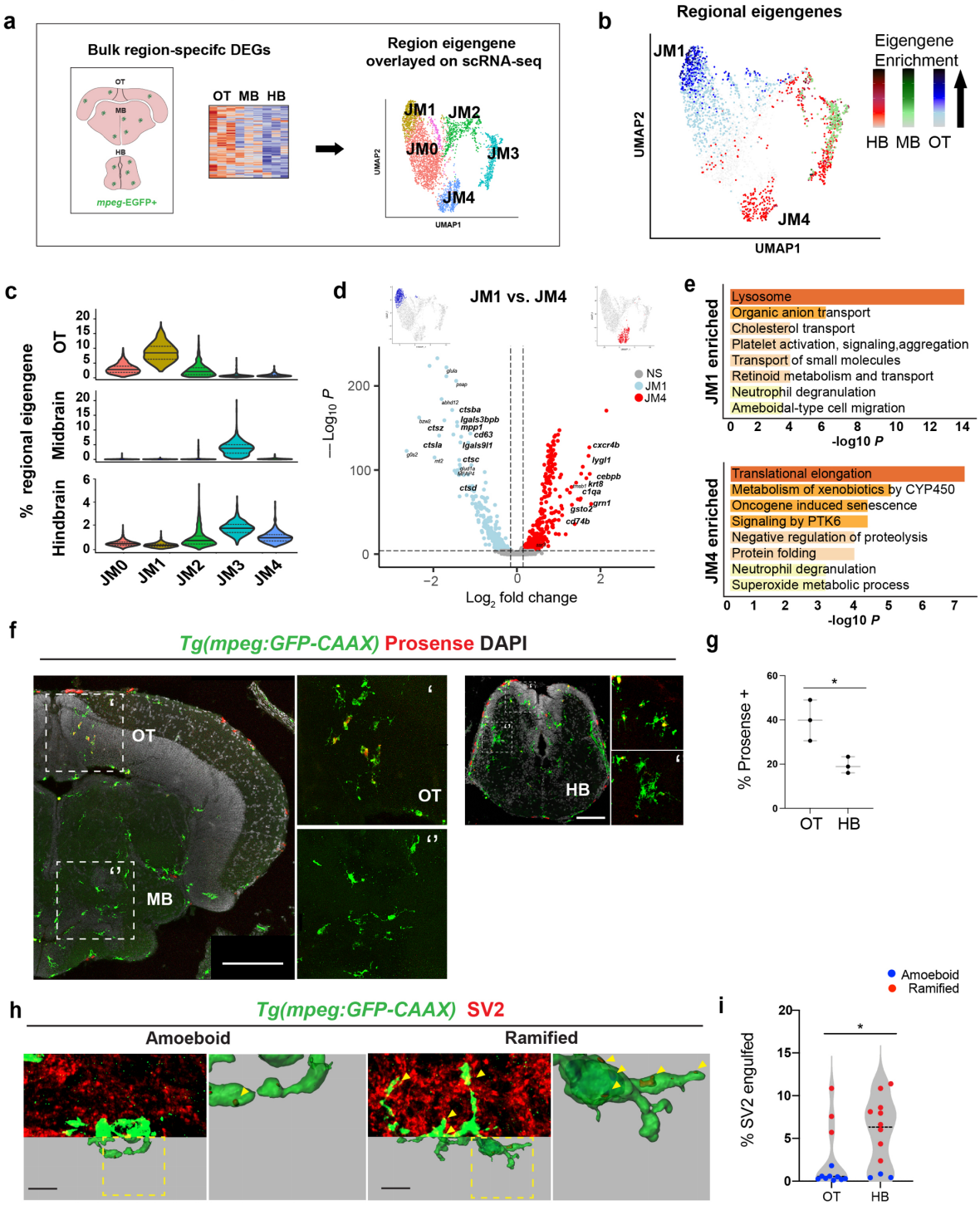

Figure 3.4. Region-enriched functional microglial subsets in zebrafish hindbrain and optic tectum.
a) Schematic of analysis pipeline overlaying brain-region defining genes identified with bulk sequencing onto *mpeg1.1*+ scRNA sequencing clusters. Colors correspond to clusters defined in Fig. 2C. **b)** Feature plots of region-defining eigengenes from hindbrain (HB; red), midbrain (MB; green) and optic tectum (OT; blue) overlaid on *mpeg1.1*+ UMAP, highlighting microglial clusters JM1 and JM4. Eigengenes were composed of single region marker genes with regional enrichment (log_2 fold change > 1.2, basemean > 100, and adj. $p < 0.05$) from the bulk sequencing analysis in figure 3 and computed with the PercentageFeatureSet function in the Seurat R package. Color-coding for

Eigengene expression: OT, low expression; light blue, high expression; dark blue. MB, low expression; light green, high expression; dark green. HB, low expression; pink, high expression; red. **c)** Violin plots of regional eigengene distributions, related to B. Colors correspond with clusters shown in Fig. 2C, 4A. (Solid black line = median; dotted lines = 1st and 3rd quartiles). **d)** Volcano plot of differentially expressed genes between clusters JM1 (OT-enriched; blue) and JM4 (hindbrain-enriched; red). Thresholds represented by dotted lines were set to adjusted p value $<10^{-8}$, log fold change > 0.2. (MAST differential expression test with Bonferroni correction; See Supplemental S5). **e)** Top GO terms from differentially expressed genes in d. (Metascape; hypergeometric test with Benjamini-Hochberg correction for multiple comparisons). **f)** Representative images of cathepsin-cleaved Prosense 680 colocalized with *mpeg1.1*-EGFP in indicated brain regions. Scale: 100 µm. Images are representative of the n=3 replicates. **g)** Quantification of total percent microglia containing cleaved Prosense680 in OT and HB. Unpaired t-tests. Dots represent 3 individual fish, data are mean ± SD. *p<0.0236. OT (Optic Tectum) and HB (Hindbrain). Two-tailed unpaired t-test. **h)** Representative images and 3D reconstructions of *mpeg1.1*-EGFP+ microglia with engulfed SV2 protein. Insets: close-up of reconstructions (arrowheads:SV2 content). Scale bar 5 µm. Images are representative of amoeboid or ramified morphology. **i)** Quantification of percent microglial volume containing SV2 in randomly selected microglia from OT and HB. Post hoc analyses show morphology assignment as ramified (red, sphericity<0.6) vs. amoeboid (blue, sphericity >0.6. Mann Whitney u-test, *p < 0.0177, dots= mean value per fish from 3 microglia per fish. **See also Fig. S3.4.5 and Fig. S3.4.6.**

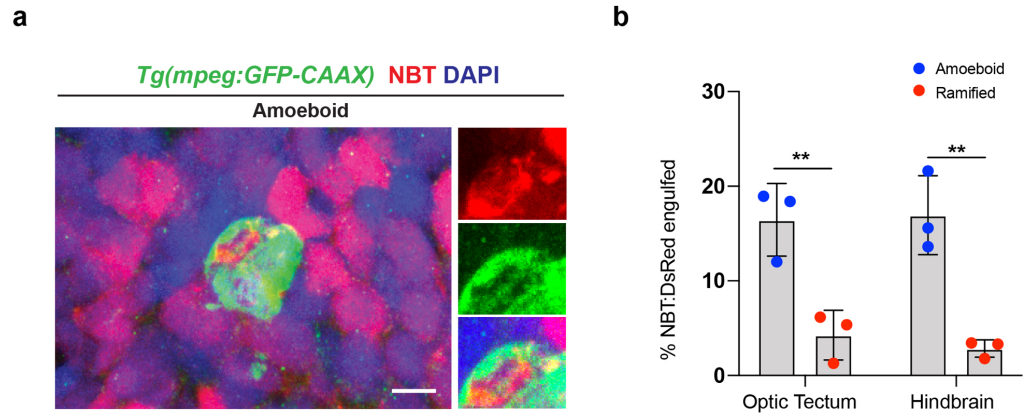

Supplemental Figure 3.4.5. Neuronal engulfment in the OT and HB at 28 dpf.
a-b) Representative image and quantification of *NBT*:DsRed neuronal bodies within ramified or amoeboid microglia (Sphericity > .6) from OT and HB brain regions. Two separate t-tests, **p < 0.01, n=3 microglia per fish; n=3 represented as mean values. Scale bar: 10 µm. All images are representative of the n=3 replicates.

We performed additional analyses to assess lineage relationships and determine whether these functional subsets were conserved across species. To examine predicted lineage relationships, we performed pseudotime analysis with Monocle 3 (Cao et al., 2019; Qiu et al., 2017; Trapnell et al., 2014). This suggested that adult-specific cluster A4, NAMs, and SAMs each represent distinct end points derived from precursors that include the proliferating and putative homeostatic clusters A2/JM2 and A0/JM0 (**Fig. S3.4.6a**). To determine whether these subsets could be identified in the developing human brain, we compared the clusters to a published human fetal microglia dataset (**Fig. S3.4.6b**; (Kracht et al., 2020)). We found that 71% (750/1054) of the

human cluster marker genes analyzed had at least one zebrafish homolog. Using these genes, we found a strong correlation between human fetal cluster 6 (dividing cells) and zebrafish cluster JM2 (dividing cells); additionally, human fetal clusters 3 (enriched in gestational weeks 11-12) and 5 (immediate early gene-expressing microglia) had significant overlap with NAM cluster JM1. Together, the NAM-overlapping clusters (3 and 5) represented 20% of cells.

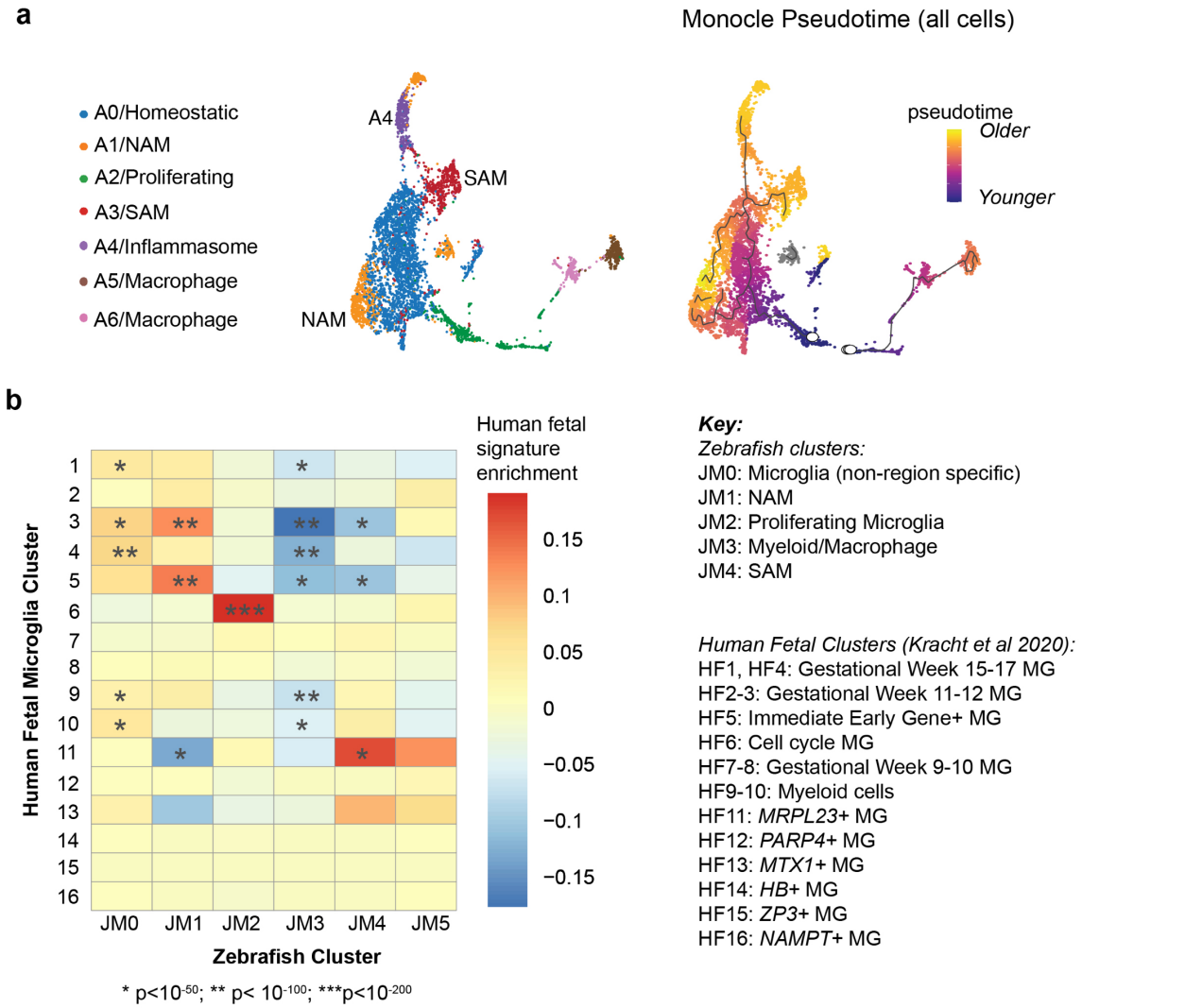

Supplemental Figure 3.4.6. Human fetal microglia (Kracht et al., 2020) comparison to juvenile zebrafish microglia and pseudotime analysis.
a) Pseudotime analysis with Monocle 3 (Cao et al., 2019) on both juvenile and adult *mpeg1.1* positive cell populations. Left UMAP plot is colored by cluster, right colored by estimated pseudotime using dividing cells as a starting point. **b)** Heatmap comparing juvenile zebrafish microglial clusters to a single-cell human fetal microglia dataset (Kracht et al 2020, table S3)(Kracht et al., 2020). Cells are colored by signature enrichment (estimated increase in average eigengene expression calculated with the AddModuleScore function in Seurat) in the listed zebrafish cluster compared to all other zebrafish clusters. (Two-sided Wilcoxon Rank-Sum Test, *$p<10^{-50}$, **$p<10^{-100}$, ***$p<10^{-200}$).

A smaller, less well characterized cluster (<3% of cells) shared a gene signature with SAM cluster JM4. From this we conclude that NAM-like cells can be identified in a human fetal dataset, whereas SAMs are either rare at this developmental stage or less functionally discrete in the human fetal brain. Thus, these functional subsets of microglia have a conserved gene signature that is at least to some extent detectable across species.

Discussion

Here we define the regional localization and molecular signatures of two distinct microglial phagocytic states in the developing zebrafish, including a subset of synapse-associated microglia (SAMs) abundant in the hindbrain (**Fig 3.5a-b**). We also identify several other immune populations, including a subset of macrophages. However, due to the possible presence of circulating cells in the sample, and limited conservation between zebrafish and mammalian CNS macrophage markers, future targeted investigations of these non-microglial populations are warranted. Nonetheless, this functionally annotated microglial single cell dataset presents an opportunity to investigate fundamental questions related to interactions between microglia and synapses. For example, microglia both engulf synapses and promote synapse formation via modification of the extracellular matrix and other mechanisms (Colonna and Butovsky, 2017; Nguyen et al., 2020; Wolf et al., 2017), but the molecular regulators of these different states are not well understood. The impact of neuronal activity on microglial function is also a major area of interest: microglial synapse engulfment has been proposed to be activity-dependent, and in both fish and rodents microglial contact can acutely regulate neuronal activity (Badimon et al., 2020; Li et al., 2012). However, observing these processes in the intact developing brain is challenging

in rodents and is a major strength of the zebrafish model. This molecularly defined population of synapse-associated microglia in the zebrafish hindbrain provides an opportunity to temporally define and genetically manipulate these microglial subsets in physiological and disease contexts.

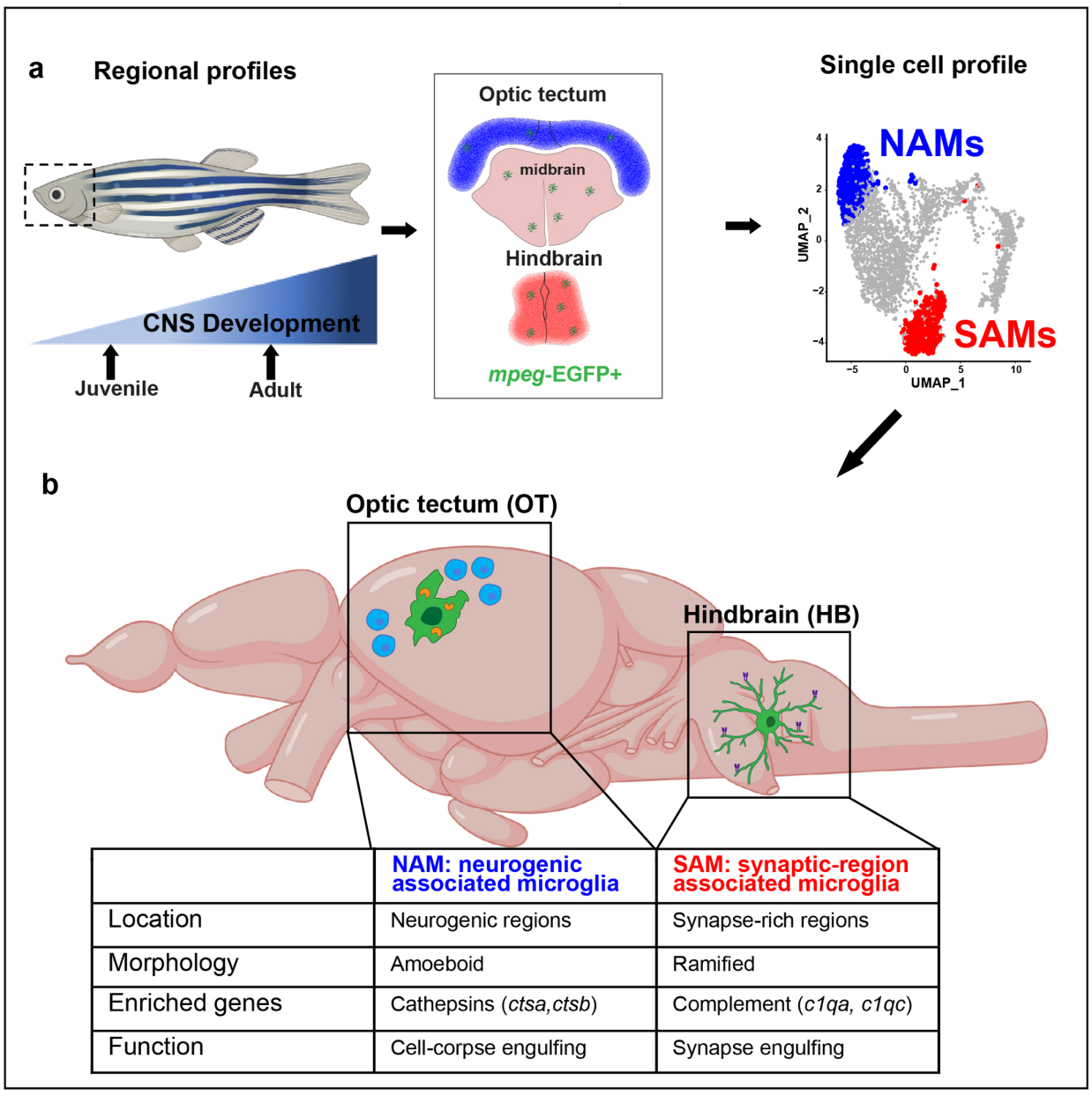

	NAM: neurogenic associated microglia	SAM: synaptic-region associated microglia
Location	Neurogenic regions	Synapse-rich regions
Morphology	Amoeboid	Ramified
Enriched genes	Cathepsins (*ctsa,ctsb*)	Complement (*c1qa, c1qc*)
Function	Cell-corpse engulfing	Synapse engulfing

Figure 3.5. Summary diagram of the identified neurogenic-associated microglia (NAMs) and synaptic-region associated microglia (SAMs) in the developing zebrafish brain.
a) Schematic of analysis pipeline overlaying brain-region defining genes identified with bulk sequencing onto *mpeg1.1*+ scRNAseq clusters identifies NAMs and SAMs. **b)** Unique features of NAMs and SAMs in the developing juvenile brain. Adapted from BioRender.com (2020). Retrieved from https://app.biorender.com/biorender-templates.

Importantly, we show that both SAMs and NAMs are phagocytic *in vivo*, but in different contexts and via distinct molecular mechanisms. Our observations regarding NAMs are consistent with several recent publications. For example, deficits in lysosomal function lead to defective cell corpse phagocytosis and dysmorphic 'bubble microglia' in the OT (Villani et al., 2019). Another study used bulk RNA sequencing to identify *ccl34b.1* as a marker of ameboid microglia with high phagocytic capacity in the adult zebrafish (Wu et al., 2020). Interestingly, *ccl34b.1* is also strongly enriched in our NAM subset, suggesting that these represent similar or overlapping populations, and possibly that the ontogenetic origins of those microglia as described in that study may be linked to their distinct functions, although further work would be required to definitively establish this. Our studies of functional cathepsin activity suggest *in vivo* approaches to track lysosomal function in this population. More importantly, we have identified genes associated with microglia localized to synaptic regions of the zebrafish CNS. The initiating components of the classical complement cascade (*c1qa* and *c1qc*) are top differentially expressed genes in our SAM subset. C1q is also microglial-encoded in the murine brain and in multiple vertebrate species including zebrafish (Fonseca et al., 2017; Geirsdottir et al., 2019) and promotes developmental synaptic engulfment (Stevens et al., 2007). Other top candidates, including the transcription factor *cebpb* and major histocompatibility complex, class II (*cd74a & cd74b*), have been implicated in rodent models of Alzheimer's disease (Mathys et al., 2017; Ndoja et al., 2020). These data suggest that the SAM profile identifies a core microglial program conserved across species, and raise the question of how other gene candidates, including *lygl1, grn1*, *fgl2a* and others, are regulating microglial-synaptic interactions.

Our data highlight evolutionarily conserved features of zebrafish microglia as well as unique strengths of the zebrafish model. It is striking that developmental microglial heterogeneity in the fish is largely conserved into adulthood, in contrast to generally diminishing amounts of diversity in adult rodents (Hammond et al., 2019; Li et al., 2019a). This may reflect the fact that fish continue to grow in size throughout life, adding new neurons and new synaptic connections. This conservation suggests that the time window for studying microglial roles in circuit formation may be much broader than in mammals, and that mechanisms may exist to maintain synaptic plasticity throughout life. Future studies focusing on the microglial-synapse interactions in the zebrafish hindbrain can take advantage of co-existing populations of cell-corpse engulfing and synaptic-region associated microglia to further define the differences between these subsets. Our data also suggest that live-imaging of microglia-synapse interactions may help to answer key questions about how and why microglia interact with synapses. Finally, the ability to do high throughput screening in zebrafish raises the possibility that this model could be used to define therapeutic targets in neurodevelopmental diseases linked to immune dysfunction including autism spectrum disorder, epilepsy, and schizophrenia.

Acknowledgements: We are grateful to Marci Rosenberg, Haruna Nakajo, and members of the Molofsky Lab for helpful comments on the manuscript, to Ari Molofsky, Tom Nowakowski and Galina Popova for their expert advice, and to Brian Black, Gary Moulder and Louie Ramos for the support of the CVRI Zebrafish Core facility. Thanks to Francesca Peri for the Tg(*mpeg1.1:GFP-CAAX*) fish, David Traver for the *Tg(cd45:DsRed)* fish, and Roland Wu for the *Tg(mpeg1.1:EGFP)* fish, and to the UCSF Laboratory for Cell Analysis and Dr. Eric Chow at Center for Advanced Technologies for technical contributions. **Funding*:*** A.V.M is supported by the Pew Charitable Trusts, NIMH (R01MH119349 and DP2MH116507), and the Burroughs Welcome Fund. N.J.S. is supported by UCSF-IRACDA (K12GM081266) fellowship. L.C.D. received support from the Matilda Edlund Scholarship and the Genentech Fellowship.

Data and materials availability: The single-cell RNA sequencing and bulk RNA sequencing data generated in this study have been deposited in the NCBI Gene Expression Omnibus database under accession code GSE164772 and GSE164771, respectively. The data are unrestricted. A searchable database is provided at https://www.annamolofskylab.org/microglia-sequencing. The human fetal microglia data analyzed in this study were downloaded from Table S3 of a previously published article (Kracht et al., 2020). Any additional information required to reanalyze the data reported in this paper is available from the lead contact upon request.

Code availability: All code used to analyze sequencing data can be found at https://github.com/lcdorman/zebrafish2021.

Methods

Experimental model and subject details: All animal protocols were approved by and in accordance with the ethical guidelines established by the UCSF Institutional Animal Care and Use Committee and Laboratory Animal Resource Center (LARC). Wild-type, AB strain zebrafish (*Danio rerio*; ZIRC, University of Oregon, Eugene, OR) were propagated, maintained, and housed in recirculating habitats at 28.5°C and on a 14/10-h light/dark cycle. Embryos were collected after natural spawns, incubated at 28.5°C and staged by hours post fertilization (hpf). Juveniles used were 28 days of age, a time in development before sex determination. Adults of either sex were used at 12 months of age. Ages were matched within experiments. The transgenic reporter lines, *Tg(cd45:DsRed)* and *Tg(mpeg1.1:EGFP)* was used to identify hematopoietic lineage and mononuclear phagocytes (Ellett et al., 2011; Wittamer et al., 2011)..

Immunohistochemistry: Tissues were fixed overnight at 4°C in 0.1M phosphate buffered 4% paraformaldehyde, cryoprotected with 20% sucrose, and embedded in optimal cutting temperature (OCT) medium (Sakura Finetek). Immunohistochemistry (IHC) was performed on 20-µm-thick sections collected on a cryostat and mounted onto glass slides (Silva et al., 2020). Sections were washed in phosphate buffered saline with 0.5% Triton-x (PBST) and incubated with 20% heat-inactivated normal goat serum in PBST for 2 hours (NSS; Sigma-Aldrich, Corp.). Primary antibodies were applied overnight at 4°C, all antibody dilutions and catalog numbers are listed in **Table 3.2**. Sections were then washed with PBST and incubated in secondary antibodies for 1 hour at room temperature. Prior to IHC for BrdU, sections were immersed in 100°C sodium citrate buffer (10 mM sodium citrate, 0.05% Tween 20, pH 6.0) for 30 minutes and cooled at room temperature for 20 minutes. IHC was performed as described above.

Labeling neurogenic zones: In juveniles, dividing cells were labeled with BrdU by housing animals in system water containing 5 mM BrdU for 24 hours prior to collection(Silva et al., 2020).

In situ* Hybridization:* Digoxigenin (DIG)-labeled riboprobes for *cd74a* and *ctsba* was generated by PCR amplification using primers containing the T3 or T7 promoter sequences. Full sequences available in Supplemental Table 3.2. 20-µm-thick sections were hybridized with riboprobes at 55°C, incubated with an alkaline-phosphatase-conjugated anti-DIG antibody and visualized using Fast Red TR/Naphthol AS-MX (SIGMA*FAST*) as the enzymatic substrate. When *in situ* hybridizations were combined with BrdU IHC, sections were removed from the fast red solutions, rinsed and post-fixed in buffered 4% paraformaldehyde for 10 minutes then processed for BrdU IHC as described above.

ProSense680 injections: Fish were injected with 2 nL of ProSense680 at a concentration of 20 nM using a nanospritzer with a fire pulled glass pipette connected directly into the lateral ventricle of the brain and returned to system water immediately following injections. Fish were euthanized 24 hours post injection and processed for immunohistochemistry as stated above.

Microglia morphology quantitation: Z-stack images of *mpeg1.1:*EGFP + and 4C4 staining were acquired with a step size of 0.5µm using a 63x objective (NA 1.4) on an LSM 800 Confocal Microscope (Zeiss) spanning a thickness of 20 µm. Microglia sphericity and Sholl intersections were quantified using Imaris software (Bitplane) by creating 3D surface reconstructions of

mpeg1.1-EGFP^{+}-4C4^{+} microglia. All images were set to a standard threshold to accurately maintain morphology for quantifications.

Microglia engulfment assay: Images were acquired with an LSM 800 Confocal Microscope (Zeiss) using the same parameters as described above. Imaris software (Bitplane) was used to generate 3D surface rendering of microglia, which were then masked for *NBT*-DsRed or SV2 channels within that microglia. Masked channels were then 3D rendered to obtain volume data. *NBT*-DsRed and SV2 engulfment was calculated per cell as the volume of SV2 or *NBT*-DsRed divided by the volume of the microglia.

Fluorescence activated cell sorting (FACS): For bulk RNA-sequencing of juvenile 28 dpf *Tg(mpeg1.1:EGFP)* zebrafish, the optic tectum, midbrain and hindbrain were dissected (10 zebrafish were pooled per sample). For scRNA-sequencing of 28 dpf *Tg(mpeg1.1:EGFP): Tg(cd45:DsRed)* juveniles (10 zebrafish pooled per lane) and 1 year old *Tg(mpeg1.1:EGFP): Tg(cd45:DsRed)* adults (3 zebrafish pooled per lane) whole brains were dissected. To isolate microglia and other *cd45*+ cells, the brain(s) (regions) were mechanically dissociated in isolation medium (1x HBSS, 0.6% glucose, 15 mM HEPES, 1 mM EDTA pH 8.0) using a glass tissue homogenizer (VWR). Subsequently, the cell suspension was filtered through a 70 μm filter (Falcon) and pelleted at 300 g, 4ºC for 10 minutes. The pellet was resuspended in 22% Percoll (GE Healthcare) and centrifuged at 900 g, 4ºC for 20 minutes (acceleration set to 4 and deceleration set to 1). Afterwards, the myelin free pellet was resuspended in isolation medium that did not contain phenol red. Prior to sorting on a BD FACS Aria III, the cell suspension was incubated with DAPI (Sigma). For bulk RNA-sequencing, microglia were gated on FSC/SSC

scatter, live cells by DAPI, and *mpeg1.1:*EGFP+. After sorting, cells were spun down at 500 g, 4°C for 10 min and the pellet was lysed with RLT+ (Qiagen). For scRNA-sequencing, microglia, macrophages and *cd45*+ cells were collected by gating on FSC/SSC scatter, live cells by DAPI, and all *cd45:*DsRed (which included both *mpeg1.1:*EGFP+ and negative subsets). After sorting, cells were spun down at 500 g, 4°C for 10 min and resuspended in PBS + 0.05% BSA (Sigma).

Bulk RNA-sequencing of microglia: RNA was extracted using the Rneasy® Plus Micro kit (Qiagen) from RLT+ lysed microglia. RNA quality and concentration were measured using the Agilent RNA 6000 Pico kit on an Agilent Bioanalyzer. All samples had an RNA Integrity Number (RIN) >8. For each sample, a total of 10 ng of RNA was loaded as input for cDNA amplification and library construction using the QuantSeq 3' mRNA-Seq Library Prep Kit FWD for Illumina (Lexogen) following manufacturer's instructions. Library quality was determined with the Agilent High Sensitivity DNA kit on an Agilent Bioanalyzer and concentrations measured with the Qubit™ dsDNA HS Assay Kit (Thermo Fisher) on a Qubit™ (Thermo Fisher). Library pools were single-end (65-bp reads) sequenced on two lanes using an Illumina HiSeq 4000 yielding 40-50 million reads per sample.

Bulk RNA-sequencing analysis: Quality of reads was assessed using FastQC (http://www.bioinformatics.babraham.ac.uk/projects/fastqc). All samples passed quality control and reads were aligned to *Danio rerio* GRCz11.98 genome (retrieved from Ensemble) using STAR (version 2.5.4b) (Dobin et al., 2013) with '—outFilterMultimapNmax 1' to only keep uniquely mapped reads. Uniquely mapped reads were counted using HTSeq (version 0.11.1) (Anders et al., 2015). Subsequently, the DESeq2 package (version 1.28.1) (Love et al., 2014) in R software was

used to normalize the raw counts and perform differential gene expression analysis. Batch correction was done using the Limma package (version 3.44.3) (Ritchie et al., 2015) and heatmaps were made using ComplexHeatmap package (version 2.4.3) (Gu et al., 2016). Metascape was used for gene ontology analysis (Zhou et al., 2019).

Single cell RNA-sequencing: Single cells were isolated as described above. Approximately 15,000 cells were loaded into each well of Chromium Chip B (v3), libraries were prepared using the 10x Genomic Chromium 3' Gene Expression Kit in-house as described in the Manual and sequenced on two lanes of the NovaSeq SP100 sequencer for an average depth of 30,000-50,000 reads per cell. BCL files are converted to Fastq, then used as inputs to the 10X Genomics Cell Ranger 2.1 pipeline. Samples were aligned to the GRCz11.94 (danRer11) zebrafish reference genome. Clustering and differential expression analysis were conducted using Seurat version 3.1.4 (Butler et al., 2018; Satija et al., 2015). Cells outside of the thresholds listed in the table were excluded from downstream analysis (**Table 3.1**).

Table 3.1: Single Cell Sequencing Parameters

	Whole Brain Juvenile Isolation	**Whole Brain Adult Isolation**
Number of cells	Loaded: 20,000 Total passing QC: 6666 *mpeg1.1:*EGFP+: 3539	Loaded: 10,000 *mpeg1.1:*EGFP+ after QC: 2336
Biological replicates	10 fish	3 fish
10x lanes	2	1
Age	28 days post fertilization	1 year post fertilization
10x chip kit	V3	V3
Thresholds	500-3500 genes/cell; 1200-15000 transcripts/cell; 0-10% mitochondrial transcripts	500-3500 genes/cell; 1200-15000 transcripts/cell; 0-10% mitochondrial transcripts

Counts were log normalized (scale factor = 10,000) and scaled in Seurat, regressing out number of genes detected (nFeature_RNA). The top 6000 most variable genes (calculated with the vst method in Seurat) were used to calculate 50 principal components, and the top 30 PCs were used for nearest neighbor, UMAP, and cluster calculations with the resolutions shown in the table. Individual cell types were identified through calculation of marker genes using the MAST test (version 1.16.0) (Finak et al., 2015) for genes expressed in at least 20% of cells in the cluster and a natural log fold change of 0.2 or greater and adjusted p value less than 10^-8. The microglial and macrophage clusters were isolated based on expression of *cd45* (*ptprc*) and *mpeg1.1*. Normalization, clustering, and differential gene expression was recalculated for each sample (juvenile, juvenile *mpeg1.1:*EGFP^{+}, adult and juvenile *mpeg1.1:*EGFP^{+}) on genes expressed in 10% or more cells per cluster. P-values were calculated for genes with a natural log fold change >0.2 and genes with an adjusted p-value < 0.001 were used for further analysis. GO analysis was conducted using the Metascape webpage (www.metascape.org)(Zhou et al., 2019). Adult and juvenile datasets were combined using Harmony (version 1.0) (Korsunsky et al., 2019). Bulk vs single cell analysis was conducted using the following thresholds for bulk sequencing results: adj. $p< 0.05$, $\log_2$ fold change > 1.2, basemean > 100. Following thresholding, only genes uniquely enriched in one region were used to calculate "eigengene" values determined with Seurat's "PercentageFeatureSet" function.

Psuedotime analysis was conducted with Monocle 3 (version 1.0.0) (Cao et al., 2019; Qiu et al., 2017; Trapnell et al., 2014) with batch correction for age and regression of percent mitochondria and total RNA counts per cell using Batchelor (version 1.6.3) (Haghverdi et al., 2018). All other default parameters were used, and dividing cells were selected as the starting point for Psuedotime calculations.

Comparison with human fetal microglia(Kracht et al., 2020) was conducted by converting gene IDs from the differentially expressed genes per human fetal cluster calculated by the authors in table S3 (average log fold change > 0.25, adjusted p-value < 0.05) into homologous zebrafish genes using biomaRt (version 2.46.3). 354 of 1054 human genes were un-annotated and excluded from the calculation. The converted gene IDs were then used to calculate an eigengene/module score (Seurat's AddModuleScore function) for each human fetal (HF) cluster on all juvenile *mpeg1.1*+ microglia. Correlations between HF and JM clusters was conducted using a 2-sided Wilcoxon rank-sum test for each HF cluster compared to all JM clusters 0-5. The test estimate for each comparison was used to create a heatmap, and asterisk labels represent associated p-values for the comparison of each specific JM cluster's enrichment in HF cluster score compared to all other JM clusters.

Quantification and statistical analysis

GraphPad Prism 8.3.0 was used for all histological quantification analyses. Statistical tests are described in text and figure legends. RNA-sequencing data was analyzed in R as described above. Two-sided unpaired t-tests were used in comparing two groups in which the data were normally distributed, datasets with more than two groups were analyzed with one way or two-way repeated measures ANOVA as appropriate.

Table 3.2: List of key reagents and software packages

REAGENT or Software package	SOURCE	IDENTIFIER
Antibodies		
Chicken anti-GFP 1:1000	Aves Labs	Cat#GFP-1020, RRID: AB10000240
Rabbit anti-DsRed 1:1000	Takara Bio	Cat#632496; RRID: AB-_10013483
Mouse anti-synaptic vesicle glycoprotein 2A (SV2) 1:500	DHSB	RRID: AB_2315387
Rat anti-BrdU 1:500	Abcam	Cat#ab6326; RRID: AB_305426
Mouse anti-4C4 1:200	Gift from Hitchcock Lab	Cat#92092321; RRID: AB_10013752
Anti-Digoxigenin-AP, Fab Fragments 1:500	Roche	Cat#11093274910, RRID: AB_2734716
Alexa Fluor 488 goat anti-chicken 1:500	Thermo Fisher	Cat#A-11039; RRID: AB_2534096
Alexa Fluor 555 goat anti-mouse 1:500	Thermo Fisher	Cat#A-21422, RRID: AB_141822
Alexa Fluor 555 goat anti-rabbit 1:500	Thermo Fisher	Cat# A-21429; RRID: AB_2535850
Alexa Fluor 647 goat anti-mouse 1:500	Thermo Fisher	Cat# A-21235; RRID: AB_2535804
Alexa Fluor 647 goat anti-Rat 1:500	Thermo Fisher	Cat# A-21248; RRID: AB_2535816
Critical Commercial Assays		
Chromium single cell gene expression platform, version 3	10x Genomics	Library and gel bead kit-V3, 120267: Chip B kit:1000009
SIGMAFAST Fast Red TR/Naphthol AS-MX Tablets	Sigma-Aldrich	C# F4648
ProSense 680 Fluorescent Imagining Agent	PerkinElmer	C#NEV10003
Deposited Data		
Single cell RNA-Sequencing of microglia from juvenile and adults	Gene Expression Omnibus	GSE164771
Bulk RNA-sequencing of microglia from OT, MB, HB brain regions	Gene Expression Omnibus	GSE164772

Experimental Models: Organisms/Strains	**SOURCE**	**IDENTIFIER**
Zebrafish*: Tg(mpeg1.1:EGFP)*	(Ellett et al., 2011)	ZFIN: ZDB-ALT-0000
Zebrafish*: Tg(cd45:DsRed)*	(Wittamer et al., 2011)	
Oligonucleotides		
cd74a ISH primers,	In house	F: TAATACGACTCACTATAGGGGGACAGGAGAAACTCAAGG;R: AATTAACCCTCACTAAAGGGCCATCCCAAACAACATGC
ctsba ISH primers,	In house	F: TAATACGACTCACTATAGGGATGCAAGAGAGCAGTGG; R: AATTAACCCTCACTAAAGGGAAGTCCAATGAGCAGGTC
Seurat (Version 3.1.4)	(Satija et al., 2015)	https://satijalab.org/seurat
STAR (Version 2.5.4b)	(Dobin et al., 2013)	https://github.com/alexdobin/STAR/releases
DESeq2 package (Version 4)	(Love et al., 2014)	hhtp://www.bioconductor.org/packages/release/bioc/html/DESe2.html
Harmony (Version 1.0)		
ImageJ	NIH	RRID: SCR_003070
Imaris	Oxford Instruments	RRID: SCR_007370
Prism	GraphPad	RRID: SCR_002798

Chapter 4: A type I interferon response defines a conserved microglial state required for effective neuronal phagocytosis

---

Summary

Microglia, the innate immune cells of the brain, are exquisitely sensitive to dynamic changes in the neural environment. Using single cell RNA sequencing of the early postnatal murine somatosensory cortex after partial whisker removal, we identified a type I interferon (IFN-I) responsive microglia population that expanded following the induction of topographic remodeling. We found that IFN-I responsive microglia expressing the marker IFITM3 actively engulf whole neurons. Loss of IFN-I signaling (*Ifnar1*$^{-/-}$) resulted in dysmorphic 'bubble' microglia with enlarged phagolysosomal compartments. We also observed a reduction in dead cells and an accumulation of neurons with double strand DNA breaks, a marker of cell stress. Conversely, IFN-I gain of function in zebrafish was sufficient to drive increased neuronal engulfment by microglia. We identified IFITM3+ microglia in two murine disease models: SARS-CoV-2 infection and the 5xFAD model of Alzheimer's disease. These data reveal a novel role for IFN-I signaling in regulating efficient neuronal clearance by microglia.

Introduction

Neural circuits undergo dynamic and experience dependent changes in circuit connectivity during brain development, and even subtle alterations in this process are associated with neurodevelopmental diseases (Arguello and Gogos, 2012; Bitzenhofer et al., 2021; Forrest et al., 2018; Medendorp et al., 2021). Glial cells, including astrocytes and microglia, are essential to physiological neural circuit development and function (Allen and Lyons, 2018; Vainchtein and

Molofsky, 2020). Microglia in particular are of emerging interest due to their multiple roles in circuit development, including promoting synapse elimination, driving synapse formation, and engulfing whole cells (Frost and Schafer, 2016; Prinz et al., 2019). Yet despite this clear evidence of functional heterogeneity, defining the links between gene expression and function remains an active area of investigation (Hammond et al., 2019; Li et al., 2019a). One potential reason why these connections are still not completely defined is that glial heterogeneity can be transient, context-dependent, and difficult to capture. For example, while microglia broadly belong to a PU.1-dependent myeloid lineage, much of what distinguishes subsets of microglia from each other depends on dynamic responses to local factors, including cytokines, neuronal activity, and damage-associated molecular patterns (Badimon et al., 2020; Gosselin et al., 2014, 2017; Lavin et al., 2014; Vainchtein and Molofsky, 2020). Thus, defining how CNS contextual cues alter glial states is critical to linking genes to function, particularly for physiological responses that are continuously fine-tuned to maintain homeostasis (Chovatiya and Medzhitov, 2014).

In this study, we challenged the developing murine somatosensory system with altered sensory input via whisker-follicle cauterization (Erzurumlu and Gaspar, 2012; Van Der Loos and Woolsey, 1973; Sehara et al., 2010) in order to elicit glial responses to an acute but non-inflammatory re-ordering of the neural environment. Single-cell sequencing of somatosensory cortical microglia during the subsequent topographic remapping (https://www.annamolofskylab.org/microglia-sequencing) led to the identification of a population of type I interferon (IFN-I) responsive microglia population that was actively engulfing whole neurons *in situ*. Our data suggest that IFN-I is required for effective microglial phagocytosis, and that in the developing brain, an IFN-I responsive state is associated with clearance of damaged but not yet terminally injured neurons. The IFN-I signature we identified is also detected across

pathologies ranging from viral infections to Alzheimer's Disease, raising the possibility that they represent a distinct phagocytic state in those settings. More broadly, our data reveal the potential of single cell transcriptomics following a defined physiological perturbation to identify novel functional subsets of microglia.

Results

Microglia and astrocytes alter their transcriptomes in response to cortical remapping

To elicit glial phenotypes in response to physiologic changes in local circuits, we adapted a well-established barrel cortex remodeling paradigm. Facial whisker lesion before postnatal day 4 (P4) leads to irreversible structural alterations of the cortical topographic map, whereby thalamocortical synapse and cell-rich regions (barrels) separated by septa rearrange around the new sensory input space (Baldi et al., 2000; Erzurumlu and Gaspar, 2012; Jeanmonod et al., 1981; Van Der Loos and Woolsey, 1973; Sehara and Kawasaki, 2011; Sugimoto et al., 1999; Woolsey and Wann, 1976). Importantly, because the whisker somatosensory circuit synapses in the brainstem and the thalamus *en route* to the cortex, whisker follicle lesioning leads to circuit remodeling without inducing injury responses in the cortex (**Fig. 4.1a**). This paradigm captures astrocytes and microglia during a period of active proliferation and maturation. Cortical astrocytes are present by P0, but proliferate and elaborate their processes between P0-P30 (Stogsdill et al., 2017). Microglia populate the barrel cortex septa between P3 and P5, with full invasion of the barrel centers by P7 (Hoshiko et al., 2012). Microglia engulf barrel cortex synapses in response to complete whisker follicle ablation (Gunner et al., 2019a), suggesting that this paradigm may be useful for studying microglial phagocytic responses.

To elicit rearrangement but not elimination of the whisker map, we unilaterally cauterized 40% of the facial whiskers by removing follicles in alternating rows (B and D) at P2. We examined

responses at P5 and P7, following layer 4 barrel coalescence at ~P3-P5 (**Fig. 4.1a**; (Rebsam et al., 2002; Rice et al., 1985)). For this and all subsequent experiments, we compared contralateral deprived barrel cortex with ipsilateral spared cortex as an internal control. As expected, neonatal whisker removal led to redistribution of the VGLUT2+ thalamocortical axonal boutons in cortical layer 4, whereby the deprived cortical rows (B and D) were smaller with indistinct barrel separation (**Fig. 4.1b,** (Sehara et al., 2010)). This was reflected as a decreased ratio of VGLUT2 intensity between barrels and septa in layer 4 (**Fig. 4.1c**). However, mean VGLUT2 intensity across the entire barrel cortex was not significantly different, suggesting that despite redistribution, overall thalamocortical synapse density was preserved (**Fig. 4.1d, Fig. S4.1.1a**). Therefore this model may elicit different microglial states compared to full unilateral whisker loss, which leads to progressive dimming of VGLUT2 intensity (Gunner et al., 2019b). Microglial and astrocyte density were unchanged (**Fig. S4.1.1b-e**), and we did not detect any evidence of morphologic or molecular changes often associated with injury responses as measured by GFAP and Iba1 intensity respectively (**Fig. S4.1.1f-i**). We conclude that this model leads to a reorganization of the structure of the barrel cortex without provoking gross changes in synapse numbers.

To survey the response of all glia to this topographic remodeling at higher resolution, we performed single cell RNA sequencing of non-neuronal cells in microdissected somatosensory cortex. We used cold protease digestion at 4°C (Adam et al., 2017) to dissociate the tissue, which preserved most non-neuronal subsets. We found that relative to papain digestion at 34°C, this strategy increased the relative expression of microglial *P2ry12,* which has been associated with a homeostatic microglial state, and substantially decreased expression of *Tnf,* which can be induced in inflammatory or reactive conditions (**Fig. S4.1.2a-c**). Fluorescence-activated cell sorting (FACS) was used to recover live cells and enrich microglia ($CD11b^{+}/CD45^{lo}$) to 30% of total cells

before single cell sequencing on the 10x Chromium V2 platform, in which each cell is captured in a droplet so that a cell-specific barcode can be added to each mRNA before sequencing (**Fig. 4.1e, S4.1.2d-g**). After quality control (**Fig. S4.1.2h-j, Table 4.1**), unbiased clustering revealed clusters specific to astrocytes, microglia, oligodendrocyte lineage cells, endothelial cells, and pericytes, whereas neurons were largely depleted (n= 1,777 cells from 2 biological replicates; **Fig. 4.1f-h, Fig. S4.1.1k**). We did not detect changes in cell numbers, except for an increase in oligodendrocyte progenitor cells (OPC; **Fig. S4.1.3a-b**), as reported previously (Mangin et al., 2012).

Notably, both astrocytes and microglia – but not endothelial or oligodendrocyte lineage cells – showed transcriptomic shifts following whisker deprivation (**Fig. 4.1i**). The astrocytes split into two clusters, one of which (cluster 5) consisted mainly of cells from the control hemisphere, while the other (cluster 1) consisted primarily of deprived cortex. Subclustering and differential gene expression analysis on these astrocyte clusters revealed deprivation-induced enrichment of genes critical for synapse formation including *Sparcl1*, which stabilizes nascent synapses (Singh et al., 2016), and regulators of cholesterol biosynthesis necessary for synapse formation and glutamate homeostasis (*Cyp51* and *Hmgcs1)* (Ferris et al., 2017; Mauch et al., 2001; Pfrieger, 2003; Tsai et al., 2006; Valenza et al., 2015). Extracellular matrix components and regulators which contribute to barrel remodeling were also enriched (*Bcan, Tnc, Htra1*; (Cybulska-Klosowicz et al., 2004; McRae et al., 2007); **Fig. 4.1j, Fig S4.1.3c-e)**. Fluorescent *in situ* hybridization validated the deprivation-induced increase in *Htra1*, a secreted protease which degrades extracellular matrix (**Fig. 4.1k-l**; (Grau et al., 2006; Lin et al., 2018; Murwantoko et al., 2004; Tsuchiya et al., 2005)). Microglia showed a more complex response to remodeling than astrocytes, prompting us to examine them at higher resolution.

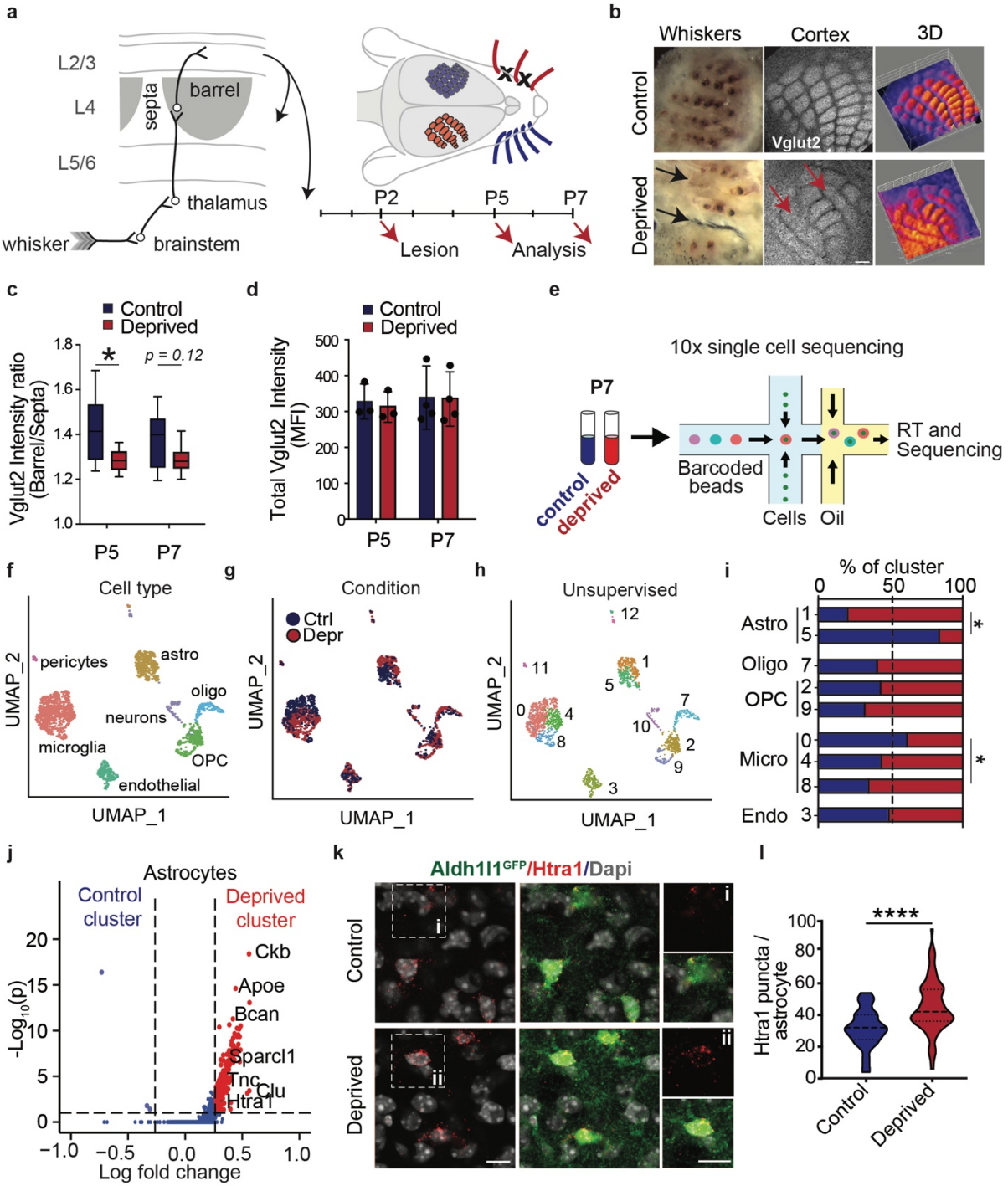

Figure 4.1: Microglia and astrocytes alter their transcriptomes in response to cortical remapping.
a) Schematic of barrel cortex connectivity and experimental timeline. **b**) Representative images of control and lesioned whisker pad (left), *en face* imaging of L4 somatosensory cortex (middle) and heat map of VGLUT2 intensity (right). (Scale bar = 100 μm). **c**) Quantification of barrel distinctness based on VGLUT2 intensity in barrels vs. septa in control and deprived hemispheres. Box and whisker plots show range (whiskers), median, and first and third quartiles (box). (2-4 barrel/septa pairs per condition per mouse; P5: n=3 mice, P7: n=4 mice, 2-way ANOVA with Sidak post-hoc test). **d**) Average barrel field VGLUT2 intensity in deprived and spared hemispheres. (P5: n=3 mice, P7: n=4, 2-way RM ANOVA with Sidak post-hoc test). **e**) Schematic of single cell barcoding and RNA sequencing using the 10x Chromium system. **f**) UMAP plot of non-neuronal single cell sequencing in P7 barrel cortex labelled by cell type

assigned by representative marker analysis. **g-h**) Data in F plotted as control vs. whisker deprived hemisphere (**g**) and unsupervised clustering (**h**). **i**) Percent of each cluster in control (blue) vs. deprived (red) hemispheres. (Chi-square test, * $p<0.01$, $f > 0.15$). **j**) Differentially expressed genes between astrocyte cluster 1 (deprived-enriched) and astrocyte cluster 5 (control-enriched.) (Thresholds: fold change > 30%, adj. $p < 0.001$). **k**) Representative image of quantitative in situ hybridization for *Htra1* mRNA co-stained with Aldh1L1-GFP astrocyte reporter. Inset highlights a single astrocyte. (Scale bar = 10 μm) **l**) *Htra1* mRNA puncta per astrocyte in control and deprived hemispheres. (n= 65 astrocytes (control) and 82 astrocytes (deprived) from 3 mice, Welch's t-test). *Statistics: All tests shown are two-tailed. *p<0.05, **p<0.01, ***p<0.001, ****p<0.0001 unless otherwise noted. Graphs shown as mean ± SD.* ***See also Figures S4.1.1-S4.1.3, Table 4.1***

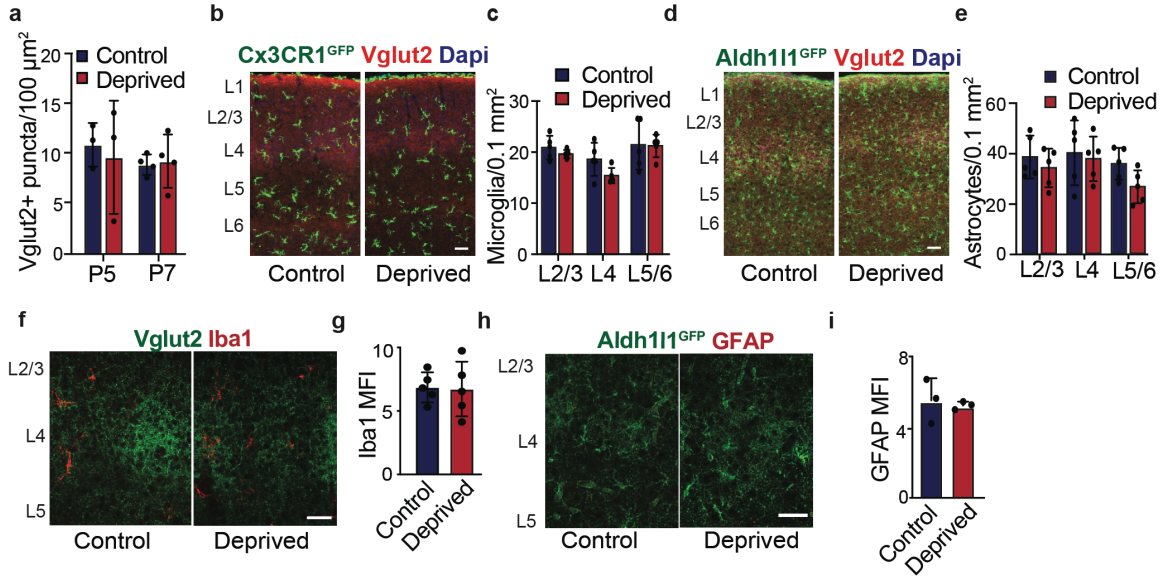

Supplemental Figure 4.1.1: Synapse numbers, glial numbers and glial reactivity are unchanged after partial whisker deprivation.
a) Data in Fig. 4.1D represented as # of VGLUT2+ puncta in barrel cortex after whisker deprivation. (P5: n=3, P7: n=4). **b**) Representative image of microglia (Cx3cr1-GFP+) in P7 cortex (Scale bar = 20 μm) **c**) Microglial density across cortical layers (n = 4 mice). **d**) Representative images of astrocytes (Aldh1l1-GFP+) in P7 cortex. (Scale bar = 20 μm) **e**) Astrocyte density across cortical layers. (n = 5 mice). **f-g**) Representative images and quantification of Iba1 intensity in coronal sections through the barrel cortex at P7. (Scale bar = 25 μm; n = 28 images from 5 mice). **h-i)** Representative images and quantification of with GFAP intensity in Aldh1l1-eGFP+ astrocytes in coronal sections through the mouse barrel cortex. (Scale bar = 25 μm; n = 3 mice). *All error bars show mean ± SD.*

Table 4.1: Sample sizes and cell yields from the single cell sequencing in Fig. 6.1 and 6.2,4.

Sample age	Sample description	#cells after QC
Pan glial RNAseq (isolated by cold protease digestion), Figure 1		
P7	1 Female, control and deprived hemispheres	394 control, 535 deprived
P7	1 Male, control and deprived hemispheres	276 control , 456 deprived
Microglial only RNAseq (isolated by dounce homogenization), Figures 2, 4		
P5	3 Females, pooled, control and deprived hemispheres	1360 control , 1265 deprived
P5	3 Male, pooled, control and deprived hemispheres	1595 control , 1290 deprived
P7	3, Females pooled, control and deprived hemispheres	2929 control, 2224 deprived
P7	1 Male, control and deprived hemispheres	1165 control , 502 deprived

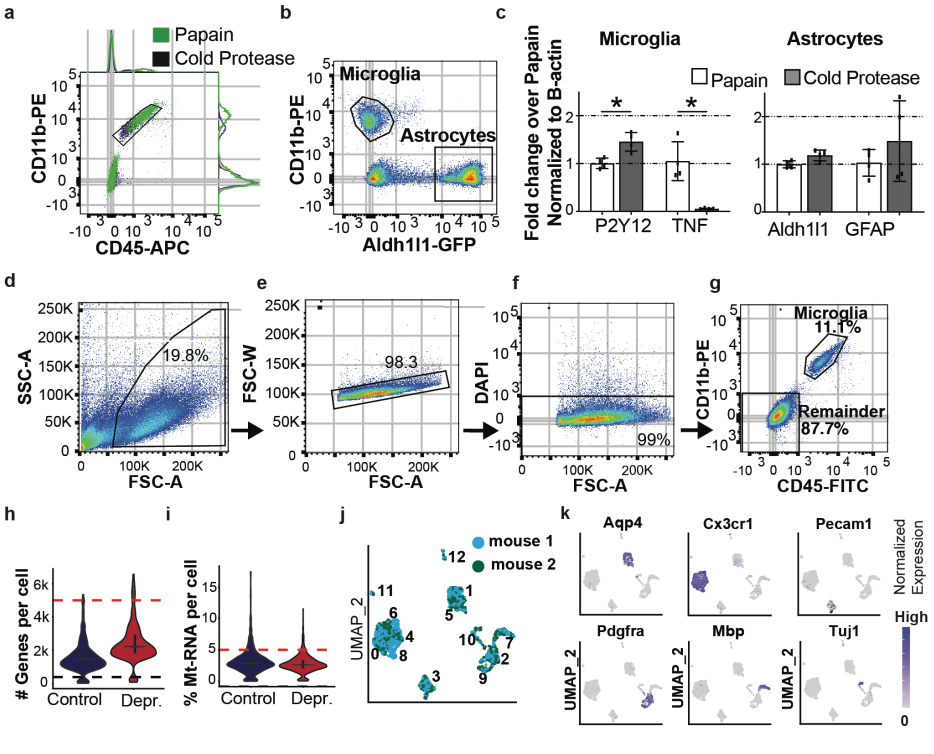

Supplemental Figure 4.1.2: Optimization of cold-protease digestion strategy and quality control of scRNAseq data in Figure 4.1. **a**) Flow gates showing reduced microglial CD45 and CD11b after cold protease digestion at 4ºC relative to papain digestion at 34ºC. **b**) Gating strategy for astrocyte and microglia isolation by Fluorescence Activated Cell Sorting (FACS). **c**) qPCR for homeostatic (P2ry12, Aldh1l1) and reactivity markers (TNF, GFAP) in microglia and astrocytes after enzymatic dissociation at 34º C (Papain) or 4º C (Cold Proteases) (n=4 mice, Welch's ANOVA with Dunnett's T3 post-hoc test). **d-g**) Full gating strategy for single cell sequencing. Gating in **g** used to enrich microglia to 30% of total cells. **h-i**) Quality control metrics for scRNAseq: number of genes recovered (**h**) and mitochondrial RNA content per cell by sample (**i**). Lines show thresholds used for cell selection. Median and 1st and 3rd quartiles shown in black on each violin. **j**) UMAP plot colored by biological replicate shows consistency across replicates. **k**) Representative feature plots showing genes used for cell type classification, including *Cx3cr1* (Microglia), *Aqp4* (Astrocytes), *Pecam1* (Endothelial cells, CD31), *Pdgfra* (OPCs), *Mbp* (Oligodendrocytes), and *Tubb3* (Neurons, TUJ1). *Statistics: All tests shown are two-tailed. *p<0.05, **p<0.01, ***p<0.001, ****p<0.0001 unless otherwise noted. Graphs shown as mean ± SD.*

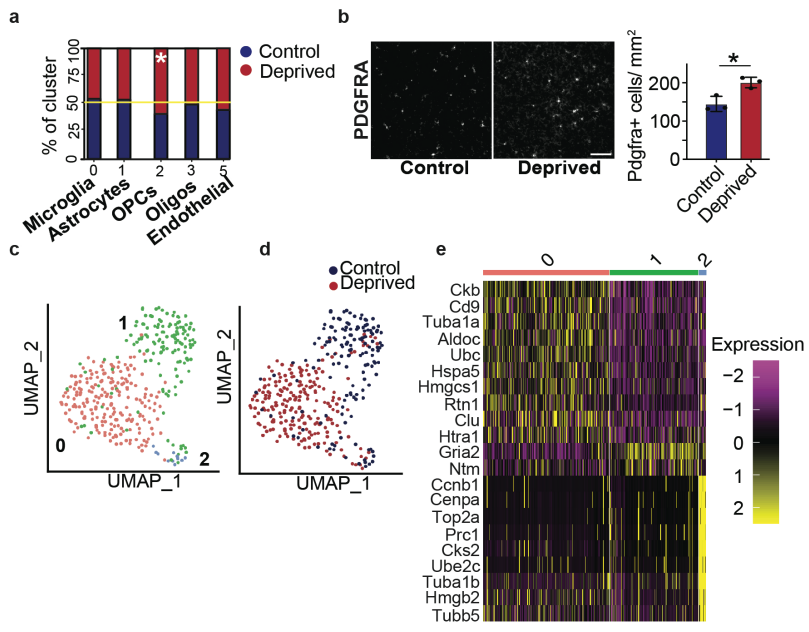

Supplemental Figure 4.1.3: Additional analyses of oligodendrocyte progenitor cells and astrocytes in barrel cortex after whisker deprivation. **a**) Data from Fig. 1F-H shown as a bar plot of relative proportions of control and deprived cells collapsed by cell type. (Chi-square test, *p<0.01). **b**) Representative images and quantification of PDGFRα+ oligodendrocyte progenitor cells in L4 of the barrel cortex. (n=3 mice, paired t-test; scale bar = 50 μm). **c-d**) UMAP plot showing astrocyte-only reclustering colored by cluster (**c**) and condition (**d**) (n=357 cells, resolution = 0.6). **e**) Heatmap of top nine genes enriched in each astrocyte cluster ordered by natural log fold change. *Htra1*, in the top 25 genes, is also included. (MAST DE test, $P_{Adj.} < 0.001$). *Statistics: All tests shown are two-tailed. *p<0.05, **p<0.01, ***p<0.001, ****p<0.0001 unless otherwise noted. Graphs shown as mean ± SD.*

A type I interferon-responsive microglial subset expands 20-fold during cortical remapping

Microglia have multiple developmental functions that may be relevant to barrel maturation. They engulf synapses in some developmental and disease contexts (Hong et al., 2016; Schafer et al., 2012), promote synapse formation, maturation, and plasticity (Hoshiko et al., 2012; Miyamoto et al., 2016; Nguyen et al., 2020), and engulf dead or dying cells (Boada-romero et al., 2020; Fourgeaud et al., 2016b; Krasemann et al., 2017; Sierra et al., 2010). Neuronal cell death in this region peaks at P5-P6 and ongoing synaptic and dendritic formation and remodeling occurs throughout the first postnatal week and beyond (Blanquie et al., 2017; Erzurumlu and Gaspar, 2012). To molecularly define this microglial response with additional temporal resolution, we performed single cell RNA sequencing of microglia at P5 and P7 after induction of topographic remapping via whisker removal at P2. We purified microglia using mechanical dissociation followed by magnetic bead isolation, which is ideal for preserving *in vivo* microglia signatures, although it depletes other glial subsets (**Fig. 4.2a**, **Table 4.1**, (Bohlen et al., 2019; Chris Bennett et al., 2018; Haimon et al., 2018; Marek et al., 2008; Miltenyi et al., 1990)). We recovered 12,330 cells from 10 mice after quality control and identified 10 microglial clusters. Two pairs of closely related clusters, 0/5 and 6/7, were combined with their nearest neighbors due to low numbers of uniquely enriched genes; of the resulting eight clusters, four were altered by whisker deprivation (**Fig. 4.2b-e,** quality control in **Fig. S4.2.4a-f**). Cell cycle analysis showed that clusters 1, 2, and 6/7 clustered mainly by markers of the different stages of cell division and were more abundant at P7 than P5 (**Fig. S4.2.4g-j**). A small macrophage subset (1% of cells, cluster 9; *Pf4*, *Lyve1*) was not substantially changed by whisker deprivation.

We focused on the four non-proliferative clusters of microglia (0/5,3,4,8), which changed in relative abundance after cortical remodeling. Cluster 0/5, the largest subset, expressed

homeostatic markers (*P2ry12, Ccr5*) and decreased modestly after whisker deprivation. The cluster most closely related to cluster 0/5 was cluster 4, which in turn was the most similar to 'proliferative-region associated microglia' (PAMs, 38/42 genes upregulated; (Hammond et al., 2019; Li et al., 2019a)) and was the only cluster to exhibit similarity with 'damage-associated microglia' (DAMS) identified in previous studies (Keren-Shaul et al., 2017) (36/83 genes upregulated; **Fig. S4.2.4k-l**). Cluster 4 also decreased modestly after whisker deprivation. In contrast, cluster 3 was enriched in canonical neuronal genes (*Rbfox3, Grin1)* and modestly increased after whisker deprivation (**Fig. 4.2c-d**).

The most striking difference between control and whisker-deprived conditions was the emergence of a microglial subpopulation enriched in type I interferon (IFN-I) response genes (cluster 8). The IFN-I response is a highly evolutionarily conserved antiviral response, but its functions in the developing brain are unknown (McNab et al., 2015). Differential gene expression and Gene Ontology (GO) analysis on cluster 8 revealed a robust interferon response signature (*Ifitm3*, *Mx1*, *Ifit3, Isg15*, *Irf7,* and *Stat1)* and GO terms "Response to virus" (GO:0009615), "Response to interferon-alpha" (GO:0035455), and "Response to interferon-beta" (GO:0035458) (**Fig. 4.2f-g)**. The interferon-responsive cluster 8 was enriched 20-fold in P5 deprived vs. control cortices (0.5% in control vs 11% in deprived) but was indistinguishable from control by P7 (0.6% vs 0.4%) (**Fig. 4.2h-i, Fig. S4.2.4m-p**). This cluster was located between microglia and macrophages in UMAP space but showed microglia-like expression of *Tmem119*, *Tgfbr1*, and *Hexb* (**Fig. S4.2.4q**). We observed little to no overlap between this IFN-I responsive cluster and the genes previously described in 'damage-associated microglia' (DAMS, **Fig. S4.2.4k;** (Keren-Shaul et al., 2017)). These data reveal a microglial subset that is rare in the typically developing cortex but expands markedly during a restricted phase of topographic remapping.

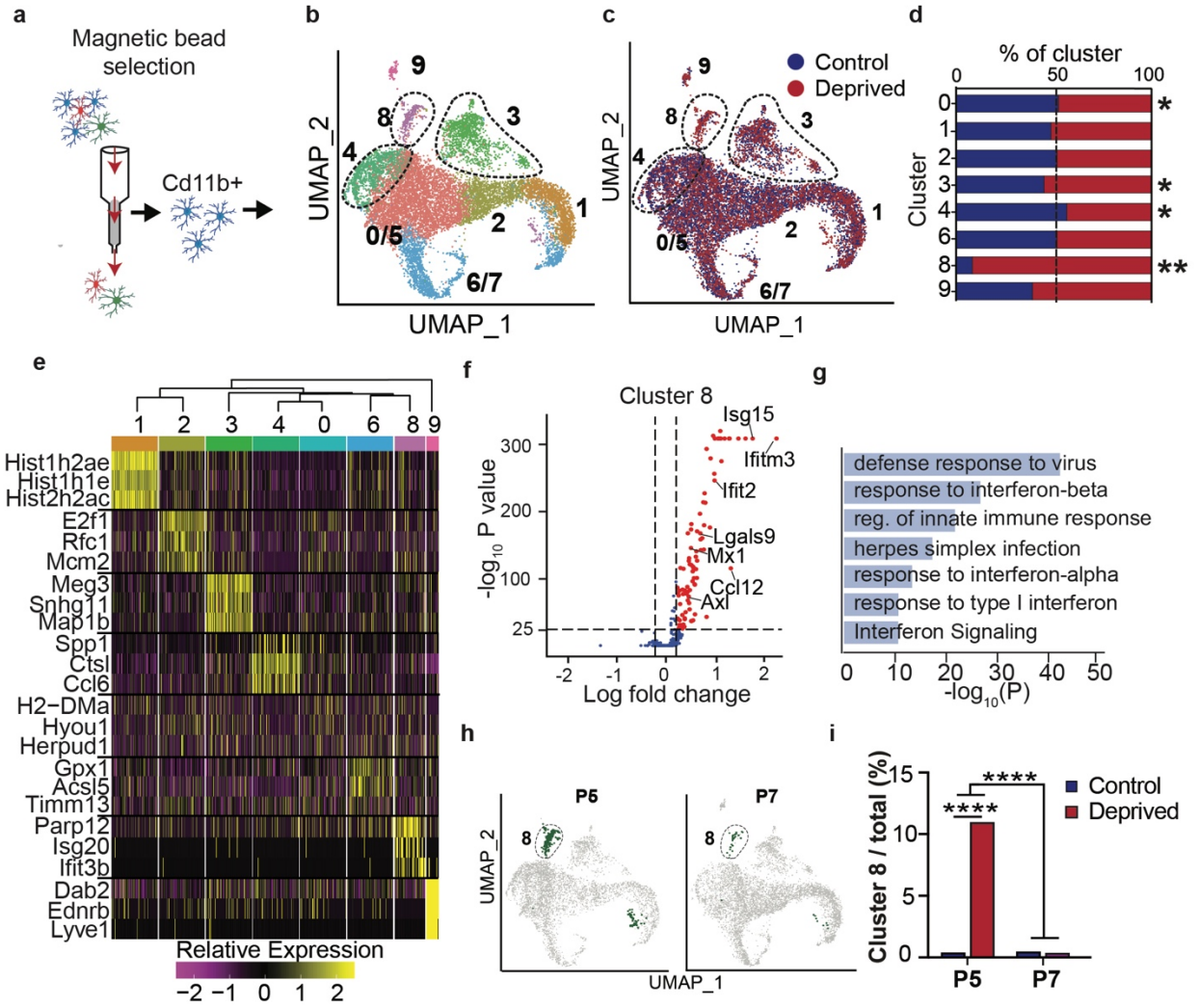

Figure 4.2. A type I interferon-responsive microglial subset expands 20-fold during cortical remapping.

a) Schematic of MACS-isolation of microglia for single cell sequencing. **b**) UMAP plot showing independent clustering of 12,000 CD11b+ cells, pooling P5 and P7 timepoints from control and whisker deprived cortices, including microglia (Clusters 0- 8) and macrophages (Cluster 9). Dotted lines highlight clusters for further analysis. Clusters 0/5 and 6/7 were the results of merging nearest neighbor clusters 0 and 5 as well as 6 and 7 due to low numbers of uniquely expressed genes. **c**) Clusters colored by condition (control vs. whisker deprived). **d**) Quantification of cluster composition by condition. X-axis represents percent of cells in each cluster from the control (blue) or deprived (red) hemispheres, normalized for total number of cells per sample. (Chi-square test with Bonferroni correction, * p_{Adj} <0.01, ** $p_{Adj} < 10^{-25}$). **e)** Heatmap of top differentially expressed genes (log_2 fold change, $p_{Adj} < 10^{-25}$). **f**) Volcano plot of genes differentially expressed in cluster 8 relative to all other clusters. **g**) Cluster 8 upregulated GO terms. **h**) Clusters separated by age (P5 vs. P7) with cluster 8 highlighted (green). **i**) Plot of cluster 8 abundance at each time point in control vs. deprived conditions (Chi-square test with Bonferroni correction, **** $p_{Adj} <10^{-10}$). ***See also Figure S4.2.4.***

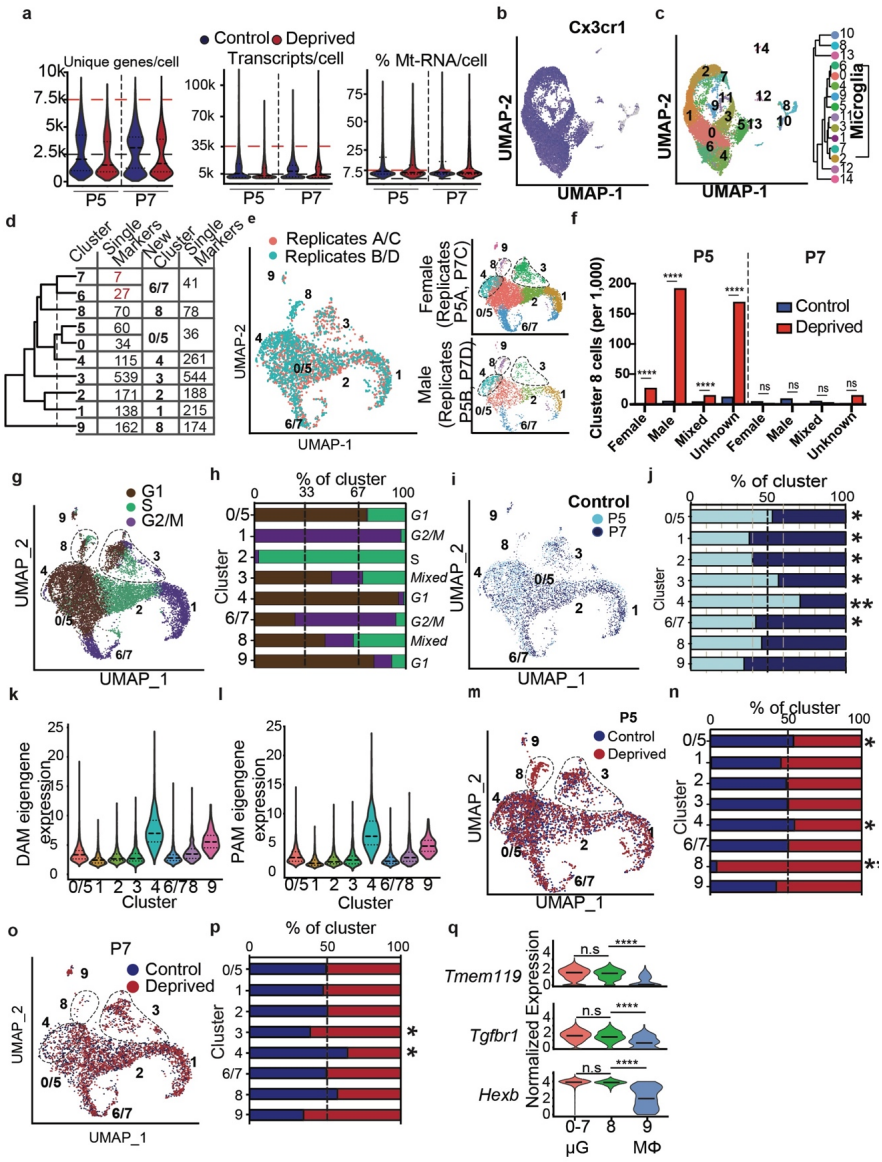

Supplemental Figure 4.2.4: Quality control and additional analyses of microglial single cell sequencing data in Figures 4.2-4.4.

a) Quality control metrics for microglial single cell sequencing (% Mt-RNA/cell: mitochondrial RNA content). Dotted lines indicate minimum and maximum threshold settings. Dashed lines represent median, 1st and 3rd quartiles. **b-c**) Feature plot of *Cx3cr1* and unsupervised clustering of all thresholded cells used to select myeloid cells (*Cx3cr1*+) for subsequent analysis. **d)** Table showing the number of uniquely upregulated genes (lfc >0.15, p.adj < 10^{-5}) before and after combining clusters 6/7 and 0/5. The dotted line shows the threshold below which clusters were combined due to few unique DEGs in both lower branches. The resultant clusters were not closely related to any other clusters with few unique DEGs. **e)** Comparison of biological replicates bioinformatically segregated via expression of male-specific genes *Ddx3y* and *Eif2s3y* and female-specific genes *Xist* and *Tsix*, normalized for abundance. Female and Male replicates also shown colored by cluster in UMAP space. (Replicate A: 3 female mice at P5; Replicate B: 3 male mice at P5; Replicate C: 3 female mice at P7; Replicate D: 1 male mouse at P7). **f)** Cluster 8 enrichment in definitively female (*Xist/Tsix*+; *Ddx3y/Eif2s3y*-), definitively male (*Ddx3y/Eif2s3y*+; *Xist/Tsix*-), mixed (*Xist/Tsix*+;*Ddx3y/Eif2s3y*-) and unknown(*Xist/Tsix*-;*Ddx3y/Eif2s3y*-) cells. **g**) UMAP plot showing cell cycle phase assignment determined using annotation from (Kowalczyk et al., 2015). **h**) Quantification of cluster composition by cell cycle phase. X-axis=% cells per cluster in G1, S, or G2/M. Labels to the right indicate that cluster's predominant phase. **i-j**) Age comparison by feature plot (i) and quantification (j) , showing only control cells, normalized for abundance. (Chi-square test with Bonferroni correction, *adj. p<0.01, **adj. p < 10^{-25}). **k)** DAM Eigengene signature expression by cluster. The eigengene represents the 83 genes upregulated by DAMS that were also found in this dataset (lfc > 1.5, adj. p < 10^{-8}) (Keren-Shaul et al., 2017). Dotted lines represent median and 1st and 3rd quartiles. **l**) PAM Eigengene signature expression by cluster. The eigengene represents the 42 genes conserved between two published datasets of a developmental PAM signature that were also expressed in this dataset. (lfc > 1.5, adj. p < 10^{-8}) (Hammond et al., 2019; Li et al., 2019a). Dotted lines represent median and 1st and 3rd quartiles. **m-p**) UMAP feature plots and quantification of percent composition of each cluster at P5 (**m-n**) and P7 (**o-p**). (Chi-Square test with Bonferroni correction, *adj. p<0.01, **adj. p < 10^{-25}). **q)** Canonical microglial genes across microglial clusters 0-6 (pooled), microglial cluster 8, and macrophage cluster 9. Line = median. (MAST DE test, ****p<10^{-25}).

The transmembrane protein IFITM3 defines a phagocytic microglial subset enriched during cortical remapping

To further determine whether interferon-responsive microglia represented a *bona fide* microglial subtype *in vivo*, we examined markers that could be used for immunostaining in tissue sections. *Ifitm3* was the most highly upregulated gene in interferon-responsive cluster 8 (**Fig. 4.2f, Fig. 4.3a**). This IFN-α/β-stimulated gene encodes a transmembrane protein known to limit viral replication, cancer progression, and amyloid beta plaque deposition (Bailey et al., 2014; Brass et al., 2009; Hur et al., 2020; Lee et al., 2020). We identified a rare population of IFITM3+ microglia in layers 4 and 5 of developing barrel cortex that were increased up to 8-fold during topographic remapping, as quantified *in situ* and by flow cytometry **(Fig. 4.3b-c; Fig. S4.3.5a-d).** We confirmed that IFITM3+ cells expressed *Mx1*, the canonical interferon stimulated transcription factor also enriched in cluster 8, as assessed by flow cytometry using an $Mx1^{GFP}$ reporter (Uccellini and García-Sastre, 2018) (**Fig. S4.3.5e-f**). An alternate marker, BST2 (a.k.a. Tetherin (Liberatore and Bieniasz, 2011)) was also increased after whisker deprivation and was expressed in most IFITM3+ cells, where it localized to an intracellular compartment (**Fig. S4.3.5g-i**). Consistent with its less specific expression in cluster 8 by single cell sequencing (**Fig. S4.3.5j**), a portion of BST2+ cells did not co-express IFITM3. Based on its similarities in developmental abundance, induction with barrel remodeling, location near barrels, and high concordance with two other markers that define our single cell cluster, we conclude that IFITM3 is a sensitive and specific marker that can identify the interferon-responsive cluster 8 *in situ*.

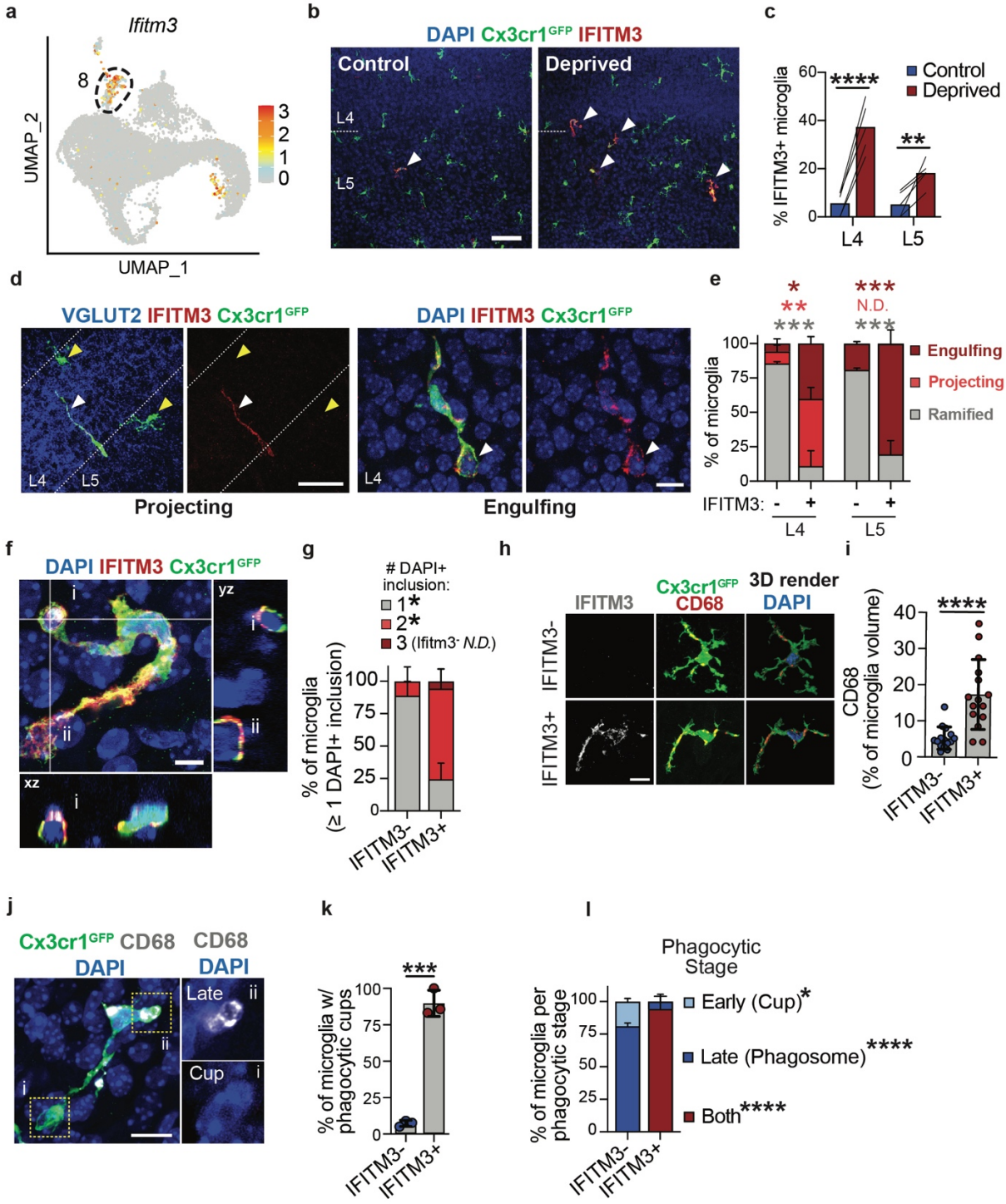

Figure 4.3. The transmembrane protein IFITM3 defines a phagocytic microglial subset enriched during cortical remapping.

a) UMAP feature plot showing normalized expression of cluster 8 marker gene *Ifitm3*. **b**) Representative image of IFITM3+ microglia (arrowheads) in control or whisker-deprived somatosensory cortex at P5 (Scale = 50 µm). **c**) Percent IFITM3+ microglia in coronal sections from layers 4 and 5 (L4, L5). Lines connect control and deprived from the same mouse (n=5, 2-way RM ANOVA with Sidak post-hoc test). **d**) Representative image of 'projecting' and 'engulfing' IFITM3+ microglia in P5 deprived cortex (Coronal sections, scale = 20 µm (left), 5 µm, (right)). **e**) Quantification of microglial morphological subtypes described in **e** (n = 4 mice, 2-way RM ANOVA with Sidak post-

hoc test). **f**) Confocal image and orthogonal views of an IFITM3+ microglia containing multiple phagocytic cups (i, ii show nuclei-containing phagocytic cups that are distinct from the microglia nucleus). (Scale bar = 5 μm) **g**) Number of DAPI+ phagocytic compartments (inclusions) per microglia, among microglia with at least one DAPI+ phagocytic compartment (n = 4 mice, 2-way RM ANOVA with Sidak post-hoc test). **h**) Representative images and 3D-rendering of CD68+ lysosomes within IFITM3+ and IFITM3- microglia in L4. (Scale = 10 μm) **i**) Quantification of % CD68 volume of total microglial volume in IFITM3+ and IFITM3- microglia (13 IFITM3- and 15 IFITM3+ from n= 3 mice, Mann-Whitney test). **J**) Representative image of a Cx3cr1-GFP+ microglia highlighting a phagocytic cup (i; $CD68^-$, non-pyknotic DAPI signal, incomplete DAPI envelopment by microglial processes) and a late phagosome or phagolysosome (ii; $CD68^+$, pyknotic DAPI signal, complete envelopment by microglial processes). (Scale bar = 10 μm). **k**) Percent of IFITM3- and IFITM3+ microglia containing phagocytic cups. (n = 3 mice, Welch's t-test). **L**) Distribution of early phagocytic cups and late phagosomes as a proportion, in microglia containing at least one phagosome. (n = 7-10 cells each from 3 mice/group, 2-way RM ANOVA with Sidak post-hoc test). *Statistics: All tests shown are two-tailed. *p<0.05, **p<0.01, ***p<0.001, ****p<0.0001. Graphs shown as mean ± SD (bar graphs) or mean ± SEM (stacked bar graphs).* ***See also Figure S4.3.5.***

While IFITM3- microglia were predominantly ramified, IFITM3+ microglia were morphologically distinct with two main subtypes. A subtype exclusive to layer 4 extended a singular primary process into the barrel hollow ('projecting'), whereas others contained prominent IFITM3+ phagocytic cups enveloping DAPI+ nuclei (**Fig. 4.3d-e**). Phagocytic IFITM3+ microglia often contained multiple DAPI+ inclusions, which appeared only rarely in IFITM3- microglia (**Fig. 4.3f-g**). Furthermore, IFITM3+ cells had higher levels of the lysosomal marker CD68, consistent with increased phagolysosomal activity (Chistiakov et al., 2017) (**Fig. 4.3h-i**).

Phagocytosis proceeds in stages which include enveloping of extracellular material by the phagocytic cup, packaging into a phagosome, fusion to mature lysosomes to form a phagolysosome, and resolution of the phagolysosome by fragmentation(Lancaster et al., 2021; Uribe-Querol and Rosales, 2020). Our data suggested that multiple stages of phagocytosis might be regulated by the interferon stimulated genes expressed in cluster 8. IFITM3+ cells were more likely to contain phagocytic cups than IFITM3- microglia (90% vs. 7%; **Fig. 4.3j-k**) but were also more likely to contain both early and late stages of phagocytosis in the same cell (**Fig. 4.3l).** While IFITM3 was enriched around phagocytic cups and diminished with closure of the phagocytic cup and upregulation of CD68+ (**Fig. S4.3.5k-l**), BST2 was enriched in a perinuclear compartment (**Fig. S4.3.5g**). Whisker deprivation led to a significant increase in the number of microglia with

phagocytic cups, phagolysosomes, or both (**Fig. S4.3.5m-n**). Taken together, these data suggest that IFN-I broadly amplifies the microglial phagocytic response, and that IFN-I responsive microglia are enveloping whole cells and often multiple cells simultaneously.

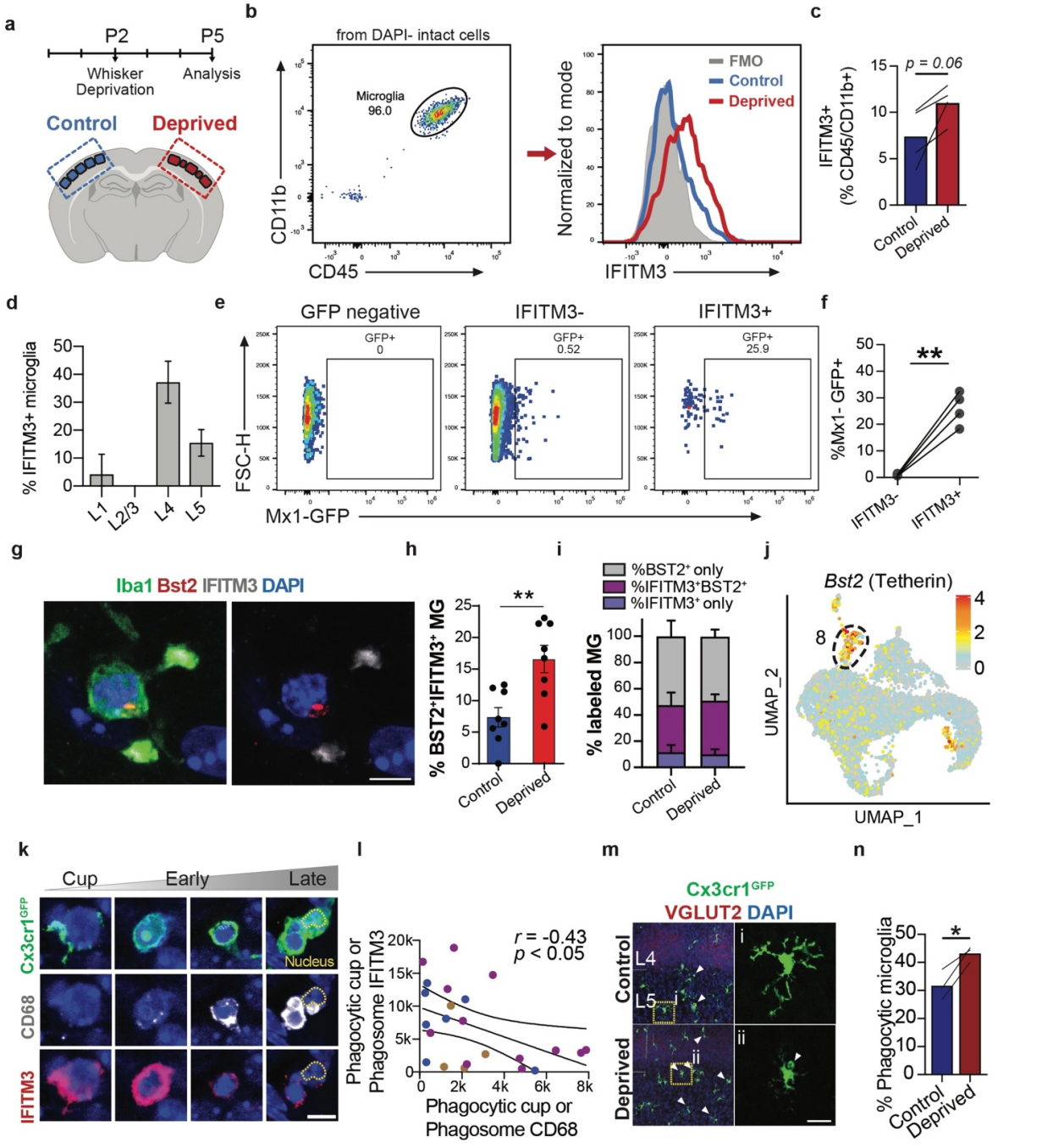

Supplemental Figure 4.3.5: Validation and additional analyses of IFITM3 expression after whisker deprivation.

a) Experimental design for IFITM3 *in situ* validation experiments. **b-c**) Representative gating strategy, histogram, and quantification of IFITM3 surface protein expression in $Cd11b^{+}/CD45^{low}$ microglia in control and deprived

hemispheres (FMO: fluorescence minus one negative control). (Lines represent control and deprived hemispheres from individual mice, paired t-test). **d**) Percent IFITM3+ microglia stratified by cortical layers in deprived cortex, see **Fig. 4.3d** for representative images (n = 3 mice). **f**) Representative flow cytometric gating strategy of Mx1-GFP+ microglia from IFITM3$^-$ vs. IFITM3$^+$ populations. (Lines connect values from the same mouse, paired t-test). **g**) Image showing colocalization of BST2 (Red) with Iba1 (green, microglia, outlined with white dotted line) and IFITM3 (white) in the deprived barrel cortex. (Scale bar = 10 μm). **h)** Quantification of double-positive BST2+/IFITM3+ microglia as a percentage of total microglia. (n = 2-3 images per condition from 3 mice, Welch's t-test). **I)** Percent of Iba1+ microglia expressing IFITM3 only (blue), BST2 only (grey) or both (purple). (n=3 mice). **j)** Normalized expression of *Bst2* in microglia sequenced in Fig. 2. **k)** Representative images showing IFITM3 and CD68 protein levels in different phagocytic compartments (Yellow dotted line = microglial nucleus, Scale bar = 5 μm). **l)** Correlation of CD68 and IFITM3 MFI per phagocytic compartment (n = 23 cells from 3 mice, r = Spearman correlation coefficient). **m)** Representative images of microglia in control and deprived cortex, inset: single microglia (scale = 50 μm, arrowheads= phagocytic compartments). **n)** Percent microglia containing at least one phagosome or phagocytic cup in control vs. deprived cortices (P5, n = 3, paired t-test). *Statistics: All tests shown are two-tailed. *p<0.05, **p<0.01, ***p<0.001, ****p<0.0001 unless otherwise noted. Graphs shown as mean ± SD.*

Type I Interferon responsive microglia are poised for neuronal engulfment

Our data suggest that IFN-I responsive microglia are actively engulfing DAPI+ cells. However, the cluster itself was not enriched for traditional phagocytic genes. This prompted us to further examine the dynamic lineage relationships between interferon-responsive cluster 8 and its neighbors. We performed RNA velocity analysis, which uses the ratio of unspliced pre-mRNA to spliced mRNA to infer trajectories between neighboring clusters on the time scale of hours, with higher velocities predicting a faster transition between cell states (Bergen et al., 2020). Interferon-responsive cluster 8 showed a predicted trajectory towards cluster 3 (**Fig. 4.4a-b**). Of note, clusters 3 and 8 were both distinct from the predominant cluster linked to lysosomal function, cluster 4 (*Cd68, Trem2, Apoe*; GO:0005764, "lysosome"; **Fig. S4.4.6a-b**). From this analysis, we hypothesized that the IFN-I responsive cluster 8 might be functionally linked to cluster 3.

Differential gene expression for cluster 3 showed an enrichment in neuronal mRNAs (*Rbfox3, Grin1, Gria1*) (**Fig. 4.4c-d**), and less commonly other cell type-specific mRNAs, including oligodendrocytes *(Vcan*) and astrocytes (*Sparcl1*; **Fig. S4.4.6c**) without downregulation of microglial genes. This finding was not due to an outlier effect, as most cells in cluster 3

expressed more neuronal mRNAs than 95% of all other cells (**Fig. 4.4e**). Non-microglial mRNA could indicate an atypical gene expression profile or captured foreign material. Although we cannot rule out the former possibility, we concluded that it was unlikely for two reasons. First, the promoters for these genes were less likely to be accessible than promoters of known microglial genes, including cluster 4 markers, based on an ATAC-Seq dataset of cortical microglia **(Fig. S4.4.6d-e,** (Han et al., 2021)). Secondly, these non-microglial genes in cluster 3 were enriched for intronic sequences associated with unspliced transcripts relative to known microglial genes (**Fig. S4.4.6f-g**). These data suggest that the neuronal mRNA was derived from captured nuclei.

We next investigated whether a candidate post-engulfment microglial subset was present *in situ*. *In situ* hybridization for *Rbfox1* and *Grin1*, two of the most abundant transcripts in cluster 3, revealed microglia forming phagocytic cups around neuronal soma (**Fig. 4.4f-g**). Definitive neuron-engulfing phagocytic cups constituted 80% of these engulfing microglia at P5, and 20% at P7, suggesting that when the IFN-I responsive subset is abundant, most engulfed cells were neurons. Once the phagocytic cup closed, these transcripts were undetectable (**Fig. 4.4f**), as was expression of marker proteins such as NeuN (not shown). We therefore examined microglial engulfment in cell-type specific TdTomato (TdT) reporter lines (*Ai14;* Jax 007908), given this marker's relative stability in the lysosome. In a *Rorb^{cre};R26R-TdT* line labeling most excitatory L4 neurons and some neurons in L5/6, but not dendrites from other layers ((Harris et al., 2014); Jax **023526**), we observed that 9% of L4/5 microglia at P5 had TdT-positive CD68-containing phagolysosomes, suggesting that they had recently engulfed a neuronal soma (**Fig. 4.4h**, **j**). In contrast, we observed no TdT inside microglia in an astrocyte reporter line at this age (*Aldh1l1^{TdT}*; **Fig. 4.4i-j**). These data suggest that microglia in the barrel cortex engulf neurons *in vivo*.

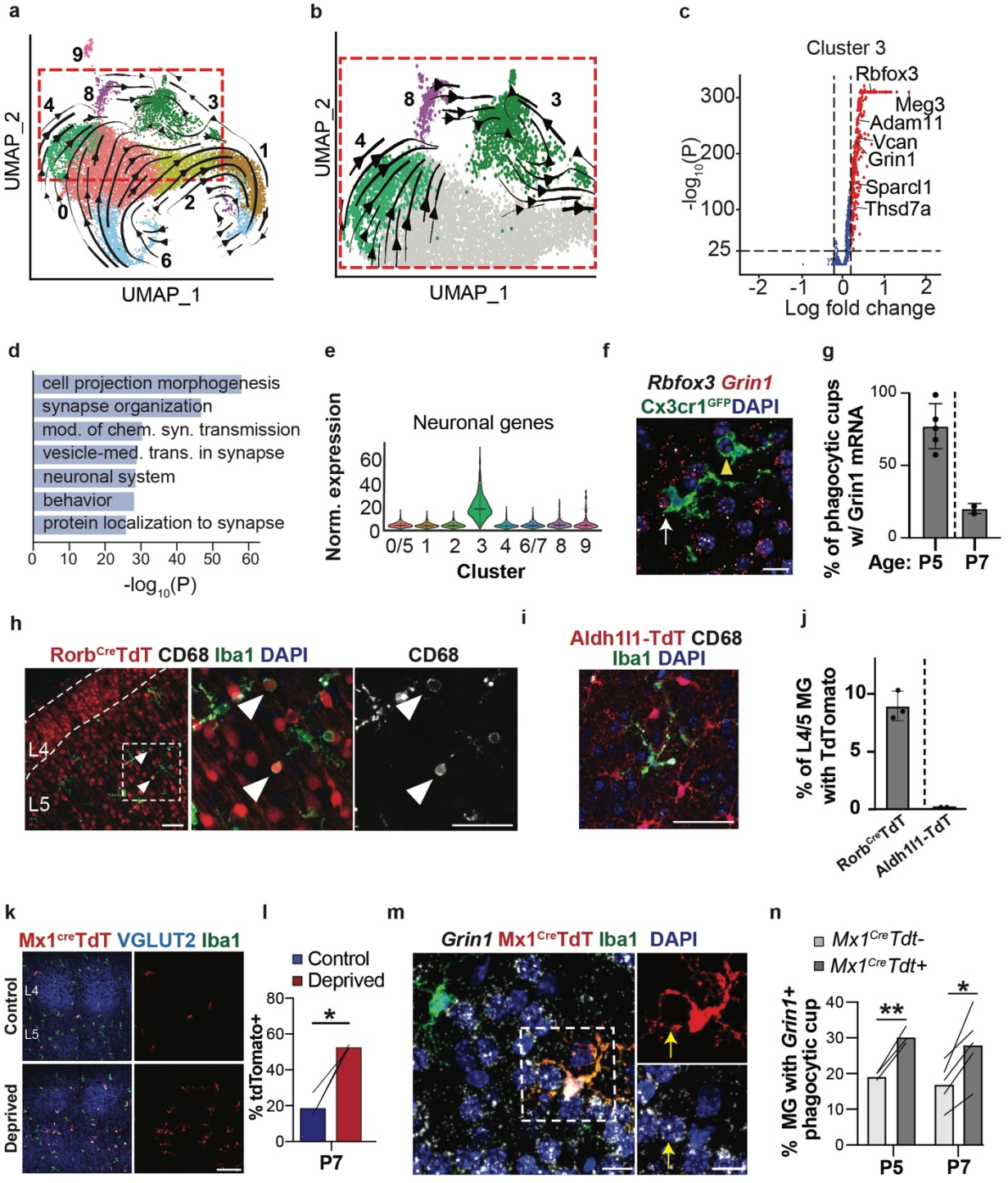

Figure 4.4. Type I Interferon-responsive microglia are poised for neuronal engulfment.
a-b) RNA velocity analysis colored by cluster (scVelo, (Bergen et al., 2020)); Inset highlights clusters 3, 4, and 8. **c-d**) Differentially expressed genes and upregulated GO terms for Cluster 6. **e)** Normalized expression of a neuronal eigengene across clusters numbered as in 2b. The 45 differentially expressed genes in cluster 3 (natural log fold change > 0.25, adj. p < 1e-10) that were neuron-specific (per (Zhang et al., 2014)) were used to define the eigengene. Lines show 5th, 50th, and 95th percentiles.**) f)** Representative image of neuronal mRNA transcripts *Rbfox3* and *Grin1* in tissues from a Cx3cr1^{GFP} reporter line. White arrow: a microglial phagocytic cup. Yellow arrowhead: enclosed phagosome lacking neuronal transcripts. (scale bar = 10 μm). **g)** Quantifications of percent of phagocytic cups enveloping nuclei

with *Grin1* transcripts at the specified ages. (Dots=mice). **h)** Representative image of Iba1+ microglia engulfing *RorbCre;Ai14+* neurons in barrel cortex. Inset: layer 5. Arrowheads: Rorb^{cre}TdT positive and CD68+ phagolysosomes. (Scale bar =50 μm). **i**) Representative image of Iba1+ microglia and Aldh11L1-TdT+ astrocytes in barrel cortex. (scale bar = 50 μm). **j)** Quantification of percent microglia containing TdTomato signal in Rorb^{cre}:TdT or Aldh111^{TdT} transgenic mice (dots=mice). **k**) Representative images of TdTomato+ cells (*Mx1-Cre;Rosa26-LSL-TdT*) in layers 4-5 of barrel cortex co-labeled with microglial marker Iba1 and VGLUT2 to highlight barrels. (Scale bar= 100 μm) **l**) TdTomato+ microglia in control and deprived cortices. (n = 3 mice, paired t-test). **m)** Representative image of a Mx1^{cre}TdT + microglial phagocytic cup around a *Grin1*+ nucleus (inset, arrow). (Scale bar =10 μm). **n**) Quantification of percent Mx1^{cre}TdT + or negative microglia forming phagocytic cups around *Grin1*+ nuclei. (Scale bar = 10 μm). (n=3 mice at P5 and 5 mice at P7, 2-way RM ANOVA with Sidak post-hoc test). *Statistics:* Thresholds in **a, b, c, d** are $p_{adj} < 10^{-25}$ >, natural log fold change > 0.2. *All tests shown are two-tailed. *p<0.05, **p<0.01, ***p<0.001, ****p<0.0001 unless otherwise noted. Graphs shown as mean ± SD.* ***See also Figure S4.4.6.***

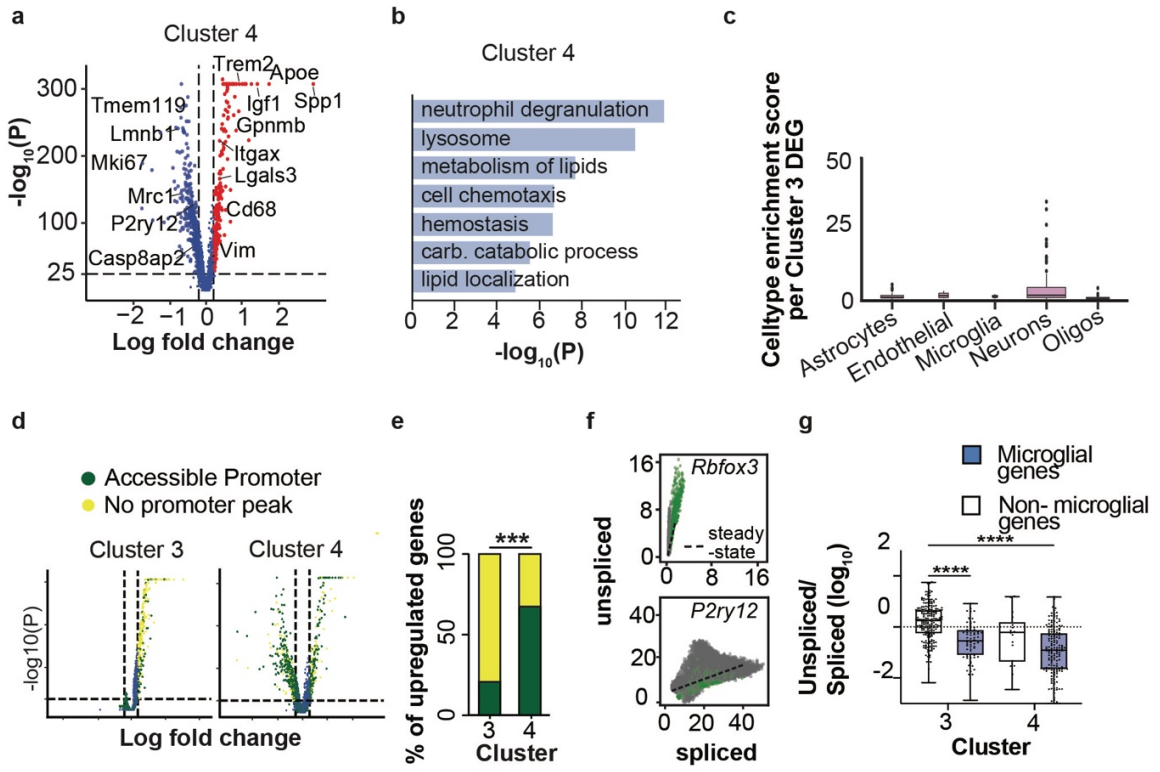

Supplemental Figure 4.4.6: Additional analysis of putative neuron-digesting cluster 6.
a-b) Volcano plot and gene ontology analysis of DEGs in cluster 4, which is analyzed in subsequent panels in comparison to cluster 6. **c)** Rank plot of genes enriched in cluster 3 (natural log fold change > 0.25, adj. $p < 10^{-10}$) that are canonical for specified cell type expressed as fold- enrichment relative to next ranked cell type. Canonical gene expression values derived from a published bulk-sequencing dataset (Zhang et al., 2014). **d**) Volcano plots in Fig. 4.4**c** (cluster 3) and S4.6**b** (cluster 4) colored by genes with accessible promoters (green) vs. no promoter peak (gray) from ATAC-seq data from P30 somatosensory cortex microglia (Han et al., 2021). "Accessible promoter" defined as ATAC-seq reads > 10th percentile of all peaks, "no promoter peak" defined as reads below 10% threshold. **e**) Bar plot of differentially expressed genes with accessible promoters vs. no promoter peak in clusters 3 and 4 (Chi-Square test). **f)** Representative plots of transcript status for a canonical neuronal gene (*Rbfox3,* which encodes NeuN*)* vs. a microglial gene (*P2ry12*). Each dot represents one cell; units are in transcript counts per cell. Green dots are cells in cluster 3; grey dots are cells in all other clusters. **g**) Ratio of unspliced:spliced transcripts (log_{10}) for enriched genes in clusters 3 and 4, for canonical microglial genes (blue) vs. genes enriched in other cell types (white). "Enriched" = 10x higher FPKM in microglia than the mean of other cell types from (Zhang et al., 2014). Box and whisker plots show data range, median, and first to third quartiles. (Welch's ANOVA with Tamhane's T2 test for multiple comparisons). *Statistics: All tests shown are two-tailed. *p<0.05, **p<0.01, ***p<0.001, ****p<0.0001 unless otherwise noted.*

To directly address whether IFN-I responsiveness precedes a post-neuron-engulfing state, we fate-mapped IFN-I responsive cells using an *Mx1^{Cre};R26R-TdT* reporter (Jax 003556 (Madisen et al., 2010)). 20% of microglia in control cortices at P7 were TdT+ (compared to 1% IFITM3+ cells at P5). This increased to ~50% after deprivation (vs. 12% IFITM3+; **Fig. 4.4k-l)** indicating that many cells not currently expressing IFITM3 were previously IFN-I-responsive. We next examined whether a history of IFN-I responsiveness predicted whether microglia would contain neuronal mRNA. TdT+ microglia were significantly more likely to contain phagocytic cups with *Grin1* mRNA (**Fig. 4.4m-n**). Taken together, these data are consistent with a model in which the IFN-I response is a transient state that precedes complete engulfment of neuronal somas.

Type I interferon deficiency leads to dysmorphic microglia with enlarged phagocytic compartments

To determine whether IFN-I signaling impacts microglial phagocytosis and neuronal engulfment *in vivo*, we examined mice lacking the obligate IFN-I receptor *Ifnar1* (Jax 028288; **Fig. 4.5a**). Microglial IFITM3 expression after whisker deprivation was completely abolished in *Ifnar1$^{-/-}$* mice (**Fig. 4.5b**), confirming that the interferon-responsive microglial subset requires canonical IFN-I signaling. We found that microglia from *Ifnar1$^{-/-}$* mice contained markedly enlarged phagocytic compartments with thin walls enclosing diffuse DAPI+ nuclear material (**Fig. 4.5c-d**). In wild-type microglia these were smaller with condensed DAPI signal that was completely enveloped by the membrane. *Ifnar1$^{-/-}$* microglia (**Fig. 4.5e-f**) frequently contained multiple phagocytic compartments per cell (**Fig. S4.5.7a, Supplemental movie 1)**, reminiscent of 'bubble' microglia observed in zebrafish with deficits in phago-lysosomal fusion(Villani et al., 2019). We found that bubble microglia - defined as containing a DAPI+ phagocytic compartment larger than the microglial nucleus were rare in control mice, representing 5-15% of microglia in control and

deprived cortices respectively. In contrast, up to 40-60% of barrel cortex microglia from *Ifnar1*$^{-/-}$ mice had bubble morphologies (**Fig. 4.5g-h**). Dysmorphic microglia were also increased in other regions of the *Ifnar1*$^{-/-}$ brain, including the corpus callosum and thalamus (**Fig. S4.5.7b-c**.) However, microglial density was unchanged (**Fig. S4.5.7d**.) Microglia from *Ifnar1*$^{-/-}$ animals also exhibited an increase in the accumulation of lysotracker, a dye that labels acidic cellular compartments including late endosomes and lysosomes (**Fig. S4.5.7e-f**). This increase was closely correlated with the increase in CD68 in both genotypes, suggesting that there was not a significant acidification defect (**Fig. S4.5.7g**). Thus, loss of IFN-I signaling results in microglia with an accumulation of enlarged acidified phagolysosomal compartments.

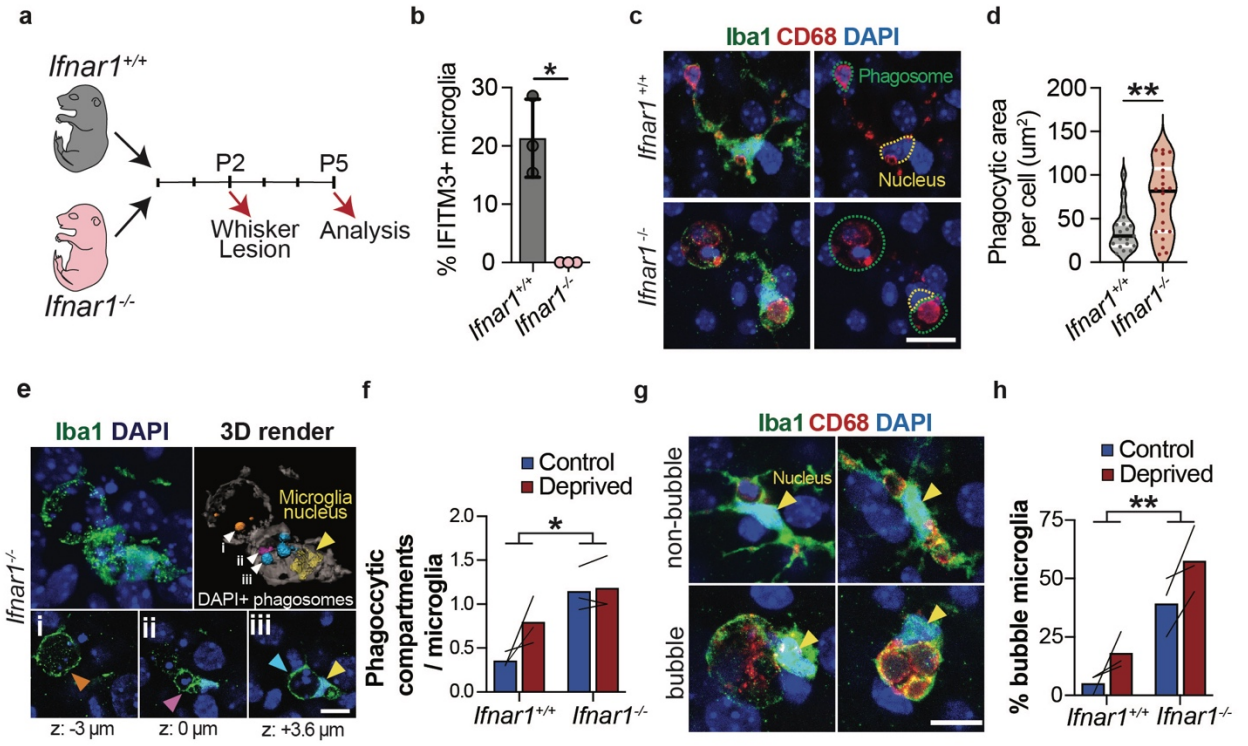

Figure 4.5: Type I interferon deficiency leads to dysmorphic microglia with enlarged phagocytic compartments.

a) Diagram of experimental design comparing control (*Ifnar1*$^{+/+}$) vs. IFN-I insensitive (*Ifnar1*$^{-/-}$) mice. **b**) IFITM3+ microglia in deprived hemispheres (L4-5 barrel cortex) from *Ifnar1*$^{+/+}$ and *Ifnar1*$^{-/-}$ (n = 3 mice, Welch's t-test). **c**) Representative image of microglia from *Ifnar1*$^{+/+}$ and *Ifnar1*$^{-/-}$ mice. (yellow: microglial nucleus, green: phagocytic compartment, Scale = 15 µm) **d**) Total area of phagocytic compartments per microglia in barrel cortex from *Ifnar1*$^{+/+}$ and *Ifnar1*$^{-/-}$ mice. (dots = microglia, n = 3 mice per genotype, Mann-Whitney test). **e**) Representative image and 3D render of microglia with multiple phagocytic compartments in *Ifnar1*$^{-/-}$ mouse (White arrowheads: DAPI+ phagosomes; Yellow: microglial nucleus). Insets: cross sections through each phagosome, colored as in render (Scale

bar = 10 μm). **f)** Phagocytic compartments per microglia in control and deprived cortices from *Ifnar1*$^{+/+}$ and *Ifnar1*$^{-/-}$ Mice. (Lines connect control and deprived hemispheres from individual mice, n = 3 mice/ genotype, 2-way RM ANOVA). **g)** Representative images of "bubble" microglia with rounded phagosomes larger than the microglia nucleus (Scale = 10 μm) **h)** Percent microglia with bubble morphology in control and deprived barrel cortices from *Ifnar1*$^{+/+}$ and *Ifnar1*$^{-/-}$ mice (n = 3 mice per genotype, 2-way RM ANOVA). *Statistics: All tests shown are two-tailed. *p<0.05, **p<0.01, ***p<0.001, ****p<0.0001 unless otherwise noted. Graphs shown as mean ± SD.* ***See also Figure S4.5.7 and Supplemental movie 1.***

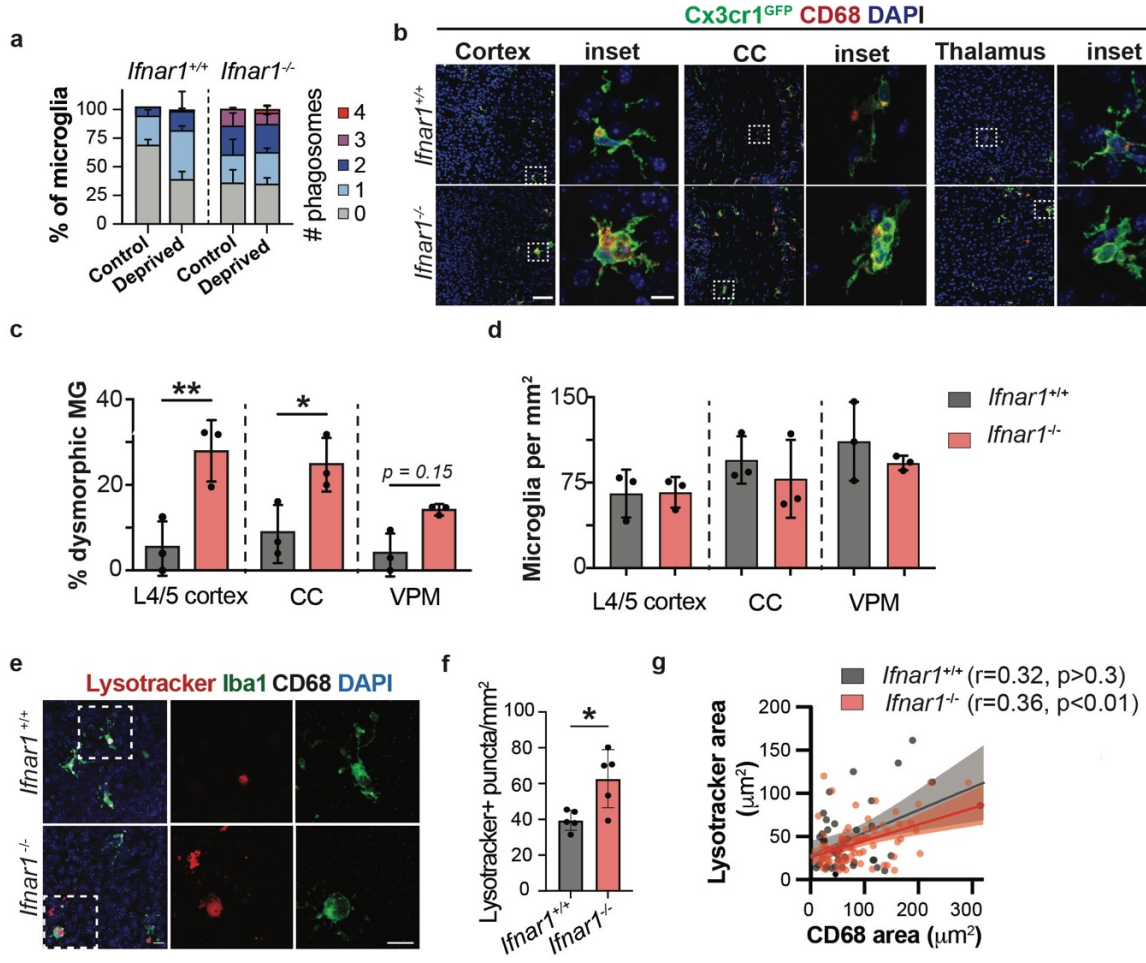

Supplemental Figure 4.5.7: Characterization of dysmorphic microglia in the *Ifnar1*$^{-/-}$ mouse.
a) Data from Fig. 5F plotted to highlight number of phagocytic compartments per microglia. (n = 3 mice per genotype). **b)** Representative images showing microglial morphology in different brain regions. (Scale bar = 50 μm (left, low power), 10 μm (inset, high power)). **c)** Dysmorphic ("bubble") microglia as a percent of total microglia per brain region. (n=3 mice per genotype, 2-way ANOVA with Sidak's post-hoc test). **d)** Microglial density in *Ifnar1*$^{+/+}$ and *Ifnar1*$^{-/-}$ mice by brain region. (n=3 mice per genotype, 2-way ANOVA with Sidak's post-hoc test). **e)** Representative images of LysoTracker Red labeled lysosomes within microglia in *Ifnar1*$^{+/+}$ and *Ifnar1*$^{-/-}$ mice. (Scale bar = 10 μm) **f)** Lysotracker+ puncta within microglia in *Ifnar1*$^{+/+}$ and *Ifnar1*$^{-/-}$ mice (n = 5 mice per genotype, Welch's t-test). **g)** Correlation between CD68 area and Lysotracker area per cell in cells with detectable signal in both channels. (n=5 mice per genotype, r = Spearman correlation coefficient). *Statistics: All tests shown are two-tailed. *p<0.05, **p<0.01, ***p<0.001, ****p<0.0001 unless otherwise noted. Graphs shown as mean ± SD.*

IFN-I signaling restricts the accumulation of damaged neurons

We next examined whether IFN-I deficiency led to broader functional impacts in the developing barrel cortex. As IFN-I responsive microglia were engulfing neurons, we wondered if IFN-I deficiency might lead to an accumulation of dead neurons. Surprisingly, *Ifnar1*$^{-/-}$ mice had significantly fewer TUNEL+ cells, evidence of end stage DNA fragmentation (**Fig. 4.6a-b**). Furthermore, we found that most TUNEL+ cells (60%) in wild-type mice were completely surrounded by microglia and a minority (20%) lacked any microglial contact. In contrast, TUNEL+ cells in *Ifnar1*$^{-/-}$ mice were more likely to be found dying alone (**Fig. 4.6c-d**). A similar deficit in microglial contact was observed with activated Caspase-3+ apoptotic cells (**Fig. S4.6.8a-b**). Thus, IFN-I deficiency leads to fewer dead cells and impaired microglial contact with dying cells.

Given the decrease in cells with end-stage DNA fragmentation in the IFN-I deficient cortex, we next examined earlier stages of DNA damage using the marker 53BP1, which accumulates at double-strand DNA (dsDNA) breaks (Schultz et al., 2000; Ward et al., 2003). These occur in both pathologic and physiologic contexts, including with increased neuronal activity and during development (Madabhushi et al., 2015; Shanbhag et al., 2019). Cells with dsDNA breaks, which were primarily neurons, increased in layer 5 after whisker deprivation (**Fig. S4.6.8c-d**), showing that topographic remapping is a developmental stressor that increases neuronal damage. We also found more cells with dsDNA breaks in the barrel cortex of *Ifnar1*$^{-/-}$ mice than in wild type mice (**Fig. 4.6e-f**), indicating an accumulation of damaged neurons in IFN-I deficient brains.

In wild-type mice, microglia with a projecting morphology (as described in **Fig. 4.3d**) frequently contacted cells with 53BP1+ foci (**Fig. 4.6g-h**). Consistent with this, IFITM3+ cells were more likely than IFITM3- cells to contact damaged neurons labeled by γ-H2AX, an independent marker of dsDNA breaks that colocalized with 53BP1 ((Dickey et al., 2009; Mah et

al., 2010); **Fig. S4.6.8e-g**). We then administered interferon-β (IFN-β) into the lateral ventricle and examined markers of dsDNA breaks 24 hours later. While the vehicle injection induced an increase in DNA damage over baseline, IFN-β exposure induced IFITM expression in microglia and led to a decrease in accumulated DNA damage, as these mice had fewer 53BP1+ puncta per cell (**Fig. S4.6.8h-l**). This supports a model in which IFN-I responsive microglia promote the elimination of damaged but viable neurons, known as phagoptosis (Brown and Neher, 2014).

To directly visualize the impact of IFN-I signaling on microglial-neuronal interactions, we performed live imaging in zebrafish (*Danio rerio*). This is an ideal model system for imaging the intact developing brain with an evolutionarily conserved antiviral IFN-I system (Boudinot et al., 2016; Secombes and Zou, 2017). We activated IFN-I signaling four hours prior to imaging with an intraventricular injection of the viral mimic poly(I:C) into zebrafish expressing the myeloid reporter *Tg(mpeg:EGFP-CAAX)* and the pan-neuronal reporter *Tg(NBT:dsRed*) (**Fig. 4.6i**). We used larvae at 7 days post fertilization, focusing on the optic tectum, which includes a resident population of neuron-engulfing microglia (Peri and Nüsslein-Volhard, 2008; Silva et al., 2021). Microglia in vehicle injected fish had a ramified morphology and made frequent passing contacts with neuronal soma, whereas poly(I:C) exposed microglia were more phagocytic (**Fig. 4.6j**, **Supplemental Movies 2-3).** Poly(I:C) led to a four-fold increase in the percent of microglia engulfing at least one neuron (**Fig. 4.6k**) and increased the percentage of microglia engulfing multiple neurons (**Fig. 4.6l**), similar to what we observed in IFN-responsive murine microglia after whisker deprivation (**Fig. 4.3f-g**). We also classified microglial process behaviors (examples in **Fig. S4.6.8m**). IFN-I stimulation decreased ramified process motility, while increasing phagocytic cup formation and the envelopment and retraction of neuronal soma (**Fig. 4.6m-n).** Thus IFN-I is sufficient to induce microglial neuronal engulfment in zebrafish.

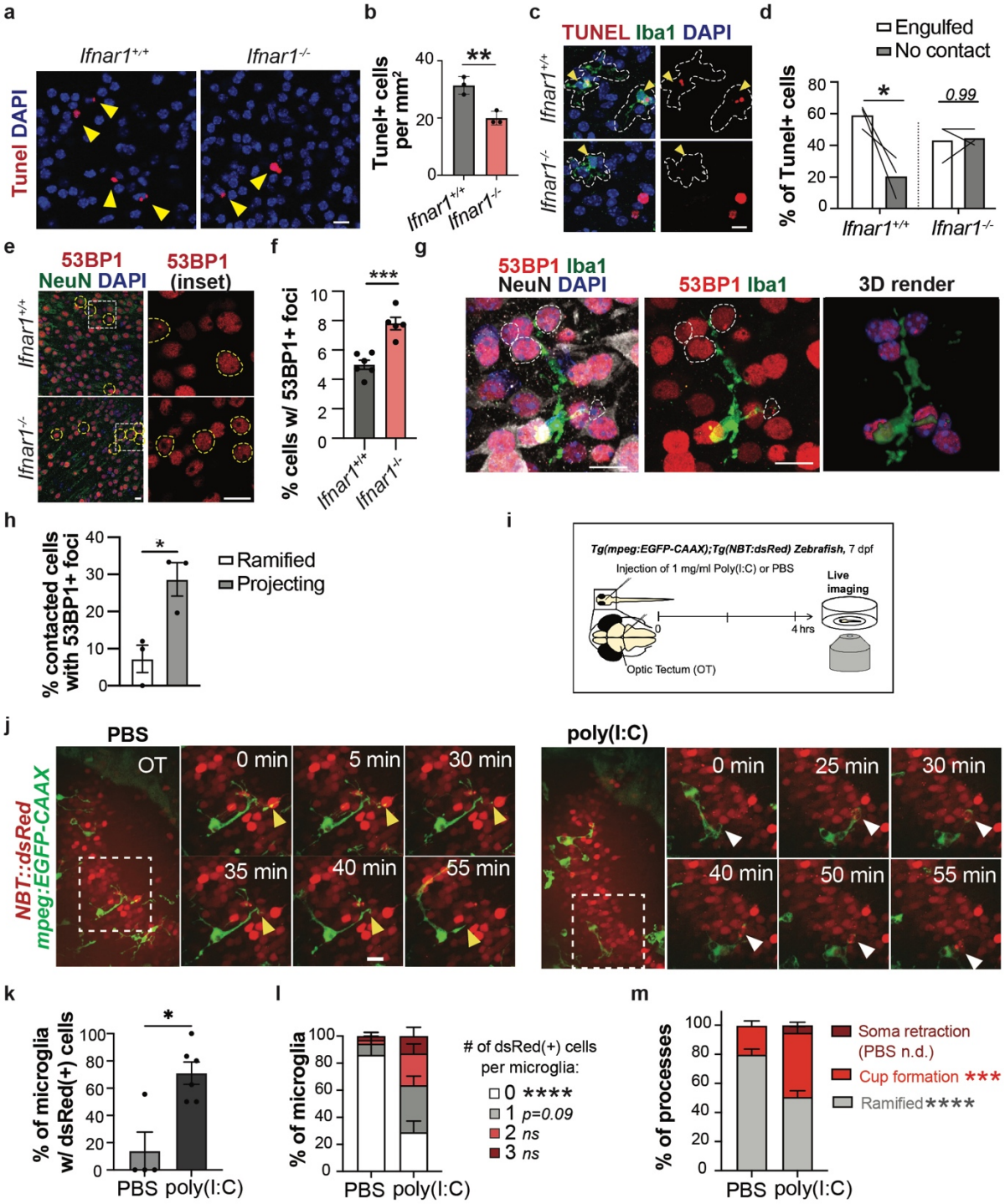

Figure 4.6: IFN-I signaling restricts the accumulation of damaged neurons.

a) Representative image of TUNEL staining in the barrel cortex of *Ifnar1*$^{+/+}$ and *Ifnar1*$^{-/-}$ mice. Arrowheads highlight TUNEL+ cells. (Scale bar = 10 μm). **b)** Quantification of TUNEL+ cells in layers 4-5 of the barrel cortex (n=3 mice per genotype, t-test). **c)** Representative images of TUNEL+ cells with Iba1+ microglia. Dotted lines outline individual microglia (Scale = 10 μm). **d)** Quantification of TUNEL signal inside microglia ("engulfed") vs outside "no contact"). Yellow arrowhead indicates microglial nucleus, which is distinct from TUNEL signal and non-pyknotic. (n = 3 mice per genotype, 2-way RM ANOVA with Sidak post-hoc test). **e)** 53BP1+ neurons in barrel cortices of *Ifnar1*$^{+/+}$ and *Ifnar1*$^{-/-}$ littermates. Yellow dotted lines outline nuclei with 53BP1+ foci, square inset highlights 53BP1staining. (Scale= 10 μm). **f)** Percent of all cells in layer 4 containing foci in *Ifnar1*$^{+/+}$ and *Ifnar1*$^{-/-}$ mice (n=6 *Ifnar1*$^{+/+}$and 5

Ifnar1$^{-/-}$ mice, t-test). **g)** Representative image showing contact between a projecting microglia and 53BP1+ foci-containing neuron. White dotted lines outline nuclei with 53BP1+ foci. 3D render (right), isolates only nuclei (blue) in contact with the microglia (green). (Scale = 10 µm) **h)** Percent of cells with 53BP1+ foci in contact with ramified or projecting microglia (dots=mice, 2-3cells/mouse, t-test). **i)** Diagram showing parameters for zebrafish poly(I:C) injection and live imaging experiment. **j)** Still image (left) and insets showing individual frames (0-55 minutes, region shown by white dotted rectangle) from live imaging of green microglia(*Tg(mpeg:EGFP-CAAX))* and red neurons (*Tg(NBT:dsRed)*) in the zebrafish optic tectum after intraventricular injection of PBS (top) or poly(I:C) to induce an interferon response. The yellow arrowhead shows a single neuron that is contacted by a microglial process but not engulfed. The white arrowhead shows a neuron that is contacted, engulfed, and trafficked towards the microglial soma. (Scale bar = 10 µm). **k**) Quantification showing the percent of microglia engulfing at least one DsRed+ cell during the hour-long video. Each dot represents one fish. (n= 4 PBS, 6 poly(I:C), Mann-Whitney test). **l**) Quantification showing the percent of microglia engulfing 0, 1, 2, or 3 DsRed+ cells during image acquisition. (n = 4 PBS, 6 poly(I:C), 2-way ANOVA with Sidak post-hoc test). **m**) Percent of microglial processes with each of three morphologies (examples are shown in fig. S8). (n = 4 PBS, 6 poly(I:C), 2-way ANOVA with Sidak post-hoc test). *Statistics: All tests shown are two-tailed. *p<0.05, **p<0.01, ***p<0.001, ****p<0.0001 unless otherwise noted. Graphs shown as mean ± SD (bar graphs) or mean ± SEM (stacked bar graphs).* ***See also Figure S4.6.8 and Supplemental Movies 2-3.***

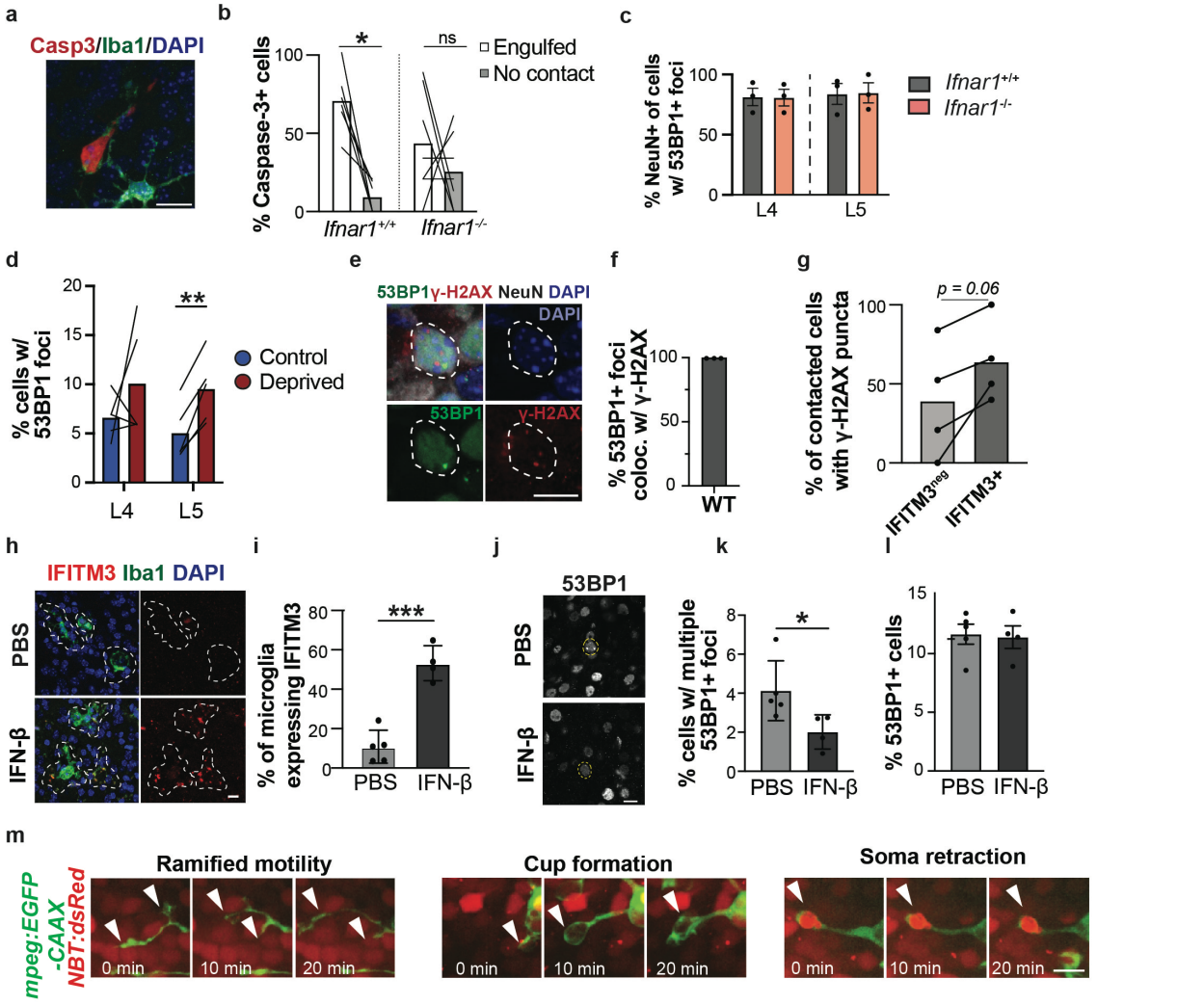

Supplemental Figure 4.6.8: Additional analysis of microglial contact with markers of neuronal cell stress and apoptosis.

a) Representative micrograph of a microglia (green, Iba1) contacting a Caspase-3+ neuron (red). Scale= 10 µm. **b)** Quantification of microglial contact with cleaved caspase-3+ cells in *Ifnar1*$^{+/+}$ and *Ifnar1*$^{-/-}$ mice. White bars: % of

caspase+ cells completely engulfed by a microglia. Grey: % of caspase-3+ cells with no microglial contact. The remaining cells were in partial contact but not engulfed as shown in g. (n = 6 *Ifnar1*$^{+/+}$ mice, 7 *Ifnar1*$^{-/-}$ mice, 2-way RM ANOVA with Sidak's post-hoc test). **c)** Percent of 53BP1+ foci-containing cells that also express the neuronal marker NeuN (n = 3 mice per genotype). **d)** Percent cells with 53BP1+ foci in control vs. whisker deprived barrel cortex in layer 4 (L4) or layer 5 (L5), lines connect control and deprived cortices from individual mice (n=5 mice, 2-way RM ANOVA with Sidak's post-hoc test). **e**) Representative images showing colocalization of γ-H2AX and 53BP1 foci within a neuronal nucleus. (Scale bar = 5 μm) **f)** Quantification of percent 53BP1 foci+ cells that also had γ-H2AX+ foci. (n=3 mice, paired t-test). **g)** Quantification of the percent of cells in contact with microglia lacking IFITM3 protein expression (IFITM3^{neg}) or expressing IFITM3 (IFITM3^{+}) that have at least one γ-H2AX puncta. (n=3 mice, paired t-test). **h)** Representative image of IFITM3 expression in microglia 24 hours after IFN-β or PBS i.c.v. injection at P4. Dotted lines outline individual microglia (Scale bar = 10 μm). **i)** Quantification of percent of microglia expressing IFITM3 protein following PBS or IFN-β i.c.v. injection. (n = 5 mice with PBS, 4 mice with IFN- β, t-test). **j**) Representative image of 53BP1+ foci in L2/3 cortex 24 hours after PBS or IFN-β-injection (scale = 10 μm). **k)** Quantification of cells containing multiple (>2) 53BP1+ foci 24 hours after PBS or IFN-β injection (n = 5 mice with PBS, 4 mice with IFN- β, t-test). **l)** Quantification showing percent of cells containing 53bp1 foci following PBS or IFN-β injection. (n = 5 mice with PBS, 4 mice with IFN- β). **m)** Representative images defining the labels used in Fig. 6m. White arrowheads show interactions between the microglial process (*mpeg:EGFP-CAAX*) and surrounding neuronal cell bodies (*NBT:dsRed*). (Scale bar = 10 μm). *Statistics: All tests shown are two-tailed. *p<0.05, **p<0.01, ***p<0.001, ****p<0.0001 unless otherwise noted. Graphs shown as mean ± SD.*

Microglia upregulate a conserved interferon-response signature in pathology

To determine if the induction of this interferon-responsive microglial subset is unique to developmental cortical remodeling, we examined murine microglial bulk transcriptomic datasets from a variety of physiological and pathological conditions, including some in which interferon responses have previously been observed (**Fig. 4.7a**, **Supp. Table 4.2;** (Friedman et al., 2018)). As expected, we found the greatest enrichment of the interferon-response signature after viral infection (lymphocytic choriomeningitis, LCMV). However, we also detected prominent induction of the same interferon response genes upregulated in cluster 8 in various sterile pathologies, including mouse models of brain tumors and of Alzheimer's disease (AD). We found similar results across a variety of single cell datasets including AD models, glioblastoma models, Sars-CoV-2 infection, demyelinating injury (LPC, Cuprizone treatment), aging, and middle cerebral artery occlusion (**Fig. S4.7.9a-b, Supp. Table 4.3**, (Friedman et al., 2018; Frigerio et al., 2019; Hammond et al., 2019; Lee et al., 2021a; Masuda et al., 2019; Ochocka et al., 2021; Shi et al., 2021; Syage et al., 2020; Zhan et al., 2020)).

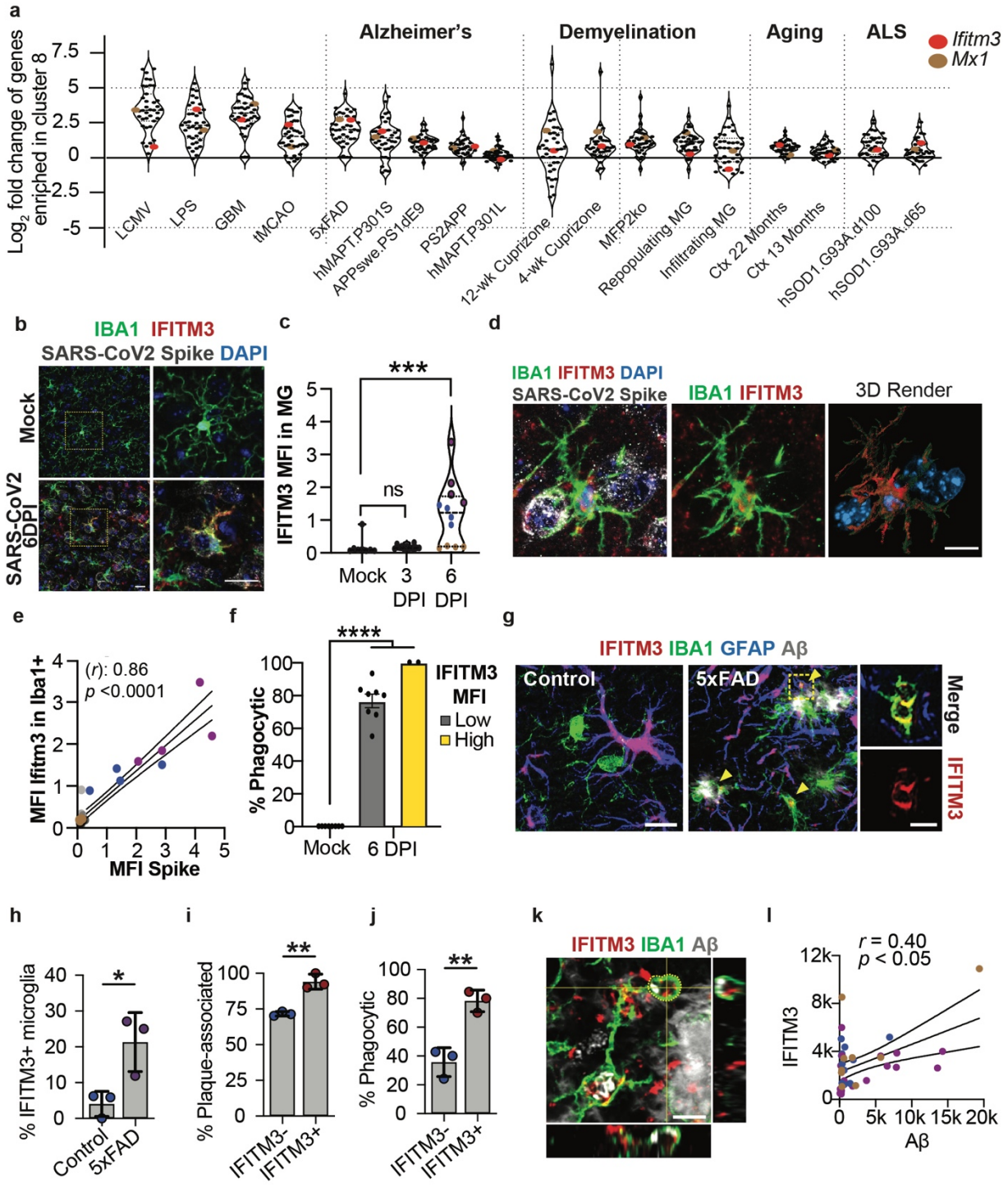

Figure 4.7: Microglia upregulate a conserved interferon-response signature in pathology.
a) Expression of 38 'cluster 8' marker genes across a set of published microglia sequencing data (from bulk sorted CD11b+ cells (Friedman et al., 2018). Dots represent individual genes, highlighting *Ifitm3* (red) and *Mx1* (orange). Y-axis represents the log-fold-change relative to the control in that dataset. See Supplementary Table 6.2 for details of each sample set and experimental condition. **b**) Representative images in somatosensory cortex showing IFITM3 staining in Iba1+ microglia from mock vs. SARS-CoV-2 infected mice 6 days post infection (DPI) (left: low power,

right: inset, single microglia, Scale bar = 20 μm). **c**) Quantification of IFITM3 mean fluorescence intensity within microglia. Each color represents an individual mouse. (n=2 mock-infected mice, 3 each at 3 and 6 days post infection, Kruskal-Wallis test). **d)** Representative image and 3D reconstruction of an IFITM3+ microglia engulfing a SARS-CoV-2 infected cell. (Scale= 10 μm). **e**) Correlation of SARS-CoV-2 Spike protein vs. microglial IFITM3 per field of view. Colored by mouse (n = 3 mice at 6 DPI, r = Spearman correlation coefficient). **f**) Percent phagocytic microglia in cortices of mock-infected vs. SARS-CoV-2 infected mice at 6 dpi, binned by IFITM3 expression per cell (see Methods for details). (Dots are fields of view from n = 2 mice/group, Kruskal-Wallis test). **g**) Representative images of microglia in hippocampi of 12-month old 5xFAD and age matched control mice, labeled with IFITM3, microglia (IBA1), astrocyte (GFAP), and Aβ (FSB dye). Inset: the plaque-adjacent phagocytic cup outlined in yellow. **h)** Percent IFITM3+ microglia in 5xFAD and control hippocampi. (n = 3 mice per group, t-test)**. I**) Percent of microglia in IFITM3+ and IFITM3- populations within 10 μm of an Aβ plaque (n = 3 mice, t-test). **j**) Percent of microglia in IFITM3+ and IFITM3- populations containing a phagocytic compartment (n = 3 mice, t-test). **k**) Confocal image and orthogonal projection of a plaque-associated IFITM3+ microglia with an Aβ+ (4G8 antibody) IFITM3+ phagocytic cup. (Scale bar = 5 μm). **l)** Correlation of Aβ and IFITM3 mean fluorescence intensity per phagocytic compartment. (Colored per mouse, r = Spearman correlation coefficient). *Statistics: All tests shown are two-tailed. *p<0.05, **p<0.01, ***p<0.001, ****p<0.0001 unless otherwise noted. Graphs shown as mean ± SD.* ***See also Figures S4.7.9-S4.7.10, Supplemental Tables 4.2-4.3.***

We observed high levels of IFITM3 in most microglia in brains with active replication of SARS-CoV-2 in a mouse model of coronavirus infection which was detectable in 2 out of 3 mice at 6 days post infection (DPI) and 0 out of 3 mice at 3 DPI, as assessed by Spike and N-protein expression **(Fig. 4.7b-c**; (Carossino et al., 2021; Kumari et al., 2021)). IFITM3 intensity was strongly correlated with infection of nearby neurons, as assessed by Spike protein intensity (r=0.93, **Fig. 4.7d-e**). We detected an increase in IFITM3 in both microglia and non-microglial cells, while infected cells were almost exclusively NeuN+ neurons, with highest levels in cortex and hippocampus and undetectable levels in the cerebellum (**Fig. S4.7.10a-d**). Microglia expressing higher levels of IFITM3 were also more likely to form phagocytic cups around SARS-CoV-2 Spike+ cells (**Fig. 4.7d,f, Fig. S4.7.10e**) and were more likely to have an amoeboid morphology (**Fig. S4.7.10f**).

Type I interferon responses may exacerbate pathology in aging and Alzheimer's disease (AD) (Baruch et al., 2014; Friedman et al., 2018; Frigerio et al., 2019; Minter et al., 2016; Orre et al., 2014; Roy et al., 2020), thus we examined whether IFITM3+ microglia could also be identified in an AD mouse model *in situ*. We examined 5xFAD mice, characterized by early Aβ deposition

and plaque formation followed by decreased performance on cognitive tasks and neuronal loss by 9 months (Oakley et al., 2006). In 12 month old 5xFAD mice, we observed that 21% of microglia in the ventral hippocampus were IFITM3+, whereas few were detected in aged-matched controls (**Fig. 4.7g-h**). We also detected IFITM3 in astrocytes as previously described(Hur et al., 2020), which was ubiquitous throughout the hippocampus in both control and 5xFAD settings and enriched in a GFAP+ cytoskeletal pattern. IFITM3+ microglia were significantly more likely to be associated with amyloid plaques than IFITM3- microglia and were twice as likely to contain at least one phagocytic cup (**Fig. 4.7i-j**). As in the developing cortex, these phagocytic cups were enriched for IFITM3 protein (**Fig. 4.7g, k**). We observed a positive correlation between IFITM3 levels within phagocytic cups and the amount of engulfed Aβ (**Fig. 4.7k-l**), although we did not observe phagocytic cups around neuronal soma at this time point. These data indicate that IFN-I responsive microglia are present in the model. However, as Aβ phagocytosis is molecularly distinct from whole cell engulfment (Huang et al., 2021; Lemke, 2019; Márquez-Ropero et al., 2020; Mazaheri et al., 2014b), the functional impact of IFN-I responsive microglia in this context remains to be determined. For example, they could play a distinct phagocytic role, such as limiting plaque deposition (Hansen et al., 2018; Liu et al., 2010), or alternately their induction could lead to a bystander effect that exacerbates neuronal loss.

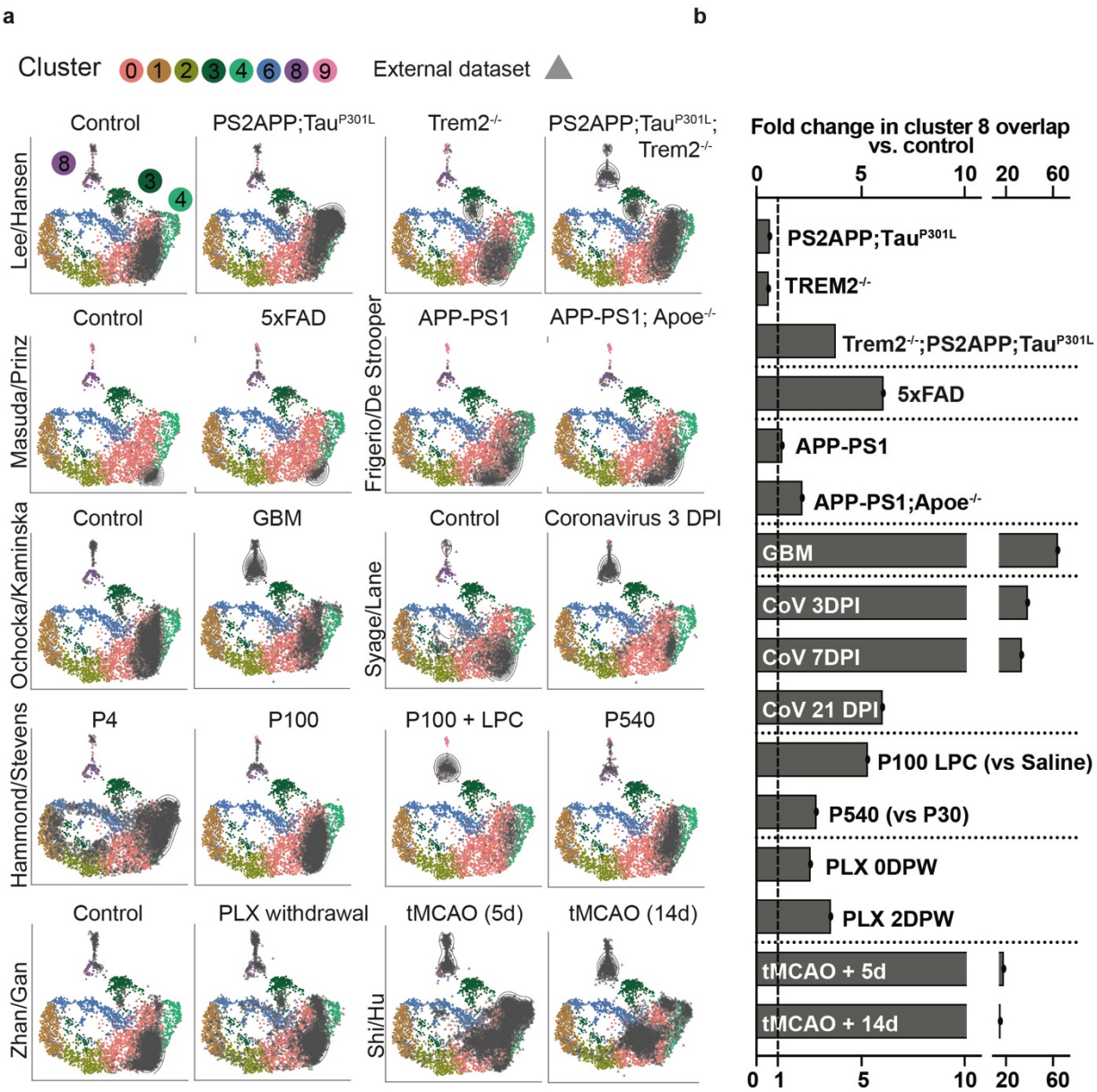

Supplemental Figure 4.7.9: Comparison of single-cell microglial sequencing in various disease and aging models with IFN-I responsive cluster 8.

a) Comparison of various microglial single-cell sequencing datasets from different disease states and ages with the single-cell dataset analyzed in this paper. The microglial P5/P7 dataset (colored dots) was reclustered to create a reference PCA and UMAP map which other datasets (grey triangles) were aligned to. Published datasets shown are described and referenced in Supplementary Table 6.3 (Frigerio et al., 2019; Hammond et al., 2019; Lee et al., 2021a; Masuda et al., 2019; Ochocka et al., 2021; Shi et al., 2021; Syage et al., 2020; Zhan et al., 2020). **b)** Bar plot showing enrichment of cluster 8-like cells in the datasets shown in a) relative to the controls used in each study.

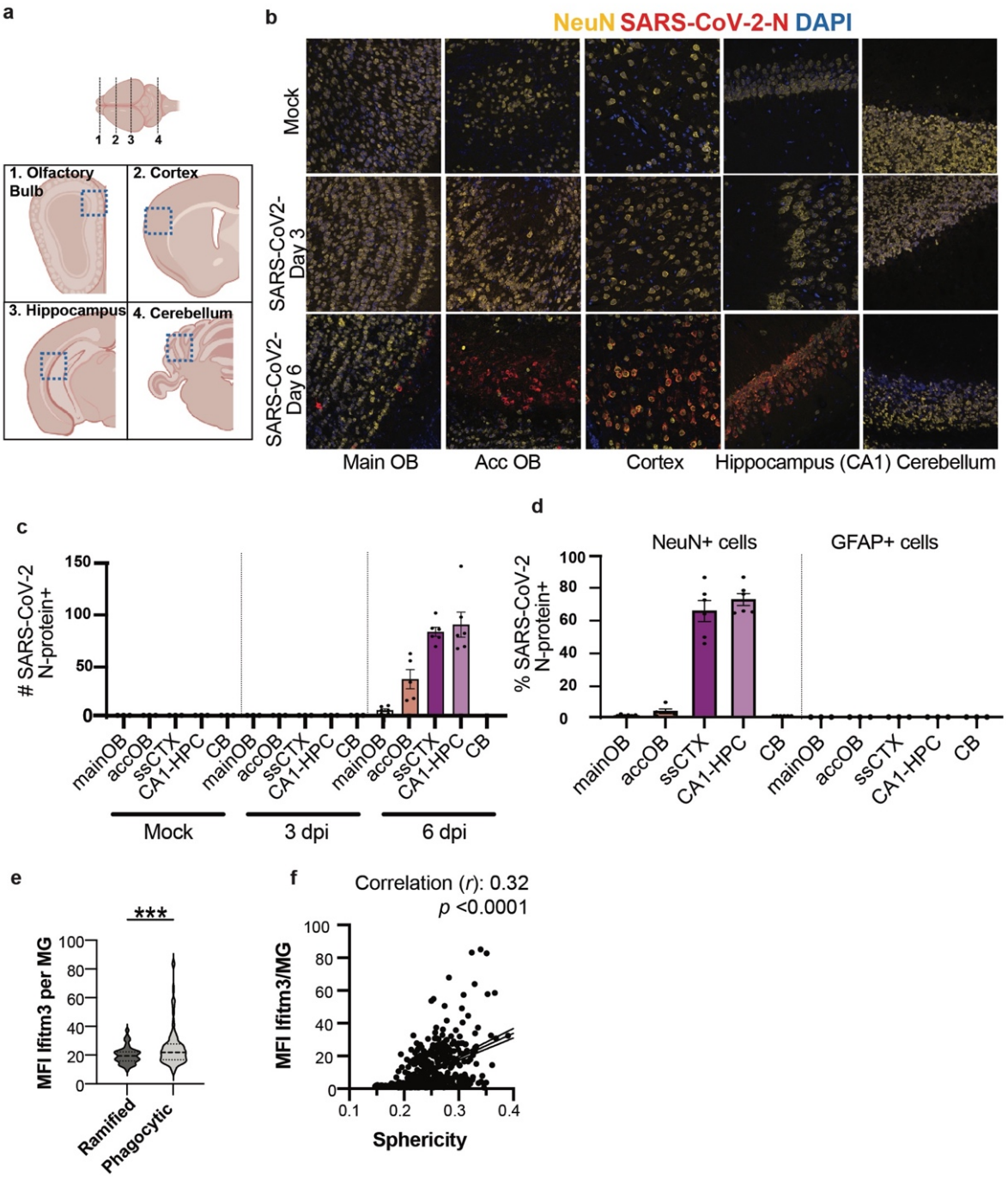

Supplemental Figure 4.7.10: Characterization of neurotropic SARS-CoV-2 infection.
a-b) Schematic and representative images of brain regions after mock infection, and 3 or 6 days post SARS-CoV-2 infection, labeled for SARS-CoV-2 N-protein and NeuN (neurons). Main OB: Olfactory Bulb, Acc OB: Accessory Olfactory Bulb, Cortex: somatosensory. **c**) Number of SARS-CoV-2 N-protein+ cells in the indicated brain regions in mock infected, 3 dpi, and 6 dpi mice. (n=2 mice per condition). **d**) Neurons (NeuN+), astrocytes (GFAP+) or microglia (Iba1+) positive for SARS-CoV-2 N-protein at 6 dpi. (3 images per region from each of n=2 mice). **e**) Quantification of IFITM3 intensity in phagocytic and non-phagocytic (ramified) cells from SARS-CoV-2 infected brains at 6 dpi (n = 2 mice, Welch's t-test). **f**) Correlation of microglial sphericity and IFITM3 intensity in Iba1+ cells from mock and infected brains. (n = 2 mock, 3 mice at 3 DPI, 3 mice at 6 DPI, r = Spearman correlation coefficient). *Statistics: All tests shown are two-tailed. *p<0.05, **p<0.01, ***p<0.001, ****p<0.0001 unless otherwise noted. Graphs shown as mean ± SD.*

Discussion

This study defines a coordinated set of functional state changes in microglia in response to developmental barrel cortex remodeling. We identified an interferon-responsive, highly phagocytic population that emerged transiently in microglia during topographic remapping and was required for effective neuronal engulfment during development. IFN-I responses are a central component of antiviral defense, and have been linked to phagocytosis in some pathogenic contexts, but their role in physiology is comparatively unknown (Brendecke and Prinz, 2012; Ivashkiv and Donlin, 2014; Kumaran Satyanarayanan et al., 2019; Ranjbar et al., 2015). The IFN-I responsive microglial subset characterized here is rare but detectable in the normally developing cortex, yet up to 40% of microglia are dysmorphic in mice lacking IFNAR1, suggesting that IFN-I microglia are rare not because they are dispensable but because they represent a highly transient microglial state. The observation that IFN-I responsive microglia are frequently digesting one cell while in the process of enclosing another, along with the characteristic 'bubble' phenotype of multiple phagosomes per cell in IFN-I deficiency, strongly suggests that IFN-I signaling accelerates phagocytosis in settings where cell turnover is high.

Our data reveal that intact IFN-I signaling in the developing brain optimizes the efficient elimination of damaged neurons. Many outstanding questions remain, including which cells release IFN-α/β, what signals drive microglia to engulf specific cells, and whether cells are eaten dead or alive (Brown and Neher, 2014; Fourgeaud et al., 2016b; Marín-Teva et al., 2004; Wakselman et al., 2008). Transcriptomic data suggests that microglia themselves could be a source of IFN-β (Zhang et al., 2014). One potential model is that exposure to damage associated molecular patterns (DAMPs) from stressed cells (Boada-romero et al., 2020; Chen et al., 2016) triggers conserved responses adapted to detect nucleic acids (Kawai and Akira, 2006; Li et al.,

2019b; Takaoka and Yamada, 2019; Wu and Chen, 2014), triggering an autocrine loop which enhances phagocytic efficiency via IFN- α/β release. In this model, physiological and self-contained engulfment events could become pathological if high IFN-I tone or abundant nucleic acids trigger a more widespread microglial response and lead to indiscriminate cell death and neuroinflammation.

Consistent with this proposed model, our data reveal the expansion of an IFN-I responsive microglial subset in pathology. While an IFN-I response is expected during neurotropic viral infection, as we observed in a SARS-CoV-2 model, the association of interferon-responsive microglia with virally infected neurons could prompt further inquiry into potential pathogenic mechanisms. Given emerging reports of neuropsychiatric sequelae following COVID-19 infection in humans (Song et al., 2021; Taquet et al., 2021), defining whether this microglial subset is present in human samples or in other animal models may be fruitful (Imai et al., 2020; Montagutelli et al., 2021; Sia et al., 2020). Furthermore, we characterize a distinct interferon-responsive microglial subset *in situ* that associates with Aβ plaques in the 5xFAD model of Alzheimer's disease. This is consistent with multiple reports of IFN-I involvement in aging and Alzheimer's disease (Baruch et al., 2014; Deczkowska et al., 2017; Frigerio et al., 2019; Hur et al., 2020; Moore et al., 2020; Roy et al., 2020), and suggests potential roles for an IFN-I induced cell state in regulating Aβ deposition. Abundant IFITM3 staining in other cell types including astrocytes points to a coordinated role of IFN-I signaling in response to widespread cellular stress or damage (Hasel et al., 2021; Roy et al., 2020). Ultimately, determining the context-specific mechanisms of microglial engulfment will enable therapeutics to target aspects of phagocytosis while preserving microglial homeostatic functions.

Additional media

Supplemental movie 1: Imaris reconstructed video scanning through the z-axis of a dysmorphic bubble microglia shown in figure 4.5e. Green = Iba1 (microglia), blue = Dapi (nucleus), red = CD68 (lysosomes).

Supplemental movies 2-3: Representative live imaging videos of microglia (*Tg(mpeg:EGFP-CAAX))* and neurons (*Tg(NBT:dsRed)*), from vehicle injected (Supplemental movie 2) or polyI:C injected (supplemental movie 3) Each frame consists of one 50 μm z-stack acquired once every 5 minutes, and each video was acquired over one hour.

Table 4.2: Extended legend for Fig. 4.7a (excel file).

Extended legend for **Figure 4.7a** including references for all publicly available bulk microglial sequencing datasets used. Adapted from (Friedman et al., 2018), Fig. 4.

Table 4.3: Extended legend for Fig. S4.7.9 (excel file).

Extended legend for **Figure S4.7.9**, including references for all publicly available published single cell sequencing datasets used.

Table 4.4: Summary of statistical analyses (excel file).

Acknowledgements: We are grateful to members of the Molofsky Lab for helpful comments on the manuscript, Dr. Rafael Han for assistance with tissue preparation, and Dr. Ari Molofsky for helpful feedback on the manuscript. Thanks to the Chan-Zuckerberg BioHub for sequencing support. **Funding*:*** A.V.M is supported by the Pew Charitable Trusts, NIMH (R01MH119349 and DP2MH116507), and the Burroughs Welcome Fund. T.J.N. was supported by NIMH RF1MH121268. L.C.D. received support from the Matilda Edlund Scholarship and the Genentech Fellowship. P.T.N. is supported by a graduate research fellowship from the National Science Foundation (Grant #1650113). C.E. was supported by a gift from Marilyn Waldman. C.C. was supported by NIA RF1AG061874.

Data availability: Supplement contains additional data. All data needed to evaluate the conclusions in the paper are present in the paper or the Supplementary Materials. Searchable database available at https://www.annamolofskylab.org/microglia-sequencing. RNA sequencing data is available through GEO at GSE173173. Any additional data needed to evaluate the paper will be provided upon request.

Code availability: R and Python code used to analyze single cell datasets is available on GitHub at https://github.com/lcdorman/IFNresponseCode.

Methods

Mice: All mouse strains were maintained in the University of California San Francisco specific-pathogen–free animal facility, and all animal protocols were approved by and in accordance with the guidelines established by the Institutional Animal Care and Use Committee and Laboratory Animal Resource Center (LARC). Mice were housed in a 12-hour light/dark cycle (7 am-7pm) at 68-79° F and 30-70% humidity. Littermate controls were used for all experiments when feasible, and reporter mice were backcrossed >10 generations on a C57Bl/6 background (Cx3cr1-GFP) or Swiss-Webster (Aldh1l1-eGFP). The following mouse strains used are described in the table below and are as referenced in the text: Cx3cr1-GFP (JAX #00582); Aldh1l1-eGFP (Gensat); Ifnar1$^{-/-}$ (JAX #028288); Mx1-GFP (JAX #033219); Mx1-Cre (JAX #003556); Ai14 (JAX #007908); B6.Cg-Tg(K18-ACE2) 2Prlmn/J (JAX #034860); B6SJLTg (APPSwFlLon, PSEN1*M146L*L286V) 6799Vas/ Mmjax (5xFAD, JAX #34840-Jax); Rorb-Ires2-Cre-D (Jax **023526**); Aldh1l1-tdTomato (MMRRC, RRID:MMRRC_036700-UCD)

Zebrafish: Fish were maintained in recirculating habitats at 28.5 ºC and on a 14/10-h light/dark cycle. Embryos were collected after natural spawns and incubated at 28.5 ºC. Larvae were imaged at 7 days post fertilization (dpf), a developmental stage at which sex cannot be determined. In this study, we used the double transgenic fish *Tg(mpeg:EGFP-CAAX);Tg(NBT:dsRed)* (zfin ID: ZDB-TGCONSTRCT-191211-1 and ZDB-TGCONSTRCT-081023-2) on a casper background to visualize microglia and neurons. All zebrafish protocols were approved by and in accordance with the ethical guidelines established by the UCSF Institutional Animal Care and Use Committee and Laboratory Animal Resource Center (LARC).

Whisker Follicle Lesions: Whisker follicle ablations were performed under hypothermia-induced anesthesia and followed by topical application of lidocaine for pain management. Postnatal day two pups were anesthetized for 3 minutes in ice. An incision was made in the whisker pad along whisker rows B and D of one side of the face, and silver nitrate was used to cauterize the exposed whisker follicles in that row. After topical 2% lidocaine application the mice were reacclimated on a heating pad for at least 15 minutes before being returned to their home cage.

Immunohistochemistry and Confocal Microscopy: For all analyses of barrel cortex, mice were perfused transcardially with ~10 mL of ice-cold PBS followed by ~10 mL of 4% (weight/volume) paraformaldehyde diluted in PBS. For analyses of SARS-CoV-2 infected brains, animals were not perfused and were post fixed by immersion in 4% PFA for 72 hours prior to cryoprotection and sectioning. All other brains were post-fixed in 4% PFA for a minimum of 4 hours and then transferred to a 30% sucrose solution for a minimum of 24 hours. Tangential sections (flat mounts) of the barrel cortex were obtained by dissecting the cortex from the diencephalon following perfusion and flattening the dissected cortices ventral side down between two cryomolds. The sections were placed in between flat toothpicks laid horizontally in the cryomold, and the second mold was pressed down on top of the toothpicks to maintain uniform thickness. Brains were then flash frozen and sliced on a HM 440E freezing microtome (GMI Instruments) or embedded in OCT following 30% sucrose treatment and frozen at -80°C for a minimum of 1 day and then sectioned on a CryoStar NX70 Cryostat (Thermo Fisher) before being mounted on coverslips. Sections from control and deprived hemispheres of individual mice were mounted on the same slides for all experiments.

See resource table below for details of all antibodies used. Immunohistochemistry was performed as follows: brain sections were incubated in a blocking solution consisting of 5% normal goat serum (Thermo Fisher) and 0.1% Triton (Sigma-Aldrich) diluted in 1X PBS. Primary antibodies were diluted in 3% normal goat serum in 0.1% Triton and tissue was incubated on a shaker overnight at 4°C. Secondary antibodies were diluted in 3% normal goat serum and tissue was incubated on a shaker for 2 hours at room temperature. Brain sections were mounted on coverslips with ProLong Gold or Glass (Thermo Fisher) for all imaging. For staining with IFITM3 (Thermo Fisher #11714-1-AP), secondary antibody staining was done with goat anti-rabbit IgG, HRP-linked (Cell Signaling Technology #7074) and visualized with TSA Plus Cy3 detection system (Akoya Biosciences #NEL744001KT). For staining with SARS-CoV-2 Spike and N protein antibodies (GeneTex), an additional antigen retrieval step (70°C for 10min) was performed prior to blocking. Slides were imaged on an LSM 800 confocal microscope (Zeiss, Zen 2.6 software) using 20x, 40x, and 63x objectives. For analysis of phagocytic cups, slides were imaged on LSM 880 confocal microscope with AiryScan (Zeiss) using a 63x objective. All antibodies used are referenced in **Table 4.6**.

Fluorescent In Situ Hybridization (FISH): FISH experiments were performed using the RNAscope Multiplex Fluorescent Reagent Kit v1 assay for *Htra1* and v2 assay for *Grin1* and *Rbfox3* (ACD Bio) as described by the manufacturer for fixed-frozen tissue, but eliminating the 60°C incubation and post-fixation steps prior to tissue dehydration. Brains were embedded in OCT following 30% sucrose treatment and frozen at -80°C for a minimum of 1 day prior to sectioning. Mouse *Htra1* RNAscope Probe (ACD Bio #423711-C2), Mouse *Grin1* RNAscope Probe (ACD Bio #431611-C1) and mouse *Rbfox3* Probe (ACD Bio #313311-C2) were used to detect each

transcript. For immunohistochemical labeling with antibodies following the RNAscope assay, tissues were incubated with blocking and antibody solutions as described above immediately after RNAscope and washing four times, 5 minutes each. Confocal optical sections were imaged on a Zeiss 700 at 63x magnification through layer IV of flattened *en face* cortical sections of the barrel cortex. The Htra1 channel was thresholded to remove puncta smaller than 0.06 um^2 in area, and the puncta within a 10 μm radius of each Aldh1l1-GFP+ astrocyte were counted. Three images each from at least two sections each of three separate mice were counted per condition.

Flow cytometry: For all flow cytometry experiments, animals were perfused transcardially with ice-cold D-PBS, mounted coronally in ice-cold isolation media (HBSS, 15 mM HEPES, 0.6% glucose, 1 mM EDTA pH 8.0) and 350 micrometer slices were prepared on a vibratome. A stereomicroscope was used to visually identify barrel regions; 1 mm^3 of tissue was collected per hemisphere. All data analysis was performed using FlowJo™ software.

For single cell sequencing of non-neuronal cells from the cortex, cells were isolated using a protocol modified from Adam et al 2017. Barrel cortex was enzymatically dissociated with psychrophilic proteases (PBS with 4 μL/mL DNAse (Sigma D4527-40KU), 5 mg/mL protease (Creative Enzymes NATE-0633, 175 ug/mL L-cysteine) incubated on ice for 20 minutes with gentle trituration every 5 minutes until tissue chunks were no longer visible. Cells were centrifuged at 300g for 5 minutes at 4°C.

For isolation of astrocytes and microglia with Papain, barrel cortex tissue was dissociated in 20 U/mL papain (Worthington) in dissociation buffer (Ca/Mg-free HBSS with phenol red, 1 mM L-cysteine, 22.5 mM D-glucose, 0.5 mM EDTA, 20 ug/mL DNAse) for 80 minutes at 34° C with shaking every 15 minutes. The dissociation reaction was stopped with 1 mg/ml ovomucoid trypsin inhibitor and the cells were pelleted by centrifugation at 300g for 5 minutes at room

temperature. After removing the supernatant and triturating in fresh ovomucoid solution, myelin debris was eliminated by centrifuging in a 22% Percoll gradient at 900g for 20 minutes (acceleration 4, brake 1, 4° C). Pelleted cells were then washed with isolation medium and incubated in blocking solution consisting of anti-mouse CD16/32 antibody (Biolegend). Cells were sorted on a BD FACS Aria III and gated on forward/side scatter, live cells by Hoechst, CD11b-PE (eBioscience), and CD45-FITC (BioLegend) to identify, sort for, and enrich microglia. Microglia (CD11b+) and other cells were sorted into the blocking media described above and mixed at a ratio of 1/3 microglia: 2/3 non-microglial cells for 10x sequencing. Sorted cells were pelleted in an 87Eppendorf tube at 300 g for 5 minutes at 4°C and then resuspended in blocking buffer consisting of 1% (weight/volume) Rnase-free BSA and 1X PBS for downstream sequencing.

MACS Bead Isolation: For sorting microglia only for downstream RNA-sequencing, cells were isolated as described previously (Galatro et al., 2017). Briefly, barrel cortices dissected as described above were mechanically dissociated using a glass tissue homogenizer in isolation medium (HBSS, 15 mM HEPES, 0.6% glucose, 1 mM EDTA pH 8.0). Cells were filtered and then pelleted at 300 g for 10 minutes at 4°C before being resuspended in 22% Percoll (GE Healthcare) and centrifuged at 900 g for 20 minutes with acceleration set to 4 and deceleration set to 1 in order to remove cellular debris. Pelleted microglia were then resuspended in staining media (PBS, 0.5% BSA, 2 mM EDTA) and incubated with CD11b MACS beads (Miltenyi, 1:50) for 15 minutes at 4°C. The cells were washed with staining buffer, pelleted at 300 g for 5 minutes at 4°C, and reconstituted in 500 uL staining buffer. Microglia were isolated as described in the manual for MACS LS columns and collected in staining buffer without EDTA, pelleted at 300 g for 5 minutes

at 4°C , counted on a hemocytometer, and 15,000-20,000 cells were diluted in 30 μL in a BSA-coated plate for 10x sequencing.

Single cell RNA-sequencing: Single cells were isolated as described above.

Pan-Glial isolation (Figure 1): Approximately 2,000 cells (v2, **Fig.**1-2) from each sample were loaded into each well of Chromium Chip A according to the manufacturer instructions and combined into droplets with barcoded beads using the Chromium controller. Libraries were prepared by the Gladstone Institutes Genomics Core following the instructions in the Chromium Single Cell 3' Reagent Kits version 2 user guide. The samples were sequenced to an average depth of 40,000-60,000 reads on an Illumina HiSeq 4000 sequencer.

Microglial single cell sequencing (Figure 2): Approximately 15,000 cells were loaded into each well of Chromium Chip B (v3, figure 3), libraries were prepared in-house as described in the 10x Manual, and sequenced on one lane of the NovaSeq S4 at the Chan-Zuckerberg BioHub.

Single cell data analysis: Sequenced samples were processed using the Cell Ranger 2.1 pipeline (built on the STAR aligner)(Dobin et al., 2013) and aligned to the GRCm38 (mm10) mouse reference genome. Clustering and differential expression analysis were conducted using Seurat version 3.1.4. Data for figures 1 and 2 (total glial population) and figure 3 (microglia only) were prepared on different versions of the 10x Chromium platform and were therefore analyzed separately as detailed below. Sequencing scripts can be found at https://github.com/lcdorman/IFNresponseCode, and original data can be found on GEO at GSE173173. (**Table 4.5**).

Table 4.5: Single cell sequencing parameters

	Whole Glial Isolation	**Microglial Isolation**
Number of cells (thresholded)	1777 cells; 357 astrocytes	12,330 microglia
Figures	1, S2-S3	2-4, S4, S9
Age	Postnatal day 7	Postnatal days 5 and 7
Biological Replicates (mice)	1 Male + 1 Female	P5: 3 Male + 3 Female P7: 1 Male + 3 Female
Lanes	2 (Control/Deprived, 2 mice pooled)	4 (P5 Control/Deprived, 6 mice pooled; P7 Control/Deprived, 4 mice pooled)
10x Chromium Kit	Chip A/V2	Chip B/V3
Feature thresholds	400-5000 genes/cell	2500-7500 genes/cell
% Mitochondrial RNA thresholds	0-5% mitochondrial RNA/cell	0-7.5% mitochondrial RNA/cell
Normalization	SCTransform	Log normalization/scale factor 10,000
Minimum % of cells expressing gene for diff. exp. Analysis	5%	10%
Clustering resolution (Seurat)	1.2 (clusters); 0.1 (cell types); 0.6 (astrocytes)	0.5

Sorted cells were sequenced using the 10x Chromium kit. Following alignment in Cell Ranger as described above, counts were imported into R and analyzed using the Seurat package (Butler et al., 2018; Macosko et al., 2015). Cells outside of the thresholds listed in the table were excluded from downstream analysis. Cells were identified as "female" or "male" based on their expression of the gene *Xist*; any cells expressing at least one count of *Xist* were labelled female, while all others were labelled male. Counts were then normalized, regressing out percent mitochondrial RNA and total counts per cell. The top 6000 most variable genes were used to calculate 50 principal components, and the top 30 PCs were used for nearest neighbor, UMAP, and cluster calculations with the resolutions shown in the table. Individual cell types were identified through calculation of marker genes using the Wilcox test for genes expressed in at least 50% of cells in the cluster and a natural log fold change of 1.2 or greater and adjusted p value less than 0.001.

For the cold protease experiment examining all non-neuronal cells (Fig.1) , the astrocyte cluster was isolated and reclustered based on the top astrocyte and microglial genes to remove 5 cells which showed high expression of microglial marker genes and separate the cells into three clusters. The remaining astrocytes were re-normalized and analyzed with the Variance Partition package (Hoffman and Schadt, 2016) in R to determine the top 1,000 genes altered by condition. Differential expression analysis using Seurat's MAST function was then conducted using these genes between the control-enriched and deprived-enriched clusters. Volcano plots were generated using the EnhancedVolcano package in R, with gene labels chosen from the top differentially expressed genes. Cutoffs were set at natural log fold change greater than 0.25 (28% increase) and adjusted p-value smaller than 10^{-3}.

For the microglia only experiment (Fig. 2-on) , the microglial and macrophage clusters were isolated based on expression of Cx3cr1, Fcrls, P2y12, and low expression of non-microglial genes as shown in the heatmap. The filtered cells were re-normalized and analyzed with the Variance Partition package ((Hoffman and Schadt, 2016) in R to determine the top genes determining sex, the first 8 of which were excluded from downstream analysis. The top 6000 most variable genes were used to recalculate PCs, UMAP, and clusters. Clusters were determined using a resolution of 0.5, and the two sets of most closely related clusters (0/5 and 6/7) were combined due to low numbers of unique differentially expressed genes (log fold change >0.15, adjusted p-value < 10^{-5}). Clusters were combined either due to relatively low numbers of uniquely upregulated genes (<30 between clusters 6/7, 34 between clusters 0 and 5). The resultant and remaining clusters had equal or more unique DEGs and importantly were not more closely related to any other clusters with few unique DEGs. Differential gene expression between clusters were calculated using the MAST test in Seurat. The heatmaps shown only include genes expressed by at least 50% of the

cells in that cluster and with an adjusted p-value below 10^{-25}, sorted by highest log fold change. GO analysis was conducted using the Metascape webpage (www.metascape.org) (Zhou et al., 2019). Volcano plots were generated using the EnhancedVolcano package in R, with gene labels chosen from the top differentially expressed genes. Cutoffs were set at natural log fold change greater than 0.2 (22% increase) and adjusted p-value smaller than 10^{-25}.

Cell cycle phase assignment: Cells were assigned to S phase, G1 phase, or G2/M phase (not distinguished) using a previously published dataset (Kowalczyk et al., 2015) and the CellCycleScoring function in Seurat.

"Eigengene" calculations: DAM/PAM Subset-specific "Eigengenes" were calculated based on published differential gene expression signatures. All genes differentially expressed in a particular published subset with LFC > 1.5 and adj. $p < 10^{-8}$ were combined and an expression value for this eigengene was calculated using the PercentageFeatureSet function in Seurat, which calculates a percent expression per cell for any gene set. Ribosomal genes, which are expressed by all the clusters, were excluded from the analysis to avoid biasing the eigengene towards these highly expressed genes. Eigengene expression was validated by randomly sampling sets of 10 genes from the eigengene; every random sample showed the same gene expression pattern in the clustered data set as the full gene set, ensuring that a few genes were not biasing the entire eigengene. The "Neuronal Eigengene" was calculated using a published cell-specific RNA sequencing database(Zhang et al., 2014). Fold enrichment by cell type (neurons, oligo lineage, astrocytes, microglia, endothelial cells) was calculated for each of the genes enriched in cluster 3 (MAST DE analysis, adj. p<1e-10, natural log fold change > 0.25). Fold enrichment by cell type was defined as the highest FPKM divided by the next highest FPKM for each gene, resulting in a cell type assignment and enrichment score. Only genes with an enrichment score greater than 3 for

Neurons were included in the Neuronal eigengene calculation (45 genes). The normalized expression values for these 45 neuronal-specific genes were summed on a per-cell basis to create a violin plot showing overall neuronal gene expression per cluster.

RNA Velocity analysis: Spliced and unspliced transcript counts were calculated using Velocyto 0.17 and the velocyto run10x command with default settings. UMAP cell embeddings and annotation were exported from Seurat and used to plot all data shown. ScVelo 2.0.0 was run in Python and trajectories were calculated for all cells, then for each sample individually (Bergen et al., 2020; La Manno et al., 2018).

Bar plot creation: Bar plots were created using ggplot2 in R. Coding details available on github (https://github.com/lcdorman/IFNresponseCode/blob/main/Code%20for%20paper/P5_P7%20Microglia/D_BarPlots.Rmd). A table was made of cells per cluster per sample. Cell numbers were normalized by sample by dividing each entry by the total number of cells for that sample and multiplying by 2,000. Percents per cluster were then calculated by dividing the normalized cell numbers by the total number of cells in that cluster and multiplying by 100. Statistics were calculated individually for each cluster using a Chi-Square test on the raw cell numbers per cluster and sample. Plots with multiple bars had an additional Bonferroni correction applied, which multiplies the p-value by the number of comparisons.

Atac-seq and microglial enrichment integration: "Microglial specificity" values were calculated using a published bulk sequencing dataset from developing mouse cortex(Zhang et al., 2014). FPKM values per gene in microglia were divided by the average FPKM for that gene in all other cell types to find a "Specificity score". A specificity score of 10 or higher was considered "Microglial specific" for the purposes of this study. An unpublished Atac-seq study of bulk

microglia from adult mouse cortex was used to identify open chromatin promoter peaks for each gene. Peaks were called using Homer. Homer's "Peak Score" output was used to call peaks, which measures the position-adjusted number of reads identified for a particular promoter region. Only promoter peaks were considered, and if multiple promoter peaks were found for a single gene, only the one with the highest score was used. A promoter peak was only considered present if at least two of four samples had a peak score greater than 15. The minimum detectable peak had a value of 5, while the maximum detected was 5,000.

qPCR: To extract RNA from cells isolated by FACS, freshly sorted cells were pelleted at 500 g for 10 minutes at 4° and then resuspended in RLT Plus buffer (Qiagen). Cells were vortexed and frozen for at least one day at -80° before being thawed on ice and processed for RNA using a Rneasy Mini Kit (Qiagen). Purified mRNA was converted to cDNA with the High Capacity cDNA Reverse Transcription kit (Life Technologies) and amplified using either the Fast SYBR Green Master Mix (Thermo Fisher) or TaqMan Gene Expression Master Mix (Thermo Fisher) and a 7900HT Fast Real-Time PCR System (Applied Biosystems).

SARS-CoV-2 virus propagation and plaque assay: All SARS-CoV-2 cell culture and animals works were performed in the Biosafety level 3(BSL3). African green monkey kidney Vero-E6 cell line (ATCC#1586) and Calu-3 cells(ATCC# HTB-55) was obtained from American Type Culture Collection and maintained in Minimum Essential Medium (MEM, Gibco Invitrogen) supplemented with 10% fetal bovine serum (FBS, Gibco Invitrogen), 1% Penicillin-Streptomycin-Glutamine (Gibco Invitrogen) at 37 °C in a humidified 5% CO2 incubator. A clinical isolate of SARS-CoV-2 from a UCSF patient was propagated in Vero E6 cells and Calu-3 cells. 80%

Confluent monolayers of Vero E6 cells grown in 6-well plates were incubated with the serial dilutions of virus samples (250 µl/well) at 37 °C for 1 hour. Next, the cells were overlaid with 1% agarose (Invitrogen) prepared with MEM supplemented containing 2% fetal bovine serum(sigma), 1x penicillin/streptomycin/glutamine (100xPSG, Gibco). Three days later, the cells were fixed with 4% formaldehyde (PFA) for 2 hours, the overlay was discarded and samples were stained with cresyl violet dye.

SARS-CoV-2 infection: 5-6 weeks old Hemizygous K18-hACE2 mice (The Jackson laboratory, https://www.jax.org/strain/034860, stock number: 034860, B6.Cg-Tg(K18-ACE2)2Prlmn/J) were anesthetized with isoflurane and inoculated with $6x10^4$ PFU of SARS-CoV-2 intranasally in a BSL3 facility. The mice were sacrificed at 3 and 6 days post- infection, and the brain was removed and fixed in 4% PFA for 72 hours before being sunk in 30% sucrose and embedded in OCT. 40 µm sections were cut on a cryostat and stained as described above with 2 minute antigen retrieval at 95 degrees. Antibodies used include the following: rabbit anti-SARS-CoV-2 Nucleocapsid(N) (GeneTex, GTX135361), mouse anti-SARS-CoV-2-spike(S), (GeneTex, GTX632604).

Microglia CD68 volume: Z-stacks were collected on an LSM 880 confocal microscope with AiryScan (Zeiss) on Super resolution mode and a 63x objective (NA 1.4). Laser power and gain were consistent across each image. AiryScan processing was performed in Zen software (Zeiss) at a setting of 6 (‘‘optimal’’ setting). Images were analyzed using Imaris software (Bitplane) by creating a 3D surface rendering of individual microglia, thresholded to ensure microglia processes were accurately reconstructed, and maintained consistent thereafter. Microglia rendering was used

to mask and render the CD68 channel within each microglia. CD68 volume per microglia was then calculated as the total volume of masked CD68 volume within the masked GFP volume.

Microglia phagocytic compartment analyses: Phagocytic compartments, including phagocytic cups, phagosomes, and phagolysosomes, were identified as DAPI-enveloping structures that are distinct from the microglia nuclei. Unlike the microglia nuclear compartment, phagosomes lacked staining for Iba1 or GFP. Phagocytic cups lacked CD68 and only partially enveloped a DAPI+ and non-pyknotic cell. For experiments in 5xFAD animals, phagocytic cups were identified as Iba1 deficient organelles at the terminal ends of microglia processes. Microglia with bubble morphology were identified by enlarged and rounded phagosomes or phagolysosomes that were larger than the microglia nucleus. These phagocytic compartments contained DAPI+ nuclear material undergoing pyknosis or karyorrhexis, which were very sparsely distributed within the phagosome. In contrast, non-bubble phagosomes tightly enveloped engulfed nuclear material such that the DAPI signal saturated the phagosome area.

Z-stacks were acquired using an LSM 880 confocal microscope with AiryScan (Zeiss) on Super resolution mode and a 63x objective (NA 1.4, 0.04 μm pixel size, 16-bit depth) and processed as described above. Phagocytic compartments were analyzed in ImageJ and ROI's were drawn around phagosomes using the Versatile Wand Tool plugin. The "tolerance" setting was manually adjusted to envelop the microglia phagocytic compartment surface and "connectedness" was set to 8-connected. An optical section was selected from the z-stack that represented the center of the compartment and mean intensity, integrated density, and area were then recorded for each phagocytic compartment.

For analysis of phagocytic compartments in Sars-CoV-2 infected mice, images were first binned by average IFITM3 MFI per microglia. The maximum microglial IFITM3 mean fluorescence intensity per image across all samples was called 100%. The lower bin represents images with 0-50% of the maximum expression, and the higher bin represents images with 50-100% of the maximum expression. Each microglia was then manually scored for presence or absence of a phagocytic compartment as described above. For experiments in 5xFAD mice determining microglia association with plaques, microglia that were within 10 μm of an Aβ plaque was considered plaque-associated.

Lysotracker analysis: Mice were perfused with ice-cold PBS and cut into 200 μm coronal sections on a vibratome in a supplemented media (HBSS, 15 mM HEPES, 0.6% glucose, 1 mM EDTA pH 8.0). Sections containing the barrel cortex were incubated with Lysotracker Red at 1:5000 for 10 minutes, then washed and fixed overnight in 4% PFA before staining and mounting. 15 μm z-stacks were acquired on a LSM800 and analyzed in Fiji.

Interferon-β injection: A solution of 10 ng Interferon-β (IFN-β, R&D Systems, 8234-MB-010) diluted in 2 μl of aqueous solution containing 1mM of the indicator dye PsVue-550 (Molecular Targeting, P-1005, prepared according to the manufacturer's directions) was injected into the right lateral ventricle of P4 C57/Bl6J mice (coordinates: x = 1, y=1.8, z = -2, in reference to lambda). Control mice were injected with an equal volume PsVue-containing vehicle. The mice were perfused 24 hours later with ice-cold PBS and PFA, post-fixed in 4% paraformaldehyde overnight at 4°C, cryoprotected and sectioned on a cryostat at 50 μm (floating sections, used for IFITM3 quantification) and 20 μm (slide-mounted sections, used for 53BP1 foci quantification). Images

were acquired using the 40x objective of an LSM 800 (Zeiss) and counted using the Cell Counter tool in Fiji. 53BP1 quantification was conducted on primary and secondary motor cortex Layer 2/3 within 500 μm laterally to the injection track.

Poly(I:C) microinjection into zebrafish larvae: For poly(I:C) injection, 7 dpf *Tg(mpeg:EGFP-CAAX);Tg(NBT:dsRed)* zebrafish larvae were anesthetized with 0.2 mg/ml of tricaine in embryo medium. Larvae were injected with 2 nl of 1 mg/ml poly(I:C) (Invitrogen) or PBS as a vehicle control into the optic tectal ventricle by microinjection. Zebrafish larvae were transferred to fresh embryo medium after injection for recovery and imaged at 4 hrs post injection. We carefully monitored the larvae after injection to confirm that they recovered from anesthesia and did not exhibit abnormal swimming behaviors. Only healthy post-injection larvae were used for live imaging.

Live imaging: For live imaging, *Tg(mpeg:EGFP-CAAX);Tg(NBT:dsRed)* zebrafish larvae were anesthetized with 0.2 mg/ml of tricaine in embryo medium and mounted in 1.2% low-melting agarose gel on a glass bottom 35-mm dish (MatTek) and covered with embryo water containing 0.2 mg/ml tricaine. Time-lapse image was performed on a Nikon CSU-W1 spinning disk/high speed widefield microscope. We took time-lapse images from the optic tectum collecting 40-60 μm z-stacks (step size: 0.5 μm) at 5 min intervals for 30 min-1 hr. The images were processed by ImageJ software. For analysis, we calculated the number of DsRed(+) neurons in microglia for the first 30 min of each video. For the analysis of process motility, we carefully observed each microglia process for the first 30 min of each video and classified all processes into three categories: 1) 'ramified' were defined as processes with or without movement that have no

phagocytic cup formation, 2) ‘cup formation’ denoted processes with or without movement that contained or formed phagocytic cups, and 3) ‘soma retraction’ — processes that enclosed DsRed+ cells that were subsequently trafficked toward the microglial soma). Statistical analyses were performed by GraphPad Prism software.

QUANTIFICATION AND STATISTICAL ANALYSIS

GraphPad Prism 9.3.1 was used for most statistical analyses of imaging data, and the Seurat package V3 in R was used for statistical analysis of single cell data. Statistical tests are as described in text and figure legends. Violin plots were used for data with $n > 20$ to better visualize the distribution of individual data points. Single cell RNA-sequencing data was analyzed in R as described in the methods section above. Categorical data shown in bar plots (cluster-specific differences in cell numbers) were analyzed in R using a Chi-Square test on each cluster with Bonferroni’s correction for multiple comparisons.

Table 4.6: Resources and key reagents

Antibodies-immunostaining
rabbit anti-DsRed 1:1000 (Clontech, 632496)
Rat anti-mCherry 1:1000 (Invitrogen, M11217)
chicken anti-GFP 1:1000 (Aves Labs, 1020)
chicken anti-NeuN1:400 (Millipore, ABN91)
rabbit anti-Iba1 1:1000 (Wako Chemicals, 019-19741)
Mouse anti-Iba1 1:1000 (Wako Chemicals, 016-26721)
Guinea pig anti-Iba1 1:2000 (Synaptic Systems, 234-004)
Rat anti-P2ry12 1:100 (Biolegend, 848001)
rabbit anti-P2y12 1:500 (David Julius Lab)
rat anti-GFAP 1:1000 (Thermo Fisher, 13-0300)
Rabbit anti-IFITM3 1:1:1000 (Thermo Fisher, 11714-1-AP)
guinea pig anti-VGLUT2 1:2000 (Synaptic Systems, 135404)
rat anti-CD68 1:500 (BioRad, MCA1957GA)
Goat anti-rabbit IgG, HRP-linked (Cell Signaling Technology, 7074P2)
Hoechst 33342 solution 1:5000 (Thermo Fisher, 62249) was used for nuclear labeling
Mouse anti-Amyloid-Beta (4G8) 1:1000 (BioLegend, 800708)
rabbit anti-SARS-CoV-2-N protein 1:1000 (GeneTex, GTX135361)
mouse anti-SARS-CoV-2-Spike 1:1000 (GeneTex, GTX632604)
Rat anti-Bst2/Tetherin (R&D Systems, MAB8660-SP)
Mouse anti-γ-H2AX (EMD Millipore, 05-636)
Rabbit anti-53BP1 (Novus Biologicals, NB100-304)
Rabbit anti-cleaved caspase 3 1:1000 (BD Biosciences, 559565)
Goat Secondaries 1:500 (a-Rb, GP, Ck, Rat, Ms; 555, 488, 647) (Life Technologies)
Antibodies — flow cytometry
TruStain rat anti-CD16/32 1:100 (BioLegend, 101319)
APC rat anti-CD11b 1:100 (BioLegend, 101212)
PE rat anti-CD11b 1:100 (eBioscience, 12-0112-81)
FITC rat anti-CD45 1:100 (BioLegend, 103108)
Rabbit anti-IFITM3 1:1:1000 (Thermo Fisher, 11714-1-AP)
Goat anti-Rb 647 1:500 (Life Technologies A-21244)

Critical Commercial Assays	**Source**	**Cat #**
RNAscope Multiplex Fluorescent Reagent Kit v1 assay, Mouse *Htra1* RNAscope Probe; RNAscope Multiplex Fluorescent Reagent Kit v2 assay, Mouse *Grin1* RNAscope probe, Mouse *Rbfox3* RNAscope probe	Advanced Cell Diagnostics	320851, 423711-C2, 323100, 431611, 313311-C2
DeadEnd Fluorometric TUNEL system	Promega	G3250
Lysotracker Red	ThermoFisher	L7528
TSA Plus Cyanine 3, Cyanine 5, and Fluorescein detection kits	Akoya Biosciences	NEL744001KT, NEL745001KT NEL701A001KT

Critical Commercial Assays	**Source**	**Cat #**
Chromium single cell gene expression platform, version 2 (Whole-glia RNAseq, Figure 1)	10x Genomics	Library and gel bead kit — V2, 120267 Chip A kit: 1000009
Chromium single cell gene expression platform, version 3 (Microglial RNAseq, Figures 2+)	10x Genomics	Library and gel bead kit – V3, 1000075 Chip B kit: 1000074
Summary of Deposited Data		
Single cell RNA-sequencing of glial from postnatal day 7 barrel cortex after unilateral whisker follicle cauterization at postnatal day 2	Gene Expression Omnibus	**GSE173173**
Single cell RNA-sequencing of microglia from postnatal day 5 and 7 barrel cortex after unilateral whisker follicle cauterization at postnatal day 2	Gene Expression Omnibus	**GSE173173**
Experimental Models: Model organisms		
Cx3cr1-GFP	JAX #00582	(Jung et al., 2002)
Aldh1l1-eGFP	GENSAT MGI:3843271	(Gong et al., 2003)
Ifnar1-/-	JAX #028288	(Prigge et al., 2015)
Mx1-GFP	JAX #033219	(Uccellini and García-Sastre, 2018)
Mx1-Cre	JAX #003556	[JAX]
Ai14	JAX #007908	(Madisen et al., 2010)
B6.Cg-Tg(K18-ACE2)2Prlmn/J	JAX #034860	(McCray et al., 2007)
B6SJL-Tg(APPSwFlLon,PSEN1*M146L*L286V)6799Vas/Mmjax (5xFAD)	JAX #34840-Jax	(Oakley et al., 2006)
Aldh1l1-tdTomato	MMRRC, RRID:MMRRC_036700-UCD	
Rorb-Ires2-Cre-D	Jax **023526**	
Tg(mpeg:EGFP-CAAX)	ZFIN ID: ZDB-TGCONSTRCT-191211-1	
Tg(NBT:dsRed)	ZFIN ID: ZDB-TGCONSTRCT-081023-2	

Chapter 5: Conclusion and Future Directions

Conclusions

This dissertation represents the combined interdisciplinary work of more than 20 scientists. It is for that reason that we were able to draw conclusions about the structure and function of microglia in a wide variety of contexts. By combining expertise in immunohistochemistry, microscopy, flow cytometry, mouse and zebrafish genetics, and bioinformatics, we were able to generate hypotheses about molecular mechanisms of microglial function and validate them *in situ* in multiple model organisms. In this conclusion I will summarize our findings, present some lessons learned about experimental design of single cell sequencing experiments, and conclude with ideas for future research based on this work.

Microglia have long been known to have a diversity of functions; this work highlights the diversity of gene expression profiles that characterize even microglia ostensibly carrying out similar functions. In this work we show multiple different transcriptomic states for phagocytic microglia in particular environmental contexts. In the context of a developing brain during a wave of neurogenesis, phagocytic microglia in the zebrafish Optic Tectum express a signature including lysosomally active cathepsin proteases, *apoeb*, and galectins. Nearby microglia in the synapse-rich hindbrain, which engulf synapses or synaptic debris, instead express genes associated with opsonization and antigen presentation including members of the complement pathway and the major histocompatibility complex (MHC) class II gene *cd74b*. Adult zebrafish brains also contained lysosomally active microglia expressing inflammasome genes, which can lead to immune activation following apoptotic cell clearance (Boada-romero et al., 2020). This work allowed us to transcriptomically characterize distinct microglial functional states, providing a basis

for future hypothesis-driven work investigating how specific gene expression changes determine microglial morphology and function in different environments.

The mammalian brain does not exhibit this same degree of spatial segregation of microglial functions. This makes it more difficult to identify distinct functional populations in the naive brain due to the dynamic and often transient nature of microglial states. Therefore, we designed an experiment with a developmental perturbation to induce a robust microglial response to widespread topographic remapping in the somatosensory cortex of the mouse brain. We identified a transient population of interferon-responsive microglia that were highly phagocytic with the ability to engulf multiple cells simultaneously. This microglial state is functionally, regionally, and transcriptomically distinct from yet another phagocytic cell population referenced in chapter 2, which is found in the developing corpus callosum and engulfs oligodendrocytes (Hammond et al., 2019; Li et al., 2019a). Type I interferon-responsive microglia engulf neurons within the grey matter and limit the accumulation of stressed neurons. This is the first study to identify interferon-responsive microglia during physiological development and to characterize the functional significance of this pathway in promoting effective phagocytosis. Beyond their important role in development, this study and others have observed a similar transcriptomic signature under pathological conditions (Friedman et al., 2018) suggesting that these microglia are likely influential in disease progression as well. Finally, this microglial state is distinct from damage associated microglia (DAMs) (Keren-Shaul et al., 2017), which share more in common with the white-matter associated microglia mentioned above. This work brings us a step closer to a full understanding of how microglia are shaped by and in turn sculpt their neural environment.

Lessons in single cell sequencing experimental design

Chapters 3 and 4 represent entire stories combining sequencing with diverse other techniques to functionally define multiple populations. In both of these cases, the sequencing experiments had interpretable and useful results because of specific choices made during the experimental design phase. In chapter 3, we used bulk microglial sequencing to identify region-specific signatures within the zebrafish brain. We then overlaid this regional metadata on our whole-brain single cell sequencing microglial dataset to annotate the independently identified clusters. This analysis validated that these regionally diverse populations were in fact transcriptomically distinguishable and allowed the *in silico* removal of macrophage contamination to specifically characterize unique microglial populations. In the neonatal murine microglial sequencing, we purposefully started with a developmental perturbation – partial whisker cauterization – in order to elicit a microglial response to a strong stimulus, knowing that previous ground-state microglial sequencing often showed little heterogeneity despite the many known roles of microglia in the developing brain. In each case, careful experimental design allowed the collection of high-quality interpretable sequencing data.

Most importantly, it was crucial in each case to start with a carefully defined scientific question that could best be answered through single-cell sequencing. In one case, we used a developmental perturbation where we expected a heterogeneous microglial response that would not be fully captured by bulk sequencing. The use of a widespread perturbation and specific isolation of the cell type we were interested in, in the area of the brain we expected to be affected, allowed us to observe a shift in cell profiles that otherwise could have been hidden. In the other case, we were specifically interested in microglial heterogeneity within the zebrafish brain which could not be fully captured by sorting-based isolation techniques and bulk sequencing. Importantly, we had

prior evidence showing that this heterogeneity existed at the age and in the regions we were interested in and were able to use that evidence as metadata to annotate and further understand the resulting single-cell sequencing dataset.

After defining the question, isolating a robust population of healthy, intact cells is the key to obtaining high quality sequencing data. As technology improves the necessary cell numbers will likely fall, but we found overall that only 1/4 of the cells loaded in any given experiment will survive through sequencing and quality control. Therefore, it is necessary to ensure through adequate pilot experiments that the cells isolated are healthy and enriched for the population of interest. It is important to carefully consider how to mitigate any potential artifacts introduced during tissue preparation, dissociation, and cell isolation. During each of these steps, differences in timing, temperature, enzymes used, oxygenation, and stress on cells (i.e. through sorting) can alter the transcriptional profile and health of the cells. Any of these alterations can result in overall changes in gene expression that mask important variations in physiological cell states.

Replication, and avoiding pseudoreplication bias, is a big issue with expensive single-cell sequencing experiments (Zimmerman et al., 2021). Ideally, experimental design would ensure multiple biological and technical replicates for each experimental condition; however, this can be cost-prohibitive. While this field will continue to evolve, we addressed this issue by including multiple male and female biological replicates within a single lane, which could later be distinguished *in silico* based on expression of female- and male- specific genes. If this is not possible, for example in our zebrafish experiments, we instead included two lanes per condition to ensure separable biological and technical replicates.

In short, the key to a good single cell sequencing experiment, in my experience, is to ensure that this hypothesis-generating approach is not just a fishing expedition but instead has carefully designed parameters to maximize the changes of success.

Future Directions

Single-cell sequencing is by nature a hypothesis-generating technique, and while the works presented here have combined sequencing with a variety of techniques to reach functional and mechanistic conclusions, we hope that these conclusions will open the door to a variety of novel questions. In chapter 3, we found intriguing new gene candidates in zebrafish microglia that appear likely to play a role in determining whether those cells phagocytose whole cells (galectins and cathepsins) or synaptic material/ECM (*lygl1, cebpb, grn1, cd74b*). We don't currently know what signals regulate the maintenance of these populations, and how quickly (or at all) a microglia can transition between the states we identified. We also found an adult population of microglia with inflammasome marker expression that did not appear in the developing fish. Inflammasome activation can result in the release of cytokines and further immune activation, which could potentially result in more cell death (Boada-romero et al., 2020). It is unclear why we only found these microglia in the adult brain, or whether they are helpful or harmful in health and disease; it is possible that immature microglia are not competent to express inflammasome genes, or there may be signals in the adult and aging brain that promote these signals.

We then moved to the mouse brain and characterized the glial response to a developmental stressor that causes topographic remapping of thalamocortical inputs in the neonatal somatosensory cortex. We found that this perturbation expanded an existing type I interferon-responsive microglial population with an increased capacity for phagocytosis. Blocking type I

interferon signaling resulted in an accumulation of neurons with DNA damage and concomitant decrease in dead cells, suggesting that these microglia selectively and efficiently kill and engulf stressed neurons in a process called phagoptosis (Brown and Neher, 2012). This work raises many fascinating questions. We don't yet know what the timescale of microglial phagocytosis is and how it is altered by interferon activation. Answering this question would assist in designing experiments to probe this response. Data not shown here suggests that murine microglia take over 6 hours to respond with detectable levels of IFITM3 after direct injection of IFN-β, while zebrafish microglia were observed to engulf more cells within 4 hours of poly(I:C) injection. Meanwhile, recent research in cultured macrophages suggests a timescale of phagosome maturation in which phagosomes fuse with lysosomes in 1-2 hours, and lysosomes take ~6 hours to resolve and re-form (Lancaster et al., 2021). Within this six hour time window, the phagocytic capacity of the cell is decreased.

Our work suggests that interferon activation may decrease the latency between a microglia engulfing its first, second, and third cells, perhaps by speeding up the process of phagosome resolution. This would also explain why IFNAR1$^{-/-}$ microglia had enlarged lysosomes, if they could not be properly broken down and recycled. This idea is supported by prior work showing that IFITM proteins help stabilize v-ATPases and consequently clathrin in endosomal membranes. This stabilization enables fusion of different endosomal compartments, which is a necessary step in the breakdown of apoptotic cell bodies within microglia (Peri and Nüsslein-Volhard, 2008; Wee et al., 2012).

It will also be important to investigate how interferon production is triggered, and which cells are actually making it; how or if microglia know to target particular cells, especially if they themselves are the source of the interferon; what the effects of interferon signaling deficits are

later in life, both acutely and chronically; and how these cells fit into the TREM2-APOE axis discovered to play a role in neurodegeneration (Krasemann et al., 2017; Lee et al., 2021b). It is likely that this cell state is distinct from TREM2-activated microglia, based on multiple single cell sequencing datasets including those presented here (Friedman et al., 2018), but it is unclear how they differ functionally both during development (where they may be restricted to particular regions of the brain, white matter vs grey matter) and in aging and disease (Hammond et al., 2019; Li et al., 2019a).

An important outstanding question in microglial biology is how to separate the harmful and productive effects of microglia in contexts of extensive neuronal damage and death, including in stroke, infection, and neurodegeneration. Gaining a better understanding of the mechanisms of diverse forms of microglial phagocytosis and the signaling cascades that mediate these responses will allow researchers to target particular forms of microglial activity while sparing others. In essence, dissecting these pathways may grant us scalpels where we currently have only hammers.

References

Adam, M., Potter, A.S., and Potter, S.S. (2017). Psychrophilic proteases dramatically reduce single-cell RNA-seq artifacts: A molecular atlas of kidney development. Dev.

Allen, N.J., and Lyons, D.A. (2018). Glia as architects of central nervous system formation and function. Science (80-.).

Anders, S., Pyl, P.T., and Huber, W. (2015). HTSeq-A Python framework to work with high-throughput sequencing data. Bioinformatics.

Arguello, P.A., and Gogos, J.A. (2012). Genetic and cognitive windows into circuit mechanisms of psychiatric disease. Trends Neurosci. *35*, 3–13.

Ayata, P., Badimon, A., Strasburger, H.J., Duff, M.K., Montgomery, S.E., Loh, Y.H.E., Ebert, A., Pimenova, A.A., Ramirez, B.R., Chan, A.T., et al. (2018). Epigenetic regulation of brain region-specific microglia clearance activity. Nat. Neurosci. *21*, 1049–1060.

Badimon, A., Strasburger, H.J., Ayata, P., Chen, X., Nair, A., Ikegami, A., Hwang, P., Chan, A.T., Graves, S.M., Uweru, J.O., et al. (2020). Negative feedback control of neuronal activity by microglia. Nature.

Bailey, C.C., Zhong, G., Huang, I.C., and Farzan, M. (2014). IFITM-family proteins: The cell's first line of antiviral defense. Annu. Rev. Virol.

Baldi, A., Calia, E., Ciampini, A., Riccio, M., Vetuschi, A., Persico, A.M., and Keller, F. (2000). Deafferentation-induced apoptosis of neurons in thalamic somatosensory nuclei of the newborn rat: Critical period and rescue from cell death by peripherally applied neurotrophins. Eur. J. Neurosci.

Baruch, K., Deczkowska, A., David, E., Castellano, J.M., Miller, O., Kertser, A., Berkutzki, T., Barnett-Itzhaki, Z., Bezalel, D., Wyss-Coray, T., et al. (2014). Aging-induced type I interferon response at the choroid plexus negatively affects brain function. Science (80-.).

Bennett, M.L., Bennett, F.C., Liddelow, S.A., Ajami, B., Zamanian, J.L., Fernhoff, N.B., Mulinyawe, S.B., Bohlen, C.J., Adil, A., Tucker, A., et al. (2016). New tools for studying microglia in the mouse and human CNS. Proc. Natl. Acad. Sci. U. S. A. *113*, E1738–E1746.

Bergen, V., Lange, M., Peidli, S., Wolf, F.A., and Theis, F.J. (2020). Generalizing RNA velocity to transient cell states through dynamical modeling. Nat. Biotechnol.

Bitzenhofer, S.H., Pöpplau, J.A., Chini, M., Marquardt, A., and Hanganu-Opatz, I.L. (2021). A transient developmental increase in prefrontal activity alters network maturation and causes cognitive dysfunction in adult mice. Neuron.

Blanquie, O., Yang, J.W., Kilb, W., Sharopov, S., Sinning, A., and Luhmann, H.J. (2017). Electrical activity controls area-specific expression of neuronal apoptosis in the mouse developing cerebral cortex. Elife.

Boada-romero, E., Martinez, J., Heckmann, B.L., Green, D.R., Group, I., and Park, T. (2020). Mechanisms and physiology of the clearance of dead cells by efferocytosis. Nat. Rev. Cell Biol.

Bohlen, C.J., Bennett, F.C., and Bennett, M.L. (2019). Isolation and Culture of Microglia. Curr. Protoc. Immunol.

Boudinot, P., Langevin, C., Secombes, C.J., and Levraud, J.P. (2016). The Peculiar Characteristics of Fish Type I Interferons. Viruses 2016, Vol. 8, Page 298 *8*, 298.

Brass, A.L., Huang, I.C., Benita, Y., John, S.P., Krishnan, M.N., Feeley, E.M., Ryan, B.J., Weyer, J.L., van der Weyden, L., Fikrig, E., et al. (2009). The IFITM Proteins Mediate Cellular

Resistance to Influenza A H1N1 Virus, West Nile Virus, and Dengue Virus. Cell.

Brendecke, S.M., and Prinz, M. (2012). How type I interferons shape myeloid cell function in CNS autoimmunity. J. Leukoc. Biol. *92*, 479–488.

Brown, G.C., and Neher, J.J. (2012). Eaten alive! Cell death by primary phagocytosis: "Phagoptosis." Trends Biochem. Sci. *37*, 325–332.

Brown, G.C., and Neher, J.J. (2014). Microglial phagocytosis of live neurons. Nat. Rev. Neurosci. *15*, 209–216.

Butler, A., Hoffman, P., Smibert, P., Papalexi, E., and Satija, R. (2018). Integrating single-cell transcriptomic data across different conditions, technologies, and species. Nat. Biotechnol.

Butovsky, O., Jedrychowski, M.P., Moore, C.S., Cialic, R., Lanser, A.J., Gabriely, G., Koeglsperger, T., Dake, B., Wu, P.M., Doykan, C.E., et al. (2014). Identification of a unique TGF-β-dependent molecular and functional signature in microglia. Nat. Neurosci.

Cao, J., Spielmann, M., Qiu, X., Huang, X., Ibrahim, D.M., Hill, A.J., Zhang, F., Mundlos, S., Christiansen, L., Steemers, F.J., et al. (2019). The single-cell transcriptional landscape of mammalian organogenesis. Nature *566*, 496–502.

Carossino, M., Montanaro, P., O'Connell, A., Kenney, D., Gertje, H., Grosz, K., Kurnick, S., Bosmann, M., Saeed, M., Balasuriya, U., et al. (2021). Fatal neuroinvasion of SARS-CoV-2 in K18-hACE2 mice is partially dependent on hACE2 expression. BioRxiv.

Casano, A.M., Albert, M., and Peri, F. (2016). Developmental Apoptosis Mediates Entry and Positioning of Microglia in the Zebrafish Brain. Cell Rep. *16*, 897–906.

Chen, J., He, J., Ni, R., Yang, Q., Zhang, Y., and Luo, L. (2019). Cerebrovascular Injuries Induce Lymphatic Invasion into Brain Parenchyma to Guide Vascular Regeneration in Zebrafish.

Dev. Cell *49*, 697-710.e5.

Chen, J., Poskanzer, K.E., Freeman, M.R., and Monk, K.R. (2020). Live-imaging of astrocyte morphogenesis and function in zebrafish neural circuits. Nat. Neurosci. *23*, 1297–1306.

Chen, Q., Sun, L., and Chen, Z.J. (2016). Regulation and function of the cGAS-STING pathway of cytosolic DNA sensing. Nat. Immunol.

Chistiakov, D.A., Killingsworth, M.C., Myasoedova, V.A., Orekhov, A.N., and Bobryshev, Y. V. (2017). CD68/macrosialin: Not just a histochemical marker. Lab. Investig.

Chovatiya, R., and Medzhitov, R. (2014). Stress, inflammation, and defense of homeostasis. Mol. Cell *54*, 281–288.

Chris Bennett, F., Bennett, M.L., Gephart, H., Plowey, E.D., and Correspondence, B.A.B. (2018). A Combination of Ontogeny and CNS Environment Establishes Microglial Identity. Neuron *98*, 1170-1183.e8.

Colonna, M., and Butovsky, O. (2017). Microglia function in the central nervous system during health and neurodegeneration. Annu. Rev. Immunol. *35*, 441–468.

Cybulska-Klosowicz, A., Zakrzewska, R., Pyza, E., Kossut, M., and Schachner, M. (2004). Reduced plasticity of cortical whisker representation in adult tenascin-C-deficient mice after vibrissectomy. Eur. J. Neurosci.

Davalos, D., Grutzendler, J., Yang, G., Kim, J. V., Zuo, Y., Jung, S., Littman, D.R., Dustin, M.L., and Gan, W.B. (2005). ATP mediates rapid microglial response to local brain injury in vivo. Nat. Neurosci.

Deczkowska, A., Matcovitch-Natan, O., Tsitsou-Kampeli, A., Ben-Hamo, S., Dvir-Szternfeld, R., Spinrad, A., Singer, O., David, E., Winter, D.R., Smith, L.K., et al. (2017). Mef2C restrains

microglial inflammatory response and is lost in brain ageing in an IFN-I-dependent manner. Nat. Commun.

Diaz-Aparicio, I., Paris, I., Sierra-Torre, V., Plaza-Zabala, A., Rodríguez-Iglesias, N., Márquez-Ropero, M., Beccari, S., Huguet, P., Abiega, O., Alberdi, E., et al. (2020). Microglia Actively Remodel Adult Hippocampal Neurogenesis through the Phagocytosis Secretome. J. Neurosci. *40*, 1453–1482.

Dickey, J.S., Baird, B.J., Redon, C.E., Sokolov, M. V., Sedelnikova, O.A., and Bonner, W.M. (2009). Intercellular communication of cellular stress monitored by γ-H2AX induction. Carcinogenesis *30*, 1686–1695.

Dobin, A., Davis, C.A., Schlesinger, F., Drenkow, J., Zaleski, C., Jha, S., Batut, P., Chaisson, M., and Gingeras, T.R. (2013). STAR: Ultrafast universal RNA-seq aligner. Bioinformatics.

Ellett, F., Pase, L., Hayman, J.W., Andrianopoulos, A., and Lieschke, G.J. (2011). mpeg1 promoter transgenes direct macrophage-lineage expression in zebrafish. Blood *117*, e49–e56.

Erzurumlu, R.S., and Gaspar, P. (2012). Development and critical period plasticity of the barrel cortex. Eur. J. Neurosci.

Ferrero, G., Mahony, C.B., Dupuis, E., Yvernogeau, L., Di Ruggiero, E., Miserocchi, M., Caron, M., Robin, C., Traver, D., Bertrand, J.Y., et al. (2018). Embryonic Microglia Derive from Primitive Macrophages and Are Replaced by cmyb-Dependent Definitive Microglia in Zebrafish. Cell Rep. *24*, 130–141.

Ferris, H.A., Perry, R.J., Moreira, G. V., Shulman, G.I., Horton, J.D., and Kahn, C.R. (2017). Loss of astrocyte cholesterol synthesis disrupts neuronal function and alters whole-body metabolism. Proc. Natl. Acad. Sci. U. S. A.

Finak, G., McDavid, A., Yajima, M., Deng, J., Gersuk, V., Shalek, A.K., Slichter, C.K., Miller, H.W., McElrath, M.J., Prlic, M., et al. (2015). MAST: A flexible statistical framework for assessing transcriptional changes and characterizing heterogeneity in single-cell RNA sequencing data. Genome Biol.

Fleming, A., Diekmann, H., and Goldsmith, P. (2013). Functional Characterisation of the Maturation of the Blood-Brain Barrier in Larval Zebrafish. PLoS One *8*, e77548.

Fonseca, M.I., Chu, S.H., Hernandez, M.X., Fang, M.J., Modarresi, L., Selvan, P., MacGregor, G.R., and Tenner, A.J. (2017). Cell-specific deletion of C1qa identifies microglia as the dominant source of C1q in mouse brain. J. Neuroinflammation *14*, 1–15.

Forrest, M.P., Parnell, E., and Penzes, P. (2018). Dendritic structural plasticity and neuropsychiatric disease. Nat. Rev. Neurosci. *19*, 215–234.

Fourgeaud, L., Traves, P.G., Tufail, Y., Leal-Bailey, H., Lew, E.D., Burrola, P.G., Callaway, P., Zagorska, A., Rothlin, C. V., Nimmerjahn, A., et al. (2016a). TAM receptors regulate multiple features of microglial physiology. Nature *532*, 240–244.

Fourgeaud, L., Traves, P.G., Tufail, Y., Leal-Bailey, H., Lew, E.D., Burrola, P.G., Callaway, P., Zagorska, A., Rothlin, C. V., Nimmerjahn, A., et al. (2016b). TAM receptors regulate multiple features of microglial physiology. Nature *532*, 240–244.

Friedman, B.A., Srinivasan, K., Ayalon, G., Meilandt, W.J., Lin, H., Huntley, M.A., Cao, Y., Lee, S.H., Haddick, P.C.G., Ngu, H., et al. (2018). Diverse Brain Myeloid Expression Profiles Reveal Distinct Microglial Activation States and Aspects of Alzheimer's Disease Not Evident in Mouse Models. Cell Rep.

Frigerio, C.S., Wolfs, L., Fattorelli, N., Perry, V.H., Fiers, M., and De Strooper, B. (2019). The

Major Risk Factors for Alzheimer's Disease: Age, Sex, and Genes Modulate the Microglia Response to Aβ Plaques. Cell Rep. *27*, 1293–1306.

Frost, J.L., and Schafer, D.P. (2016). Microglia: Architects of the Developing Nervous System. Trends Cell Biol. *26*, 587–597.

Galatro, T.F., Vainchtein, I.D., Brouwer, N., Boddeke, E.W.G.M., and Eggen, B.J.L. (2017). Isolation of microglia and immune infiltrates from mouse and primate central nervous system. In Methods in Molecular Biology, p.

Galloway, D.A., Phillips, A.E.M., Owen, D.R.J., and Moore, C.S. (2019). Phagocytosis in the brain: Homeostasis and disease. Front. Immunol.

Geirsdottir, L., David, E., Keren-Shaul, H., Weiner, A., Bohlen, S.C., Neuber, J., Balic, A., Giladi, A., Sheban, F., Dutertre, C.A., et al. (2019). Cross-Species Single-Cell Analysis Reveals Divergence of the Primate Microglia Program. Cell.

Ginhoux, F., Greter, M., Leboeuf, M., Nandi, S., See, P., Gokhan, S., Mehler, M.F., Conway, S.J., Ng, L.G., Stanley, E.R., et al. (2010). Fate mapping analysis reveals that adult microglia derive from primitive macrophages. Science *330*, 841–845.

Gong, S., Zheng, C., Doughty, M.L., Losos, K., Didkovsky, N., Schambra, U.B., Nowak, N.J., Joyner, A., Leblanc, G., Hatten, M.E., et al. (2003). A gene expression atlas of the central nervous system based on bacterial artificial chromosomes. Nature.

Gosselin, D., Link, V.M., Romanoski, C.E., Fonseca, G.J., Eichenfield, D.Z., Spann, N.J., Stender, J.D., Chun, H.B., Garner, H., Geissmann, F., et al. (2014). Environment drives selection and function of enhancers controlling tissue-specific macrophage identities. Cell.

Gosselin, D., Skola, D., Coufal, N.G., Holtman, I.R., Schlachetzki, J.C.M., Sajti, E., Jaeger,

B.N., O'Connor, C., Fitzpatrick, C., Pasillas, M.P., et al. (2017). An environment-dependent transcriptional network specifies human microglia identity. Science (80-.).

Grau, S., Richards, P.J., Kerr, B., Hughes, C., Caterson, B., Williams, A.S., Junker, U., Jones, S.A., Clausen, T., and Ehrmann, M. (2006). The role of human HtrA1 in arthritic disease. J. Biol. Chem.

Grommes, C., Lee, C.Y.D., Wilkinson, B.L., Jiang, Q., Koenigsknecht-Talboo, J.L., Varnum, B., and Landreth, G.E. (2008). Regulation of microglial phagocytosis and inflammatory gene expression by Gas6 acting on the Axl/Mer family of tyrosine kinases. J. NeuroImmune Pharmacol. *3*, 130–140.

Gu, Z., Eils, R., and Schlesner, M. (2016). Complex heatmaps reveal patterns and correlations in multidimensional genomic data. Bioinformatics.

Gunner, G., Cheadle, L., Johnson, K.M., Ayata, P., Badimon, A., Mondo, E., Nagy, M.A., Liu, L., Bemiller, S.M., Kim, K.W., et al. (2019a). Sensory lesioning induces microglial synapse elimination via ADAM10 and fractalkine signaling. Nat. Neurosci.

Gunner, G., Cheadle, L., Johnson, K.M., Ayata, P., Badimon, A., Mondo, E., Nagy, M.A., Liu, L., Bemiller, S.M., Kim, K.W., et al. (2019b). Sensory lesioning induces microglial synapse elimination via ADAM10 and fractalkine signaling. Nat. Neurosci. *22*, 1075–1088.

Haghverdi, L., Lun, A.T.L., Morgan, M.D., and Marioni, J.C. (2018). Batch effects in single-cell RNA-sequencing data are corrected by matching mutual nearest neighbors. Nat. Biotechnol. *36*, 421–427.

Haimon, Z., Volaski, A., Orthgiess, J., Boura-Halfon, S., Varol, D., Shemer, A., Yona, S., Zuckerman, B., David, E., Chappell-Maor, L., et al. (2018). Re-evaluating microglia expression

profiles using RiboTag and cell isolation strategies. Nat. Immunol.

Hammond, T.R., Dufort, C., Dissing-Olesen, L., Giera, S., Young, A., Wysoker, A., Walker, A.J., Gergits, F., Segel, M., Nemesh, J., et al. (2019). Single-Cell RNA Sequencing of Microglia throughout the Mouse Lifespan and in the Injured Brain Reveals Complex Cell-State Changes. Immunity.

Han, R.T., Vainchtein, I.D., Schlachetzki, J.C.M., Cho, F.S., Dorman, L.C., Johung, T., Ahn, E., Barron, J.T., Nakao-Inoue, H., Joshi, A., et al. (2021). Interleukin-33 coordinates a microglial phagocytic response and limits corticothalamic excitability and seizure susceptibility. BioRxiv 2021.08.05.455250.

Hansen, D. V., Hanson, J.E., and Sheng, M. (2018). Microglia in Alzheimer's disease. J. Cell Biol.

Harris, J.A., Hirokawa, K.E., Sorensen, S.A., Gu, H., Mills, M., Ng, L.L., Bohn, P., Mortrud, M., Ouellette, B., Kidney, J., et al. (2014). Anatomical characterization of Cre driver mice for neural circuit mapping and manipulation. Front. Neural Circuits *8*, 76.

Hasel, P., Rose, I.V.L., Sadick, J.S., Kim, R.D., and Liddelow, S.A. (2021). Neuroinflammatory astrocyte subtypes in the mouse brain. Nat. Neurosci. 2021 2410 *24*, 1475–1487.

Herbomel, P., Thisse, B., and Thisse, C. (2001). Zebrafish early macrophages colonize cephalic mesenchyme and developing brain, retina, and epidermis through a M-CSF receptor-dependent invasive process. Dev. Biol. *238*, 274–288.

Hernández, P.P., Strzelecka, P.M., Athanasiadis, E.I., Hall, D., Robalo, A.F., Collins, C.M., Boudinot, P., Levraud, J.-P., and Cvejic, A. (2018). I N N A T E L Y M P H O I D C E L L S Single-cell transcriptional analysis reveals ILC-like cells in zebrafish.

Hoffman, G.E., and Schadt, E.E. (2016). variancePartition: Interpreting drivers of variation in complex gene expression studies. BMC Bioinformatics.

Hong, S., Beja-Glasser, V.F., Nfonoyim, B.M., Frouin, A., Li, S., Ramakrishnan, S., Merry, K.M., Shi, Q., Rosenthal, A., Barres, B.A., et al. (2016). Complement and microglia mediate early synapse loss in Alzheimer mouse models. Science (80-.).

Hoshiko, M., Arnoux, I., Avignone, E., Yamamoto, N., and Audinat, E. (2012). Deficiency of the Microglial Receptor CX3CR1 Impairs Postnatal Functional Development of Thalamocortical Synapses in the Barrel Cortex. J. Neurosci.

Van Hove, H., Martens, L., Scheyltjens, I., De Vlaminck, K., Pombo Antunes, A.R., De Prijck, S., Vandamme, N., De Schepper, S., Van Isterdael, G., Scott, C.L., et al. (2019). A single-cell atlas of mouse brain macrophages reveals unique transcriptional identities shaped by ontogeny and tissue environment. Nat. Neurosci. *22*, 1021–1035.

Huang, Y., Happonen, K.E., Burrola, P.G., O'Connor, C., Hah, N., Huang, L., Nimmerjahn, A., and Lemke, G. (2021). Microglia use TAM receptors to detect and engulf amyloid β plaques. Nat. Immunol. 1–9.

Hughes, A.N., and Appel, B. (2020). Microglia phagocytose myelin sheaths to modify developmental myelination. Nat. Neurosci. *23*, 1055–1066.

Hur, J.Y., Frost, G.R., Wu, X., Crump, C., Pan, S.J., Wong, E., Barros, M., Li, T., Nie, P., Zhai, Y., et al. (2020). The innate immunity protein IFITM3 modulates γ-secretase in Alzheimer's disease. Nature.

Imai, M., Iwatsuki-Horimoto, K., Hatta, M., Loeber, S., Halfmann, P.J., Nakajima, N., Watanabe, T., Ujie, M., Takahashi, K., Ito, M., et al. (2020). Syrian hamsters as a small animal

model for SARS-CoV-2 infection and countermeasure development. Proc. Natl. Acad. Sci. U. S. A. *117*, 16587–16595.

Ivashkiv, L.B., and Donlin, L.T. (2014). Regulation of type i interferon responses. Nat. Rev. Immunol.

Izquierdo, P., Shiina, H., Hirunpattarasilp, C., Gillis, G., and Attwell, D. (2021). Synapse development is regulated by microglial THIK-1 K+ channels. Proc. Natl. Acad. Sci. U. S. A. *118*.

Jeanmonod, D., Rice, F.L., and Van der Loos, H. (1981). Mouse somatosensory cortex: Alterations in the barrelfield following receptor injury at different early postnatal ages. Neuroscience.

Jung, S., Aliberti, J., Graemmel, P., Sunshine, M.J., Kreutzberg, G.W., Sher, A., and Littman, D.R. (2002). Analysis of Fractalkine Receptor CX3CR1 Function by Targeted Deletion and Green Fluorescent Protein Reporter Gene Insertion. Mol. Cell. Biol.

Kasheta, M., Painter, C.A., Moore, F.E., Lobbardi, R., Bryll, A., Freiman, E., Stachura, D., Rogers, A.B., Houvras, Y., Langenau, D.M., et al. (2017). Identification and characterization of T reg-like cells in zebrafish. J. Exp. Med. *214*, 3519–3530.

Kawai, T., and Akira, S. (2006). Innate immune recognition of viral infection. Nat. Immunol.

Kawai, H., Arata, N., and Nakayasu, H. (2001). Three-dimensional distribution of astrocytes in zebrafish spinal cord. Glia *36*, 406–413.

Keren-Shaul, H., Spinrad, A., Weiner, A., Matcovitch-Natan, O., Dvir-Szternfeld, R., Ulland, T.K., David, E., Baruch, K., Lara-Astaiso, D., Toth, B., et al. (2017). A Unique Microglia Type Associated with Restricting Development of Alzheimer's Disease. Cell *169*, 1276-1290.e17.

Korsunsky, I., Millard, N., Fan, J., Slowikowski, K., Zhang, F., Wei, K., Baglaenko, Y., Brenner, M., Loh, P. ru, and Raychaudhuri, S. (2019). Fast, sensitive and accurate integration of single-cell data with Harmony. Nat. Methods *16*, 1289–1296.

Kowalczyk, M.S., Tirosh, I., Heckl, D., Rao, T.N., Dixit, A., Haas, B.J., Schneider, R.K., Wagers, A.J., Ebert, B.L., and Regev, A. (2015). Single-cell RNA-seq reveals changes in cell cycle and differentiation programs upon aging of hematopoietic stem cells. Genome Res.

Kracht, L., Borggrewe, M., Eskandar, S., Brouwer, N., Chuva de Sousa Lopes, S.M., Laman, J.D., Scherjon, S.A., Prins, J.R., Kooistra, S.M., and Eggen, B.J.L. (2020). Human fetal microglia acquire homeostatic immune-sensing properties early in development. Science (80-.). *369*, 530–537.

Krasemann, S., Madore, C., Cialic, R., Baufeld, C., Calcagno, N., El Fatimy, R., Beckers, L., O'Loughlin, E., Xu, Y., Fanek, Z., et al. (2017). The TREM2-APOE Pathway Drives the Transcriptional Phenotype of Dysfunctional Microglia in Neurodegenerative Diseases. Immunity *47*, 566-581.e9.

Kumaran Satyanarayanan, S., El Kebir, D., Soboh, S., Butenko, S., Sekheri, M., Saadi, J., Peled, N., Assi, S., Othman, A., Schif-Zuck, S., et al. (2019). IFN-β is a macrophage-derived effector cytokine facilitating the resolution of bacterial inflammation. Nat. Commun. *10*, 1–16.

Kumari, P., Rothan, H.A., Natekar, J.P., Stone, S., Pathak, H., Strate, P.G., Arora, K., Brinton, M.A., and Kumar, M. (2021). Neuroinvasion and Encephalitis Following Intranasal Inoculation of SARS-CoV-2 in K18-hACE2 Mice. Viruses.

Lancaster, C.E., Fountain, A., Dayam, R.M., Somerville, E., Sheth, J., Jacobelli, V., Somerville, A., Terebiznik, M.R., and Botelho, R.J. (2021). Phagosome resolution regenerates lysosomes and

maintains the degradative capacity in phagocytes. J. Cell Biol. *220*.

Lavin, Y., Winter, D., Blecher-Gonen, R., David, E., Keren-Shaul, H., Merad, M., Jung, S., and Amit, I. (2014). Tissue-resident macrophage enhancer landscapes are shaped by the local microenvironment. Cell *159*, 1312–1326.

Lee, J., Robinson, M.E., Ma, N., Artadji, D., Ahmed, M.A., Xiao, G., Sadras, T., Deb, G., Winchester, J., Cosgun, K.N., et al. (2020). IFITM3 functions as a PIP3 scaffold to amplify PI3K signalling in B cells. Nature.

Lee, S.H., Meilandt, W.J., Xie, L., Gandham, V.D., Ngu, H., Barck, K.H., Rezzonico, M.G., Imperio, J., Lalehzadeh, G., Huntley, M.A., et al. (2021a). Trem2 restrains the enhancement of tau accumulation and neurodegeneration by β-amyloid pathology. Neuron *109*, 1283-1301.e6.

Lee, S.H., Meilandt, W.J., Xie, L., Gandham, V.D., Ngu, H., Barck, K.H., Rezzonico, M.G., Imperio, J., Lalehzadeh, G., Huntley, M.A., et al. (2021b). Trem2 restrains the enhancement of tau accumulation and neurodegeneration by β-amyloid pathology. Neuron *109*, 1283-1301.e6.

Lemke, G. (2013). Biology of the TAM Receptors. Cold Spring Harb. Perspect. Biol. *5*, a009076.

Lemke, G. (2019). How macrophages deal with death. Nat. Rev. Immunol. *19*, 539–549.

Li, Q., and Barres, B.A. (2018). Microglia and macrophages in brain homeostasis and disease. Nat. Rev. Immunol. *18*, 225–242.

Li, Q., Cheng, Z., Zhou, L., Darmanis, S., Neff, N.F., Okamoto, J., Gulati, G., Bennett, M.L., Sun, L.O., Clarke, L.E., et al. (2019a). Developmental Heterogeneity of Microglia and Brain Myeloid Cells Revealed by Deep Single-Cell RNA Sequencing. Neuron.

Li, X., Deng, M., Petrucelli, A.S., Zhu, C., Mo, J., Zhang, L., Tam, J.W., Ariel, P., Zhao, B.,

Zhang, S., et al. (2019b). Viral DNA Binding to NLRC3, an Inhibitory Nucleic Acid Sensor, Unleashes STING, a Cyclic Dinucleotide Receptor that Activates Type I Interferon. Immunity.

Li, Y., Du, X.F., Liu, C.S., Wen, Z.L., and Du, J.L. (2012). Reciprocal Regulation between Resting Microglial Dynamics and Neuronal Activity In Vivo. Dev. Cell *23*, 1189–1202.

Liberatore, R.A., and Bieniasz, P.D. (2011). Tetherin is a key effector of the antiretroviral activity of type I interferon in vitro and in vivo. Proc. Natl. Acad. Sci. U. S. A. *108*, 18097–18101.

Lin, M.K., Yang, J., Hsu, C.W., Gore, A., Bassuk, A.G., Brown, L.M., Colligan, R., Sengillo, J.D., Mahajan, V.B., and Tsang, S.H. (2018). HTRA1, an age-related macular degeneration protease, processes extracellular matrix proteins EFEMP1 and TSP1. Aging Cell.

Liu, X., Li, Y.-S., Shinton, S.A., Rhodes, J., Tang, L., Feng, H., Jette, C.A., Look, A.T., Hayakawa, K., and Hardy, R.R. (2017). Zebrafish B Cell Development without a Pre–B Cell Stage, Revealed by CD79 Fluorescence Reporter Transgenes. J. Immunol. *199*, 1706–1715.

Liu, Z., Condello, C., Schain, A., Harb, R., and Grutzendler, J. (2010). CX3CR1 in microglia regulates brain amyloid deposition through selective protofibrillar amyloid-β phagocytosis. J. Neurosci.

Van Der Loos, H., and Woolsey, T.A. (1973). Somatosensory cortex: Structural alterations following early injury to sense organs. Science (80-.).

Love, M.I., Huber, W., and Anders, S. (2014). Moderated estimation of fold change and dispersion for RNA-seq data with DESeq2. Genome Biol.

Lui, H., Zhang, J., Makinson, S.R., Cahill, M.K., Kelley, K.W., Huang, H.Y., Shang, Y., Oldham, M.C., Martens, L.H., Gao, F., et al. (2016). Progranulin Deficiency Promotes Circuit-

Specific Synaptic Pruning by Microglia via Complement Activation. Cell *165*, 921–935.

Lyons, D.A., and Talbot, W.S. (2014). Glial cell development and function in zebrafish. Cold Spring Harb. Perspect. Biol. *7*.

Macosko, E.Z., Basu, A., Satija, R., Nemesh, J., Shekhar, K., Goldman, M., Tirosh, I., Bialas, A.R., Kamitaki, N., Martersteck, E.M., et al. (2015). Highly Parallel Genome-wide Expression Profiling of Individual Cells Using Nanoliter Droplets. Cell.

Madabhushi, R., Gao, F., Pfenning, A.R., Pan, L., Yamakawa, S., Seo, J., Rueda, R., Phan, T.X., Yamakawa, H., Pao, P.C., et al. (2015). Activity-Induced DNA Breaks Govern the Expression of Neuronal Early-Response Genes. Cell *161*, 1592–1605.

Madisen, L., Zwingman, T.A., Sunkin, S.M., Oh, S.W., Zariwala, H.A., Gu, H., Ng, L.L., Palmiter, R.D., Hawrylycz, M.J., Jones, A.R., et al. (2010). A robust and high-throughput Cre reporting and characterization system for the whole mouse brain. Nat. Neurosci.

Mah, L.J., El-Osta, A., and Karagiannis, T.C. (2010). γH2AX: a sensitive molecular marker of DNA damage and repair. Leuk. 2010 244 *24*, 679–686.

Mangin, J.M., Li, P., Scafidi, J., and Gallo, V. (2012). Experience-dependent regulation of NG2 progenitors in the developing barrel cortex. Nat. Neurosci.

La Manno, G., Soldatov, R., Zeisel, A., Braun, E., Hochgerner, H., Petukhov, V., Lidschreiber, K., Kastriti, M.E., Lönnerberg, P., Furlan, A., et al. (2018). RNA velocity of single cells. Nature.

Marek, R., Caruso, M., Rostami, A., Grinspan, J.B., and Sarma, J. Das (2008). Magnetic cell sorting: A fast and effective method of concurrent isolation of high purity viable astrocytes and microglia from neonatal mouse brain tissue. J. Neurosci. Methods *175*, 108–118.

Marín-Teva, J.L., Dusart, I., Colin, C., Gervais, A., Van Rooijen, N., and Mallat, M. (2004).

Microglia Promote the Death of Developing Purkinje Cells. Neuron *41*, 535–547.

Márquez-Ropero, M., Benito, E., Plaza-Zabala, A., and Sierra, A. (2020). Microglial Corpse Clearance: Lessons From Macrophages. Front. Immunol. *11*, 506.

Masuda, T., Sankowski, R., Staszewski, O., Böttcher, C., Amann, L., Sagar, Scheiwe, C., Nessler, S., Kunz, P., van Loo, G., et al. (2019). Spatial and temporal heterogeneity of mouse and human microglia at single-cell resolution. Nature.

Matcovitch-Natan, O., Winter, D.R., Giladi, A., Vargas Aguilar, S., Spinrad, A., Sarrazin, S., Ben-Yehuda, H., David, E., Zelada González, F., Perrin, P., et al. (2016). Microglia development follows a stepwise program to regulate brain homeostasis. Science *353*, aad8670.

Mathys, H., Adaikkan, C., Gao, F., Young, J.Z., Manet, E., Hemberg, M., De Jager, P.L., Ransohoff, R.M., Regev, A., and Tsai, L.H. (2017). Temporal Tracking of Microglia Activation in Neurodegeneration at Single-Cell Resolution. Cell Rep.

Mauch, D.H., Nägier, K., Schumacher, S., Göritz, C., Müller, E.C., Otto, A., and Pfrieger, F.W. (2001). CNS synaptogenesis promoted by glia-derived cholesterol. Science (80-.).

Mazaheri, F., Breus, O., Durdu, S., Haas, P., Wittbrodt, J., Gilmour, D., and Peri, F. (2014a). Distinct roles for BAI1 and TIM-4 in the engulfment of dying neurons by microglia. Nat. Commun.

Mazaheri, F., Breus, O., Durdu, S., Haas, P., Wittbrodt, J., Gilmour, D., and Peri, F. (2014b). Distinct roles for BAI1 and TIM-4 in the engulfment of dying neurons by microglia. Nat. Commun. 2014 51 *5*, 1–11.

Mazzolini, J., Le Clerc, S., Morisse, G., Coulonges, C., Kuil, L.E., van Ham, T.J., Zagury, J.F., and Sieger, D. (2020). Gene expression profiling reveals a conserved microglia signature in

larval zebrafish. Glia *68*, 298–315.

McCray, P.B., Pewe, L., Wohlford-Lenane, C., Hickey, M., Manzel, L., Shi, L., Netland, J., Jia, H.P., Halabi, C., Sigmund, C.D., et al. (2007). Lethal Infection of K18-hACE2 Mice Infected with Severe Acute Respiratory Syndrome Coronavirus. J. Virol.

McKercher, S.R., Torbett, B.E., Anderson, K.L., Henkel, G.W., Vestal, D.J., Baribault, H., Klemsz, M., Feeney, A.J., Wu, G.E., Paige, C.J., et al. (1996). Targeted disruption of the PU.1 gene results in multiple hematopoietic abnormalities. EMBO J. *15*, 5647–5658.

McNab, F., Mayer-Barber, K., Sher, A., Wack, A., and O'Garra, A. (2015). Type I interferons in infectious disease. Nat. Rev. Immunol. *15*, 87–103.

McRae, P.A., Rocco, M.M., Kelly, G., Brumberg, J.C., and Matthews, R.T. (2007). Sensory Deprivation Alters Aggrecan and Perineuronal Net Expression in the Mouse Barrel Cortex. J. Neurosci.

Medendorp, W.E., Bjorefeldt, A., Crespo, E.L., Prakash, M., Pal, A., Waddell, M.L., Moore, C.I., and Hochgeschwender, U. (2021). Selective postnatal excitation of neocortical pyramidal neurons results in distinctive behavioral and circuit deficits in adulthood. IScience *24*.

Meeker, N.D., and Trede, N.S. (2008). Immunology and zebrafish: Spawning new models of human disease. Dev. Comp. Immunol. *32*, 745–757.

Miltenyi, S., Müller, W., Weichel, W., and Radbruch, A. (1990). High gradient magnetic cell separation with MACS. Cytometry *11*, 231–238.

Minter, M.R., Moore, Z., Zhang, M., Brody, K.M., Jones, N.C., Shultz, S.R., Taylor, J.M., and Crack, P.J. (2016). Deletion of the type-1 interferon receptor in APPSWE/PS1ΔE9 mice preserves cognitive function and alters glial phenotype. Acta Neuropathol. Commun. *4*, 72.

Miyamoto, A., Wake, H., Ishikawa, A.W., Eto, K., Shibata, K., Murakoshi, H., Koizumi, S., Moorhouse, A.J., Yoshimura, Y., and Nabekura, J. (2016). Microglia contact induces synapse formation in developing somatosensory cortex. Nat. Commun.

Montagutelli, X., Prot, M., Levillayer, L., Salazar, E.B., Jouvion, G., Conquet, L., Donati, F., Albert, M., Gambaro, F., Behillil, S., et al. (2021). The B1.351 and P.1 variants extend SARS-CoV-2 host range to mice. BioRxiv 2021.03.18.436013.

Moore, Z., Mobilio, F., Walker, F.R., Taylor, J.M., and Crack, P.J. (2020). Abrogation of type-I interferon signalling alters the microglial response to Aβ1-42. Sci. Rep. *10*, 3153.

Murwantoko, Yano, M., Ueta, Y., Murasaki, A., Kanda, H., Oka, C., and Kawaichi, M. (2004). Binding of proteins to the PDZ domain proteolytic activity of HtrA1 serine protease. Biochem. J.

Ndoja, A., Reja, R., Lee, S.H., Webster, J.D., Ngu, H., Rose, C.M., Kirkpatrick, D.S., Modrusan, Z., Chen, Y.J.J., Dugger, D.L., et al. (2020). Ubiquitin Ligase COP1 Suppresses Neuroinflammation by Degrading c/EBPβ in Microglia. Cell *182*, 1156-1169.e12.

Nguyen, P.T., Dorman, L.C., Pan, S., Vainchtein, I.D., Han, R.T., Nakao-Inoue, H., Taloma, S.E., Barron, J.J., Molofsky, A.B., Kheirbek, M.A., et al. (2020). Microglial Remodeling of the Extracellular Matrix Promotes Synapse Plasticity. Cell.

Nimmerjahn, A., Kirchhoff, F., and Helmchen, F. (2005). Neuroscience: Resting microglial cells are highly dynamic surveillants of brain parenchyma in vivo. Science (80-.).

Oakley, H., Cole, S.L., Logan, S., Maus, E., Shao, P., Craft, J., Guillozet-Bongaarts, A., Ohno, M., Disterhoft, J., Van Eldik, L., et al. (2006). Intraneuronal β-amyloid aggregates, neurodegeneration, and neuron loss in transgenic mice with five familial Alzheimer's disease mutations: Potential factors in amyloid plaque formation. J. Neurosci.

Ochocka, N., Segit, P., Walentynowicz, K.A., Wojnicki, K., Cyranowski, S., Swatler, J., Mieczkowski, J., and Kaminska, B. (2021). Single-cell RNA sequencing reveals functional heterogeneity of glioma-associated brain macrophages. Nat. Commun. *12*.

Oosterhof, N., Holtman, I.R., Kuil, L.E., van der Linde, H.C., Boddeke, E.W.G.M., Eggen, B.J.L., and van Ham, T.J. (2017). Identification of a conserved and acute neurodegeneration-specific microglial transcriptome in the zebrafish. Glia *65*, 138–149.

Oosterhof, N., Kuil, L.E., van der Linde, H.C., Burm, S.M., Berdowski, W., van Ijcken, W.F.J., van Swieten, J.C., Hol, E.M., Verheijen, M.H.G., and van Ham, T.J. (2018). Colony-Stimulating Factor 1 Receptor (CSF1R) Regulates Microglia Density and Distribution, but Not Microglia Differentiation In Vivo. Cell Rep. *24*, 1203-1217.e6.

Orre, M., Kamphuis, W., Osborn, L.M., Jansen, A.H.P., Kooijman, L., Bossers, K., and Hol, E.M. (2014). Isolation of glia from Alzheimer's mice reveals inflammation anddysfunction. Neurobiol. Aging *35*, 2746–2760.

Paolicelli, R.C., Bolasco, G., Pagani, F., Maggi, L., Scianni, M., Panzanelli, P., Giustetto, M., Ferreira, T.A., Guiducci, E., Dumas, L., et al. (2011). Synaptic pruning by microglia is necessary for normal brain development. Science (80-.). *333*, 1456–1458.

Park, D., Tosello-Trampont, A.C., Elliott, M.R., Lu, M., Haney, L.B., Ma, Z., Klibanov, A.L., Mandell, J.W., and Ravichandran, K.S. (2007). BAI1 is an engulfment receptor for apoptotic cells upstream of the ELMO/Dock180/Rac module. Nature.

Peri, F., and Nüsslein-Volhard, C. (2008). Live imaging of neuronal degradation by microglia reveals a role for v0-ATPase a1 in phagosomal fusion in vivo. Cell *133*, 916–927.

Pfrieger, F.W. (2003). Role of cholesterol in synapse formation and function. Biochim. Biophys.

Acta - Biomembr.

Popova, G., Soliman, S.S., Kim, C.N., Keefe, M.G., Hennick, K.M., Jain, S., Li, T., Tejera, D., Shin, D., Chhun, B.B., et al. (2021). Human microglia states are conserved across experimental models and regulate neural stem cell responses in chimeric organoids. Cell Stem Cell *28*, 2153-2166.e6.

Prigge, J.R., Hoyt, T.R., Dobrinen, E., Capecchi, M.R., Schmidt, E.E., and Meissner, N. (2015). Type I IFNs Act upon Hematopoietic Progenitors To Protect and Maintain Hematopoiesis during Pneumocystis Lung Infection in Mice. J. Immunol.

Prinz, M., Jung, S., and Priller, J. (2019). Microglia Biology: One Century of Evolving Concepts. Cell.

Qiu, X., Mao, Q., Tang, Y., Wang, L., Chawla, R., Pliner, H.A., and Trapnell, C. (2017). Reversed graph embedding resolves complex single-cell trajectories. Nat. Methods *14*, 979–982.

Ranjbar, S., Haridas, V., Jasenosky, L.D., Falvo, J. V., and Goldfeld, A.E. (2015). A Role for IFITM Proteins in Restriction of Mycobacterium tuberculosis Infection. Cell Rep.

Ransohoff, R.M., and Cardona, A.E. (2010). The myeloid cells of the central nervous system parenchyma. Nature *468*, 253–262.

Rebsam, A., Seif, I., and Gaspar, P. (2002). Refinement of thalamocortical arbors and emergence of barrel domains in the primary somatosensory cortex: A study of normal and monoamine oxidase A knock-out mice. J. Neurosci. *22*, 8541–8552.

Renshaw, S.A., and Trede, N.S. (2012). A model 450 million years in the making: Zebrafish and vertebrate immunity. DMM Dis. Model. Mech. *5*, 38–47.

Rice, F.L., Gomez, C., Barstow, C., Burnet, A., and Sands, P. (1985). AComparative analysis of

the development of the primary somatosensory cortex: Interspecies similarities during barrel and laminar development. J. Comp. Neurol. *236*, 477–495.

Ritchie, M.E., Phipson, B., Wu, D., Hu, Y., Law, C.W., Shi, W., and Smyth, G.K. (2015). Limma powers differential expression analyses for RNA-sequencing and microarray studies. Nucleic Acids Res. *43*, e47.

Rougeot, J., Torraca, V., Zakrzewska, A., Kanwal, Z., Jansen, H.J., Sommer, F., Spaink, H.P., and Meijer, A.H. (2019). RNAseq Profiling of Leukocyte Populations in Zebrafish Larvae Reveals a cxcl11 Chemokine Gene as a Marker of Macrophage Polarization During Mycobacterial Infection. Front. Immunol. *10*, 832.

Roy, E.R., Wang, B., Wan, Y.W., Chiu, G., Cole, A., Yin, Z., Propson, N.E., Xu, Y., Jankowsky, J.L., Liu, Z., et al. (2020). Type I interferon response drives neuroinflammation and synapse loss in Alzheimer disease. J. Clin. Invest.

Sakai, C., Ijaz, S., and Hoffman, E.J. (2018). Zebrafish Models of Neurodevelopmental Disorders: Past, Present, and Future. Front. Mol. Neurosci. *11*.

Satija, R., Farrell, J.A., Gennert, D., Schier, A.F., and Regev, A. (2015). Spatial reconstruction of single-cell gene expression data. Nat. Biotechnol. *33*, 495–502.

Schafer, D.P., Lehrman, E.K., Kautzman, A.G., Koyama, R., Mardinly, A.R., Yamasaki, R., Ransohoff, R.M., Greenberg, M.E., Barres, B.A., and Stevens, B. (2012). Microglia sculpt postnatal neural circuits in an activity and complement-dependent manner. Neuron.

Schultz, L.B., Chehab, N.H., Malikzay, A., and Halazonetis, T.D. (2000). P53 Binding Protein 1 (53bp1) Is an Early Participant in the Cellular Response to DNA Double-Strand Breaks. J. Cell Biol. *151*, 1381.

Secombes, C.J., and Zou, J. (2017). Evolution of interferons and interferon receptors. Front. Immunol. *8*, 209.

Sehara, K., and Kawasaki, H. (2011). Neuronal circuits with whisker-related patterns. Mol. Neurobiol.

Sehara, K., Toda, T., Iwai, L., Wakimoto, M., Tanno, K., Matsubayashi, Y., and Kawasaki, H. (2010). Whisker-Related Axonal Patterns and Plasticity of Layer 2/3 Neurons in the Mouse Barrel Cortex. J. Neurosci.

Shanbhag, N.M., Evans, M.D., Mao, W., Nana, A.L., Seeley, W.W., Adame, A., Rissman, R.A., Masliah, E., and Mucke, L. (2019). Early neuronal accumulation of DNA double strand breaks in Alzheimer's disease. Acta Neuropathol. Commun. *7*.

Shen, K., Sidik, H., and Talbot, W.S. (2016). The Rag-Ragulator Complex Regulates Lysosome Function and Phagocytic Flux in Microglia. Cell Rep. *14*, 547–559.

Shi, L., Sun, Z., Su, W., Xu, F., Xie, D., Zhang, Q., Dai, X., Iyer, K., Hitchens, T.K., Foley, L.M., et al. (2021). Treg cell-derived osteopontin promotes microglia-mediated white matter repair after ischemic stroke. Immunity *54*, 1527-1542.e8.

Shirotani, K., Hori, Y., Yoshizaki, R., Higuchi, E., Colonna, M., Saito, T., Hashimoto, S., Saito, T., Saido, T.C., and Iwata, N. (2019). Aminophospholipids are signal-transducing TREM2 ligands on apoptotic cells. Sci. Rep. *9*, 1–9.

Sia, S.F., Yan, L.M., Chin, A.W.H., Fung, K., Choy, K.T., Wong, A.Y.L., Kaewpreedee, P., Perera, R.A.P.M., Poon, L.L.M., Nicholls, J.M., et al. (2020). Pathogenesis and transmission of SARS-CoV-2 in golden hamsters. Nature *583*, 834–838.

Sierra, A., Encinas, J.M., Deudero, J.J.P., Chancey, J.H., Enikolopov, G., Overstreet-Wadiche,

L.S., Tsirka, S.E., and Maletic-Savatic, M. (2010). Microglia shape adult hippocampal neurogenesis through apoptosis-coupled phagocytosis. Cell Stem Cell *7*, 483–495.

Sierra, A., de Castro, F., del Río-Hortega, J., Rafael Iglesias-Rozas, J., Garrosa, M., and Kettenmann, H. (2016). The "Big-Bang" for modern glial biology: Translation and comments on Pío del Río-Hortega 1919 series of papers on microglia. Glia *64*, 1801–1840.

Silva, N.J., Nagashima, M., Li, J., Kakuk-Atkins, L., Ashrafzadeh, M., Hyde, D.R., and Hitchcock, P.F. (2020). Inflammation and matrix metalloproteinase 9 (Mmp-9) regulate photoreceptor regeneration in adult zebrafish. Glia *68*, 1445–1465.

Silva, N.J., Dorman, L.C., Vainchtein, I.D., Horneck, N.C., and Molofsky, A. V. (2021). In situ and transcriptomic identification of microglia in synapse-rich regions of the developing zebrafish brain. Nat. Commun. 2021 121 *12*, 1–12.

Singh, S.K., Stogsdill, J.A., Pulimood, N.S., Dingsdale, H., Kim, Y.H., Pilaz, L.J., Kim, I.H., Manhaes, A.C., Rodrigues, W.S., Pamukcu, A., et al. (2016). Astrocytes Assemble Thalamocortical Synapses by Bridging NRX1α and NL1 via Hevin. Cell.

Song, E., Zhang, C., Israelow, B., Lu-Culligan, A., Prado, A.V., Skriabine, S., Lu, P., Weizman, O. El, Liu, F., Dai, Y., et al. (2021). Neuroinvasion of SARS-CoV-2 in human and mouse brain. J. Exp. Med.

Stephan, A.H., Barres, B.A., and Stevens, B. (2012). The complement system: An unexpected role in synaptic pruning during development and disease. Annu. Rev. Neurosci. *35*, 369–389.

Stevens, B., Allen, N.J., Vazquez, L.E., Howell, G.R., Christopherson, K.S., Nouri, N., Micheva, K.D., Mehalow, A.K., Huberman, A.D., Stafford, B., et al. (2007). The Classical Complement Cascade Mediates CNS Synapse Elimination. Cell *131*, 1164–1178.

Stogsdill, J.A., Ramirez, J., Liu, D., Kim, Y.H., Baldwin, K.T., Enustun, E., Ejikeme, T., Ji, R.R., and Eroglu, C. (2017). Astrocytic neuroligins control astrocyte morphogenesis and synaptogenesis. Nature *551*, 192–197.

Sugimoto, T., Xiao, C., Takeyama, A., He, Y.F., Takano-Yamamoto, T., and Ichikawa, H. (1999). Apoptotic cascade of neurons in the subcortical sensory relay nuclei following the neonatal infraorbital nerve transection. Brain Res.

Svahn, A.J., Graeber, M.B., Ellett, F., Lieschke, G.J., Rinkwitz, S., Bennett, M.R., and Becker, T.S. (2013). Development of ramified microglia from early macrophages in the zebrafish optic tectum. Dev. Neurobiol. *73*, 60–71.

Syage, A.R., Ekiz, H.A., Skinner, D.D., Stone, C., O'Connell, R.M., and Lane, T.E. (2020). Single-Cell RNA Sequencing Reveals the Diversity of the Immunological Landscape following Central Nervous System Infection by a Murine Coronavirus. J. Virol. *94*.

Takahashi, K., Rochford, C.D.P., and Neumann, H. (2005). Clearance of apoptotic neurons without inflammation by microglial triggering receptor expressed on myeloid cells-2. J. Exp. Med. *201*, 647–657.

Takaoka, A., and Yamada, T. (2019). Regulation of signaling mediated by nucleic acid sensors for innate interferon-mediated responses during viral infection. Int. Immunol.

Tang, Q., Iyer, S., Lobbardi, R., Moore, J.C., Chen, H., Lareau, C., Hebert, C., Shaw, M.L., Neftel, C., Suva, M.L., et al. (2017). Dissecting hematopoietic and renal cell heterogeneity in adult zebrafish at single-cell resolution using RNA sequencing. J. Exp. Med. *214*, 2875–2887.

Taquet, M., Luciano, S., Geddes, J.R., and Harrison, P.J. (2021). Bidirectional associations between COVID-19 and psychiatric disorder: retrospective cohort studies of 62 354 COVID-19

cases in the USA. The Lancet Psychiatry *8*, 130–140.

Trapnell, C., Cacchiarelli, D., Grimsby, J., Pokharel, P., Li, S., Morse, M., Lennon, N.J., Livak, K.J., Mikkelsen, T.S., and Rinn, J.L. (2014). The dynamics and regulators of cell fate decisions are revealed by pseudotemporal ordering of single cells. Nat. Biotechnol.

Tsai, H.I., Tsai, L.H., Chen, M.Y., and Chou, Y.C. (2006). Cholesterol deficiency perturbs actin signaling and glutamate homeostasis in hippocampal astrocytes. Brain Res.

Tsuchiya, A., Yano, M., Tocharus, J., Kojima, H., Fukumoto, M., Kawaichi, M., and Oka, C. (2005). Expression of mouse HtrA1 serine protease in normal bone and cartilage and its upregulation in joint cartilage damaged by experimental arthritis. Bone.

Uccellini, M.B., and García-Sastre, A. (2018). ISRE-Reporter Mouse Reveals High Basal and Induced Type I IFN Responses in Inflammatory Monocytes. Cell Rep.

Uribe-Querol, E., and Rosales, C. (2020). Phagocytosis: Our Current Understanding of a Universal Biological Process. Front. Immunol.

Utz, S.G., See, P., Mildenberger, W., Thion, M.S., Silvin, A., Lutz, M., Ingelfinger, F., Rayan, N.A., Lelios, I., Buttgereit, A., et al. (2020). Early Fate Defines Microglia and Non-parenchymal Brain Macrophage Development. Cell *181*, 557-573.e18.

Vainchtein, I.D., and Molofsky, A. V. (2020). Astrocytes and Microglia: In Sickness and in Health. Trends Neurosci.

Vainchtein, I.D., Chin, G., Cho, F.S., Kelley, K.W., Miller, J.G., Chien, E.C., Liddelow, S.A., Nguyen, P.T., Nakao-Inoue, H., Dorman, L.C., et al. (2018). Astrocyte-derived interleukin-33 promotes microglial synapse engulfment and neural circuit development. Science (80-.).

Valenza, M., Marullo, M., Di Paolo, E., Cesana, E., Zuccato, C., Biella, G., and Cattaneo, E.

(2015). Disruption of astrocyte-neuron cholesterol cross talk affects neuronal function in Huntington's disease. Cell Death Differ.

VanRyzin, J.W., Marquardt, A.E., Argue, K.J., Vecchiarelli, H.A., Ashton, S.E., Arambula, S.E., Hill, M.N., and McCarthy, M.M. (2019). Microglial Phagocytosis of Newborn Cells Is Induced by Endocannabinoids and Sculpts Sex Differences in Juvenile Rat Social Play. Neuron *102*, 435-449.e6.

Villani, A., Benjaminsen, J., Moritz, C., Henke, K., Hartmann, J., Norlin, N., Richter, K., Schieber, N.L., Franke, T., Schwab, Y., et al. (2019). Clearance by Microglia Depends on Packaging of Phagosomes into a Unique Cellular Compartment. Dev. Cell.

Wakselman, S., Béchade, C., Roumier, A., Bernard, D., Triller, A., and Bessis, A. (2008). Developmental neuronal death in hippocampus requires the microglial CD11b integrin and DAP12 immunoreceptor. J. Neurosci. *28*, 8138–8143.

Ward, I.M., Minn, K., van Deursen, J., and Chen, J. (2003). p53 Binding Protein 53BP1 Is Required for DNA Damage Responses and Tumor Suppression in Mice. Mol. Cell. Biol. *23*, 2556–2563.

Wee, Y.S., Roundy, K.M., Weis, J.J., and Weis, J.H. (2012). Interferon-inducible transmembrane proteins of the innate immune response act as membrane organizers by influencing clathrin and v-ATPase localization and function. Innate Immun.

Weinhard, L., di Bartolomei, G., Bolasco, G., Machado, P., Schieber, N.L., Neniskyte, U., Exiga, M., Vadisiute, A., Raggioli, A., Schertel, A., et al. (2018). Microglia remodel synapses by presynaptic trogocytosis and spine head filopodia induction. Nat. Commun. *9*, 1228.

Weissleder, R., Tung, C.H., Mahmood, U., and Bogdanov, A. (1999). In vivo imaging of tumors

with protease-activated near-infrared fluorescent probes. Nat. Biotechnol. *17*, 375–378.

Wittamer, V., Bertrand, J.Y., Gutschow, P.W., and Traver, D. (2011). Characterization of the mononuclear phagocyte system in zebrafish. Blood *117*, 7126–7135.

Wolf, S.A., Boddeke, H.W.G.M., and Kettenmann, H. (2017). Microglia in Physiology and Disease. Annu. Rev. Physiol. *79*, 619–643.

Woolsey, T.A., and Wann, J.R. (1976). Areal changes in mouse cortical barrels following vibrissal damage at different postnatal ages. J. Comp. Neurol.

Wu, J., and Chen, Z.J. (2014). Innate immune sensing and signaling of cytosolic nucleic acids. Annu. Rev. Immunol.

Wu, S., Xue, R., Hassan, S., Nguyen, T.M.L., Wang, T., Pan, H., Xu, J., Liu, Q., Zhang, W., and Wen, Z. (2018). Il34-Csf1r Pathway Regulates the Migration and Colonization of Microglial Precursors. Dev. Cell *46*, 552-563.e4.

Wu, S., Nguyen, L.T.M., Pan, H., Hassan, S., Dai, Y., Xu, J., and Wen, Z. (2020). Two phenotypically and functionally distinct microglial populations in adult zebrafish.

Wu, Y., Dissing-Olesen, L., MacVicar, B.A., and Stevens, B. (2015). Microglia: Dynamic Mediators of Synapse Development and Plasticity. Trends Immunol. *36*, 605–613.

Xu, J., Zhu, L., He, S., Wu, Y., Jin, W., Yu, T., Qu, J.Y., and Wen, Z. (2015). Temporal-Spatial Resolution Fate Mapping Reveals Distinct Origins for Embryonic and Adult Microglia in Zebrafish. Dev. Cell *34*, 632–641.

Zhan, L., Fan, L., Kodama, L., Sohn, P.D., Wong, M.Y., Mousa, G.A., Zhou, Y., Li, Y., and Gan, L. (2020). A MAC2-positive progenitor-like microglial population is resistant to CSF1R inhibition in adult mouse brain. Elife *9*, 1–22.

Zhang, Y., Chen, K., Sloan, S.A., Bennett, M.L., Scholze, A.R., O'Keeffe, S., Phatnani, H.P., Guarnieri, P., Caneda, C., Ruderisch, N., et al. (2014). An RNA-sequencing transcriptome and splicing database of glia, neurons, and vascular cells of the cerebral cortex. J. Neurosci.

Zhou, Y., Zhou, B., Pache, L., Chang, M., Khodabakhshi, A.H., Tanaseichuk, O., Benner, C., and Chanda, S.K. (2019). Metascape provides a biologist-oriented resource for the analysis of systems-level datasets. Nat. Commun.

Zimmerman, K.D., Espeland, M.A., and Langefeld, C.D. (2021). A practical solution to pseudoreplication bias in single-cell studies. Nat. Commun. *12*.

Publishing Agreement

It is the policy of the University to encourage open access and broad distribution of all theses, dissertations, and manuscripts. The Graduate Division will facilitate the distribution of UCSF theses, dissertations, and manuscripts to the UCSF Library for open access and distribution. UCSF will make such theses, dissertations, and manuscripts accessible to the public and will take reasonable steps to preserve these works in perpetuity.

I hereby grant the non-exclusive, perpetual right to The Regents of the University of California to reproduce, publicly display, distribute, preserve, and publish copies of my thesis, dissertation, or manuscript in any form or media, now existing or later derived, including access online for teaching, research, and public service purposes.

DocuSigned by:
Leah Dorman
FF56C76D977549E...
Author Signature

3/9/2022
Date